Thermodynamic and kinetic properties of metallic glasses during ultrafast heating

Dissertation
zur Erlangung des mathematisch-naturwissenschaftlichen Doktorgrades
"Doctor rerum naturalium"
der Georg-August-Universität Göttingen
-
im Promotionsprogramm ProPhys
der Georg-August University School of Science (GAUSS)

vorgelegt von

Stefan Küchemann

aus Göttingen

Göttingen, 2014

Betreuungsausschuss

Prof. Dr. Konrad Samwer, 1. Physikalisches Institut, Universität Göttingen

Mitglieder der Prüfungskommission

Referent:	Prof. Dr. Konrad Samwer, 1. Physikalisches Institut, Universität Göttingen
Korreferent:	Prof. Dr. Hans-Ulrich Krebs, Institut für Materialphysik, Universität Göttingen

Weitere Mitglieder der Prüfungskommission:

Prof. Dr. Annette Zippelius, Institut für Theoretische Physik, Universität Göttingen

Prof. Dr. Hans Christian Hofsäss, 2. Physikalisches Institut, Universität Göttingen

Prof. Dr. Cynthia Volkert, Institut für Materialphysik, Universität Göttingen

Prof. Dr. Vasile Mosneaga, 1. Physikalisches Institut, Universität Göttingen

Tag der mündlichen Prüfung:

Contents

List of Figures

List of Tables

Chapter 1

Introduction

Almost 300 years ago in 1724, Fahrenheit was the first to recognize in a series of experiments that water is capable of remaining in the liquid phase despite the fact that it was 8 K below its freezing point. In his experiment he sealed buckets of boiling water and left them outside for one night [1]. Only with the addition of ice crystals the supercooled water rapidly froze into a solid. His discovery inspired several more experiments with the intention to prove the universality of supercooling. Eventually, Turnbull could show in small mercury droplets that metallic liquids also have the capability of supercooling [2].
Upon further cooling, when crystallization can be avoided the system forms a glass - a solid with the frozen-in structure of a liquid. Despite the fact that glasses have been used since thousands of years for tools, hunting devices and in glassblowing [3], scientific experiments of glasses started in the 19th century. Between 1854 and 1866 R. Kohlrausch and F. Kohlrausch were some of the first who reported on the relaxation and diffusion in glassy materials [4]. About 100 years later in 1954 W. Buckel and R. Hilsch studied several metallic superconducting thin films which were evaporated on very cold substrates [5]. They found irreversible changes in the electrical resistance upon heating which Buckel could associate to a structural transformation from broad to sharp diffraction rings in electron diffraction experiments,[6]. Finally, in 1960 the group of P. Duwez found non-crystalline metallic structures in the metallic-metalloid alloy $Au_{75}Si_{25}$ by splat quenching [7].
Since the discovery, there have been several theories to predict the characteristics of the glass state [8, 9, 10, 11, 12] which could only succeed in a limited number of cases and a general theory could not emerge. A helpful classification was suggested by Angell. He observed that there are a range of glass formers, particularly network glasses like SiO_2 and GeO_2, which exhibit a rather slow decrease in viscosity upon heating above the glass transition temperature, which he called strong glasses [13]. Others, as for instance polymers, exhibit a rapidly decreasing viscosity during heating above the glass transition temperature. Among others there are for

example metallic glasses which can be found in between these two types.
During cooling from the high temperature liquid, the dramatic decrease in the dynamics is discussed with the growing length scales of dynamical heterogeneities - regions which exhibit different mobility. Due to dynamical heterogeneities the dynamics of supercooled liquids start to deviate substantially from predictions of stable liquids during cooling [14, 15, 16]. In metallic glass formers, there are a number of recent works which report the occurrence of icosahedral clusters [17, 18, 19, 20] which also exhibit a connection to the deviation of the dynamics of supercooled liquids from the dynamics of stable liquids.
In general, it is difficult to test the supercooled metallic liquids due to their comparable small resistance against crystallization. The fast incipient crystallization process in the supercooled liquid restricts the studies to short timescales and usually to temperatures close to the glass transition temperature or the melting temperature. Recently, studies of crystallization behavior could be extended far above the glass transition temperature for good glass formers by using a so called Ultrafast Scanning Calorimetry[21]. This technique reaches heating rates of up to 10^5 K/s and enables thermodynamic measurements as in a conventional calorimeter but the sample masses are limited to the order of μg. Another technique was invented by Johnson et al. using a rapid capacitor discharge[22]. This method is based on ohmic heating during a capacitor discharge. It can be combined with, for instance, an in-situ deformation procedure enabling the study of viscosity or enthalpy at heating rates of 10^5 - 10^6 K/s.
In this work, we use a capacitor discharge technique to heat up metallic glass ribbons into the supercooled liquid where we study the specific heat capacity and crystallization behavior. Additionally, we investigate the dependence of the glass transition temperature on heating rate using an intermediate heating rate technique with a power supply, differential scanning calorimetry and the capacitor discharge technique.
After this introduction in chapter 1, the second chapter comprises a classification of the glass state and characteristics of the glass transition. Particularly, previous observations of decoupling phenomena and liquid-liquid phase transition in glasses are presented. It continues with the crystallization in the framework of the time-temperature-transformation diagram and reviews the classical homogeneous and heterogeneous nucleation. At the end of the second chapter, general findings about the temperature dependence of the electrical resistance are summarized. Chapter 3 explains the capacitor discharge technique and calibration procedures. Particularly, this chapter also contains the chopper system which was used to increase the temporal resolution of the 2D X-ray detector at the synchrotron beamline. Eventually, this chapter explains the evaluation procedure and data analysis of the X-ray patterns. Chapter 4 starts with the results of the glass transition temperature and crystallization temperature using standard calorimetry techniques. Afterwards, the results of three different ways of determining

the specific heat capacity using the capacitor discharge technique are shown. This is followed by the results of the glass transition temperature using the intermediate heating technique. A main part of this chapter consists of the report of the crystallization process at different temperatures of the crystallization nose. It ends with the results of the ultrafast heating experiments which bypass the crystallization nose. All findings of this work are discussed and compared to previous results of other groups in chapter 5. Particularly, we compare the different techniques and connect the results obtained by different techniques, for example for the change in the glass transition temperature with heating rate. Finally, the results of this work are summarized in chapter 6 and a perspective and motivation for future experiments are given in the outlook.

Chapter 2

Theoretical framework

2.1 Classification of the glassy state

When a glass forming liquid is quenched below its liquidus temperature, the system departs from equilibrium and its timescales for relaxation processes increase until they are in an experimentally accessible time regime. If the system is quenched fast enough, the atoms are incapable to order into a crystalline structure and thus the configurational liquid freezes into a solid glass. The transition from the supercooled liquid to the solid glass is termed glass transition. At the glass transition, the system falls out of equilibrium and it is defined to be at the point where the internal relaxation time is about 100 s [16]. Above the glass transition temperature, the system is able to sample various states of the Potential Energy Landscape (PEL), which describes all possible states of a system in a multidimensional surface, while below the glass transition the system is trapped in one state. Therefore, the glass transition marks a transition from a dynamic continuum state to a quasi-static state [23].
Generally, the timescales of dynamics and relaxation processes vary between different locations in the sample. There are sites which transform to be liquid-like[1] earlier than others. Just in the moment, when a certain volume fraction reaches the percolation concentration as predicted by Cohen and Crest [23, 26], the glass transition occurs.

Upon cooling from the liquidus temperature to the glass transition temperature, the relaxation time as well as the viscosity changes several orders of magnitude. For instance, the viscosity with a value of $\eta = 10^{-2}\ Pa \cdot s$ at the liquidus temperature increases to a value $\eta = 10^{12}\ Pa \cdot s$ commonly within a temperature range between 150-500 K [27] (Fig. 2.1). This change in viscos-

[1]The term liquid-like can be either defined by a critical volume strain of 0.11 (Eshelby's transformation strain [24]) which a local region needs to overcome or by the dynamic argument which is implied in the Deborah number that a region responds liquid-like when the local relaxation time is smaller than the inverse of an externally applied frequency [25]

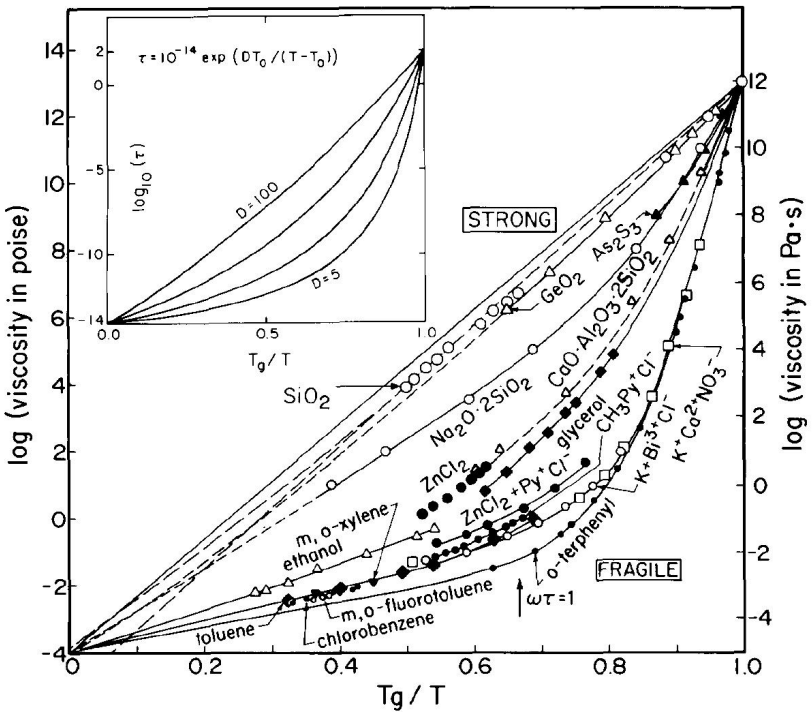

Figure 2.1: The so called Angell-plot shows the temperature dependence of the viscosity of various glass forming liquids above the glass transition temperature T_G. From [13]. Reprinted with permission from AAAS.

ity as well as the change in relaxation time can be either described by an Arrhenius law (termed as strong liquids) $\eta(T) = \eta_0 \cdot \exp(E/RT)$, with the activation energy E and the universal gas constant R, or by the Vogel-Fulcher-Tamann (VFT) law (classified as fragile liquids)[16]:

$$\eta(T) = \eta_0 \cdot \exp(DT_0/(T - T_0)) \tag{2.1}$$

with the constants A, D and T_0. Each curve in Fig. 2.1 can be characterized by the fragility m of the system which corresponds to the slope of the curve $m = \frac{\mathrm{d}\log\eta}{\mathrm{d}(T_G/T)}$. The parameter D in the VFT is related to the fragility by $D = 590/(m - 16)$[28]. This connection can be seen in the inset of Fig. 2.1.

The tremendous slowdown in the dynamics of a glass forming liquid during cooling from the liquidus temperature is not understood [29]. Usually, such dramatic changes are only observed during first order phase transitions, as for instance melting. In fact, the scenario of a first or second order phase transition in the liquid has been used as an attempt to explain some of dynamics of glass forming liquids [30].

The fragility of the system, with the exception of alcohols, is also related to the heat capacity jump at the glass transition temperature. Fragile liquids exhibit a large jump while strong

liquids show a smaller jump at the glass transition temperature [29]. Additionally, the glass transition range $\Delta T_G/T_G = (T_{G,max} - T_{G,onset})/T_G$, which is the temperature interval from the onset of the increase in the specific heat capacity at the glass transition until the end of the increase, is also small for fragile and large for strong supercooled liquids.

2.2 Characteristics of the glass transition

2.2.1 Rate dependence of the glass transition temperature

Whether a system exhibits a solid- or a liquid-like response to an external excitation depends on the timescale of observation t_{obs} relative to the internal timescale of relaxation τ_{relax} which can be expressed in the Deborah number $DE = \tau_{relax}/t_{obs}$ [25]. When the observation time is longer than the internal relaxation time (i.e. $DE < 1$), one can observe liquid-like response and, in the other case, when $DE > 1$ the system response like a solid. In this context, the glass transition marks the arbitrary transition between the two regimes. Therefore, we find the point where the glass transition occurs when the following equation is fulfilled

$$\tau_{relax} \cdot \omega_{obs} \;=\; 1. \tag{2.2}$$

This is a slight modification of the aforementioned relation where we included the frequency of an external excitation $\omega_{obs} = 1/t_{obs}$. The relaxation time can be identified to be the α-relaxation time whose temperature dependence for several glass formers can be described by the previously mentioned VFT equation within a certain temperature interval.

In general, when a glass forming system is quenched with a lower cooling rate, the system has more time in a certain temperature interval to equilibrate. Therefore, the glass transition occurs at a lower temperature [16, 31]. For instance, the rate dependence of the glass transition can be observed in the specific heat capacity. If a glass is heated up with a lower heating rate than is was previously quenched, the glass has more time to relax and the glass transition occurs at a lower temperature (see Fig. 2.2). The relaxation is manifested in slightly lower specific heat values below the glass transition temperature. The opposite happens if the glass is heated with a higher rate in comparison to the previous cooling rate. In this case, the glass transition temperature shifts to higher temperatures which is accompanied with a distinct overshoot above the specific heat level of the supercooled liquid.

Moynihan et al. showed that the change in glass transition temperature is linearly proportional to the logarithm of heating rate [32]. Later on, Brüning et al investigated a wider range of heating rates of almost four orders of magnitude in differential scanning calorimetry measurements

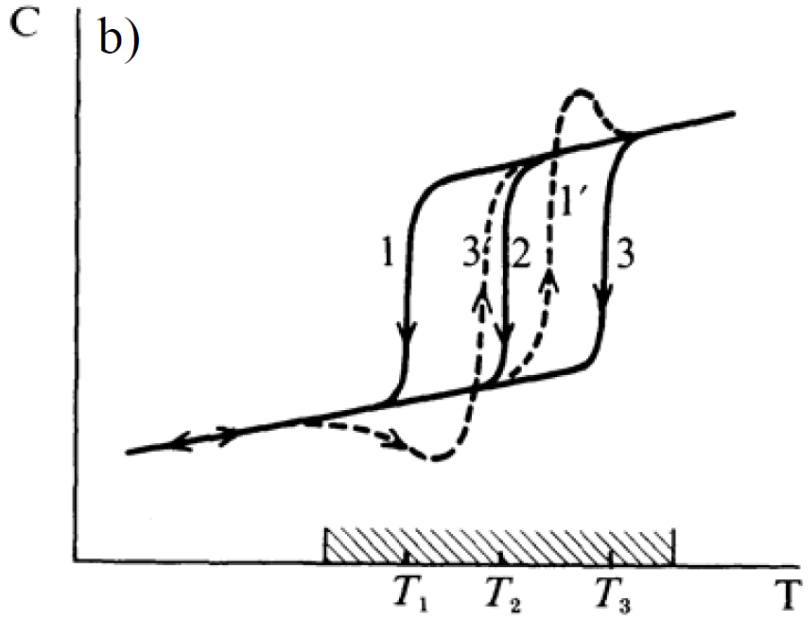

Figure 2.2: Chart of the specific heat of a glass forming liquid as a function of temperature around the glass transition temperature. The glass transition temperature shifts to higher temperatures if the glass is heated with a higher rate (1') than it was previously quenched (1). In this case, the specific heat exhibits an overshoot before it levels off in the supercooled liquid. When the glass is heated up with a slower rate (3') than it was previously quenched (3), the glass transition temperature shifts to lower temperatures accompanied with a lower specific heat value below the glass transition as an indication for relaxation processes. Taken from [3].

of several glass formers [33] (see Fig. 2.3).

They found that the heating rate dependence of the glass transition temperature can be better described by the VFT equation. This result was later confirmed in simulations of a Lennard-Jones system of Vollmayr et al. [34]. They motivated the dependence of the glass transition temperature on heating rate by combining equation 2.1 and 2.2, where the external frequency ω was replaced by the cooling rate ϕ. Consequently, if the relation from the Deborah number can also be applied to heating and cooling rate, it might be able to quantify the heating rate and cooling rate dependence of the glass transition temperature. It results in

$$T_G = T_0 - \frac{DT_0}{ln(\omega \cdot \tau_0)}. \tag{2.3}$$

Dixon also studied the glass transition temperature of salol in dielectric measurements [35]. In these measurements, the glass transition occurs at a maximum of the dielectric loss during the variation of the frequency of the dynamical excitation. Dixon observed that the change in glass transition as a function of excitation frequency can also be best described by the VFT

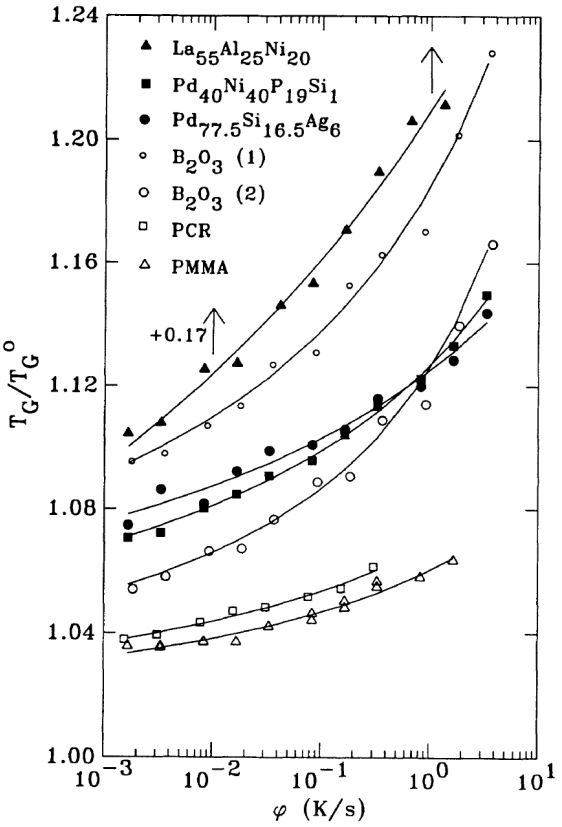

Figure 2.3: Change in glass transition temperature with heating rate for several glass formers. Reprinted with permission from [33]. Copyright 1992 by the American Physical Society.

equation. However, the change of the glass transition over 13 decades in excitation frequency cannot be described by a single VFT fit. Instead, the VFT equation can fit the data only over a smaller interval.

2.2.2 Increase in the specific heat capacity at the glass transition

The specific heat capacity is a thermodynamic quantity which is commonly analyzed when studying the glass transition. Upon heating, the specific heat capacity rises stronger at the glass transition than it does in the glassy state before it levels off in the supercooled liquid regime. The transition from the glassy state into the supercooled liquid is not a sudden process as it occurs, for instance, during a second order phase transition. Instead it takes place in a certain temperature range and this temperature range also increases with increasing heating rate [33].

Ke et al. found that the expected specific heat capacity difference between the glassy state and supercooled liquid at the glass transition is $\Delta c_P = 13.69 \pm 2.05$ J/mol·K [36], which is

independent on the composition and hence independent on the fragility. The authors discuss the heat capacity jump at the glass transition in the context of the free volume model. They relate the jump to a critical value of the reduced free volume of 0.0235 which is similar to the value of the reduced free volume of 0.024 during yielding after an externally applied stress. While the implications of the free volume theory seem to be rather questionable [37], the specific heat capacity increase at the glass transition temperature can also be interpreted in the thermodynamic equipartition theorem in which each degree of freedom in average contributes R/2 to the specific heat capacity [23, 36]. The value of Δc_P is very close to $3/2R = 12.47$ J/mol·K and thus there are 3 degrees of freedom more available when the system crosses the glass transition.
The value of $3/2R$ for the rise of the specific heat capacity at the glass transition was also found in theoretical considerations by Egami [23]. In his theory, the local atomic level stress can be expressed in a 3×3 tensor with 6 independent components: the atomic level pressure which is the trace of the tensor and five components of shear stresses. At high temperatures the total potential energy, which is equal to the configurational enthalpy, of $1.5k_BT$ is equally distributed in these 6 components [23] fulfilling the equipartition theorem. When the temperature is lowered, the system is becoming denser and consequently more frustrated. This frustration gradually creates a long range stress field as the viscosity increases during cooling [23]. Below the glass transition, the configurational enthalpy does not change anymore and thus the specific heat makes a jump of $1.5k_B$ at the glass transition.

2.3 Kinetic decoupling phenomena in supercooled liquids

In ordinary liquids at high temperatures T, the viscosity η of the system is closely related to the translational diffusion D by the Stokes-Einstein-relation

$$D = \frac{k_B T}{f\eta}, \tag{2.4}$$

with the Boltzmann constant k_B and a size parameter f [38]. When a glass forming system is cooled down from the melting point towards the glass transition temperature, the structure of the supercooled liquid clusters into regions with different mobility which relax on different timescales [39, 40]. The size of these so-called dynamical heterogeneities grow upon cooling [41, 42].
Additionally to growing cluster length scales upon cooling in the supercooled liquid, Rössler

found in NMR studies that the translational diffusion decouples from the rotational diffusion and from viscosity [14] (see Fig. 2.4b). Fig. 2.4b shows the translational and rotational diffusion D_r of o-terphenyl versus the viscosity and the temperature. During cooling, the translational diffusion deviated from the η^{-1}-dependence and exhibits a weaker dependence on viscosity than the rotational diffusion below 290 K. Related to eq. 2.4, this phenomenon is also called the breakdown of the Stokes-Einstein relation. The Stokes-Einstein breakdown could be found in a number of glass of formers and is expected to be a universal phenomenon [16].
Apart from the breakdown of the Stokes-Einstein relation, during cooling from the melting temperature the relaxation of the system splits into a primary relaxation process, the α-process and a secondary process, which is also called β-process or Johari-Goldstein process [29, 43, 44] The α-process is related to the cooperative viscous flow while the β-relaxation also exhibits a certain cooperativity but on a smaller scale most likely in a string-like motion (see Fig. 2.4a) [45, 46]. Fig. 2.4a shows an Arrhenius plot of the frequency and the temperature of chlorobenzene. It is visible that the α-process splits during cooling from the β-process at a temperature of about 167 K (1000/T=6.0 K^{-1}) and exhibits a stronger temperature dependence than the β-process. Among simple liquids and polymers the temperature where the α-, β-

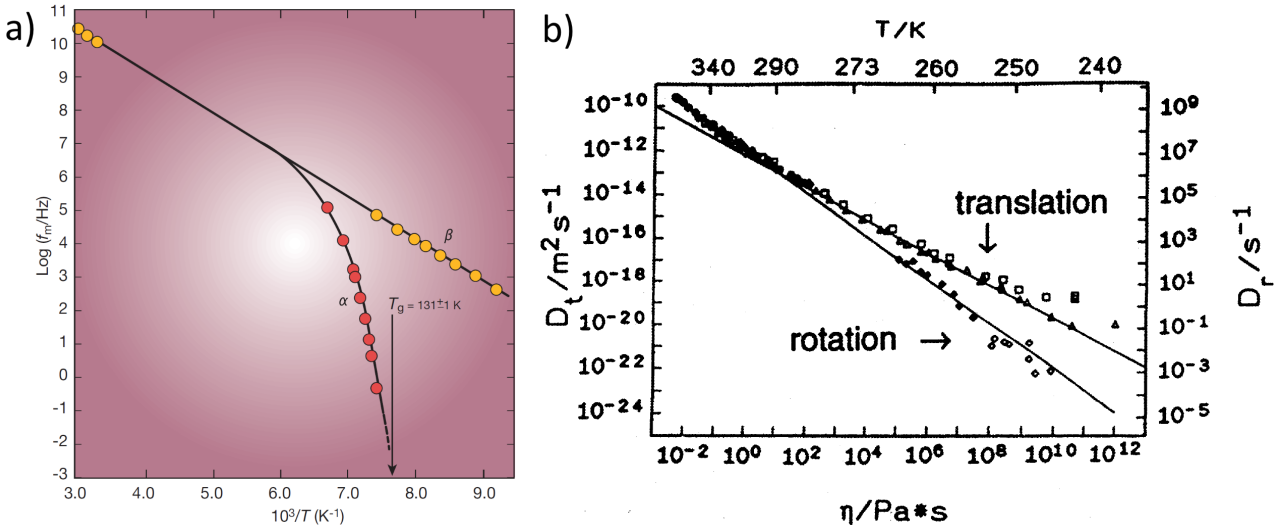

Figure 2.4: a) Separation of α- and β-process in the supercooled liquid of chlorobenzene/*cis*-decalin (molar ration 17.2/82.8 %) during cooling. Reprinted by permission from Macmillan Publishers Ltd: Nature (Ref. [16]), copyright (2001). b) Translational D_t and rotational diffusion D_r of deuterated o-terphenyl versus the viscosity and the temperature. Reprinted from [47]. Copyright (1994), with permission from Elsevier.

separation takes place varies in the range between $1.12 \cdot T_G$ for Polystyrene and $2.2 \cdot T_G$ for Cyanoadamantane.

Hachenberg and coworkers estimated the temperature where the α- and the β-process merge again during heating from the glass into the supercooled liquid to be at 720 K for $Pd_{77.5}Cu_6Si_{16.5}$ and 870 K for $Zr_{65}Cu_{27.5}Al_{7.5}$ [48]. These temperatures correspond to $1.16 \cdot T_G$ with $T_G = 622K$ and $1.41 \cdot T_G$ with $T_G = 615K$ for the Pd-based and the Zr-based glass former, respectively. The temperature dependence of the α-process can be described by the aforementioned Vogel-Fulcher-Tammann equation 2.1 while the relaxation time of the β-process follows an Arrhenius behavior [49]. In some cases it was observed that the α-, β-separation takes place close to the Mode-coupling temperature T_C [20, 48, 14]. At the temperature T_C the mode-coupling theory predicts a dynamical phase transition [30]. It is expected that the breakdown of Stokes-Einstein and the α-, β-separation are caused by the growing length scales of dynamical heterogeneities [14].
Eventually, Angell et al. observed that supercooled water exhibits a very high fragility just at the melting temperature during quenching [50]. However, the expected glass transition between 200 K and 220 K, as a result from extrapolation from liquid heat capacity data, does not take place. Instead they found, that the glass transition range $\Delta T_G/T_G = 0.1$ is very large comparable to the very strong glass former SiO_2. The authors assign this dramatic change in fragility to a fragile to strong transition during cooling in the supercooled liquid.

2.4 First order liquid-liquid phase transition in supercooled liquids

In some glass formers, particularly in SiO_2, GeO_2, silicone, water, a liquid-liquid phase transition could be observed. Particularly in metallic glasses, Li et al. found a hysteresis in the volume of three Zr-based glass formers (Vit1, Vit106, LM7) close to the melting temperature [51]. Later on, Busch et al. found a specific heat maximum also in Vit1 above the melting temperature which they could assign to a liquid-liquid first order phase transition [52]. In molecular dynamics (MD) simulations, Lad and coworkers analyzed the metallic glass former $Cu_{64.5}Zr_{35.5}$ [20]. While cooling from the liquid to the solid glass state they found a hysteresis in enthalpy. Additionally, they found a fragile to strong transition and the breakdown of the Stokes-Einstein relation all located close to the critical MCT temperature T_C. They could connect the aforementioned processes to the emergence of icosahedral clusters in the supercooled liquid upon cooling. Fig. 2.5a illustrates the different manifestations of icosahedral clusters in their metallic glass former. Fig. 2.5b shows the increase of the number of different icosahedral clusters upon cooling starting above the experimental liquidus temperature which is about 1273 K until temperatures which are below the calorimetric glass transition temperature of 787 K.

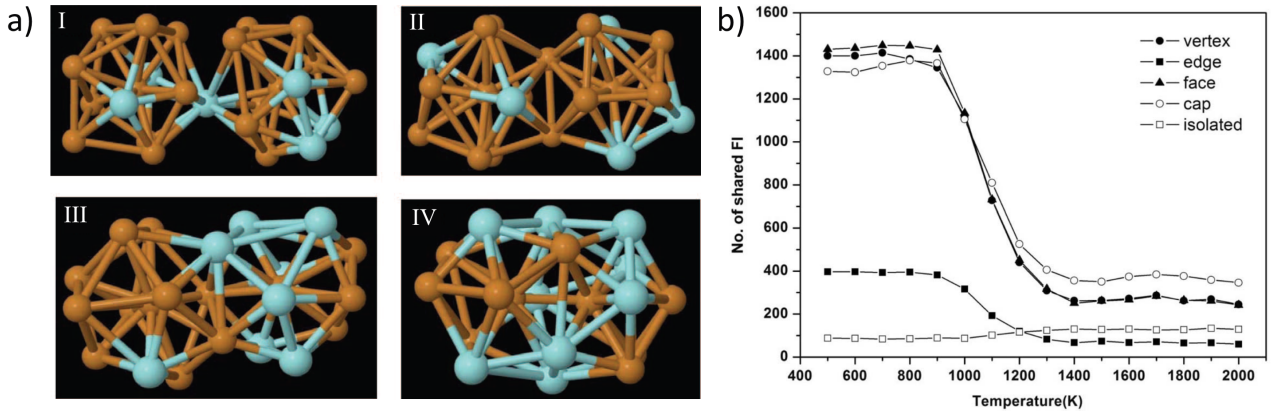

Figure 2.5: Icosahedral clusters in the supercooled liquid. a) Different types of links between two icosahedral clusters consisting of Cu (red)and Zr atoms (blue): I) vertex, II) edge, III) face and IV) pentagonal-cap. b) Increase in the number of the various cluster types mentioned in panel a) in the supercooled liquid region. Reprinted with permission from [20]. Copyright 2012, AIP Publishing LLC.

2.5 Time-temperature-transformation diagram

In general, a time-temperature-transformation (TTT) diagram is a plot in which the temperature is plotted versus the logarithm of time. It indicates how long it takes during an isothermal experiment for a certain reaction or process to take place. In the case of glasses, it reflects, for instance, the previously mentioned rate dependence of the glass transition and its sensitivity towards crystallization.

Usually in the TTT diagram of a metallic glass, there are four different states: the glass, the supercooled liquid, the high temperature liquid and the crystal (often termed as crystallization nose due to its shape; see Fig. 2.6). At sufficiently low temperatures on all laboratory timescales the system responds as a solid glass. When the temperature is increased, the system crosses the glass transition temperature into the supercooled liquid region. Now, if the system is heated further with a heating rate lower than the critical heating rate, the system inevitably crystallizes. This is the case in conventional laboratory experiments as for instance in calorimetric measurement.

Another scenario takes place when the heating rate is increased to a critical heating rate. At that critical heating rate, the sample does not crystallize during heating above the glass transition temperature. For a successful preparation of an amorphous sample by rapid quenching, it is also necessary to bypass the crystallization nose. The minimum rate which is necessary to form a glass is indicated by the critical cooling rate.

In experiments, the behavior of metallic glasses is not as it is expected theoretically [53, 22, 54] and as it is depicted in Fig. 2.6. The value of the critical heating rate differs significantly from

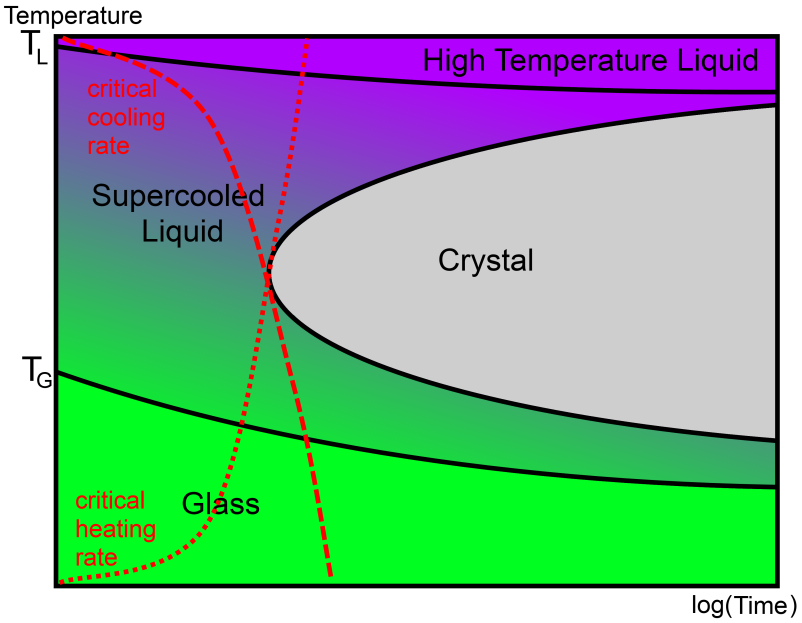

Figure 2.6: Schematic drawing of a TTT diagram of a glass.

the value of the critical cooling rate. In fact, the Zr-based system Vit. 1 exhibits a critical cooling rate of 2 K/s and a critical heating rate of 200 K/s, thus there is a factor of 100 between the two quantities in this example. This behavior is shown in Fig. 2.7.

Both critical rates are dependent on the position of the crystallization nose in the TTT diagram. The distinct difference between the two rates points out that the crystallization behavior is very different when the sample devitrifies starting from the solid glass phase in comparison to the crystallization starting from the equilibrated high temperature liquid. And additionally, in Fig. 2.7 it is visible that the crystallization nose during heating is not only shifted to shorter times but the shape of the crystallization nose during heating is also different in comparison to the one during cooling.

2.6 Crystallization of metallic glasses

The field of crystallization is widely studied since many years. This short section cannot account for the various manifestations in different systems and situations. It is strongly restricted to the scenarios which are relevant for the scope of the measurements presented in this thesis. The shape of the previously mentioned crystallization nose is given by the temperature dependence of the nucleation rate and crystal growth rate. The two concepts of nucleation and growth are discussed briefly in this chapter. For a more comprehensive treatment of crystallization we

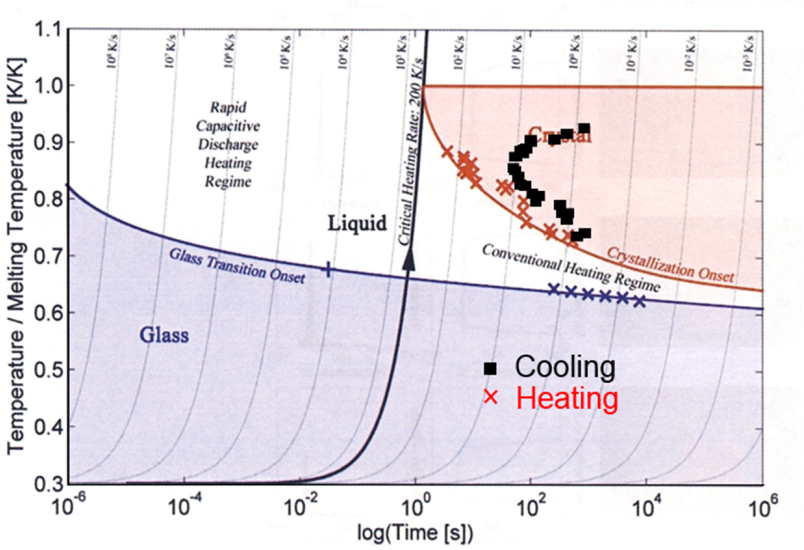

Figure 2.7: Measurement of the TTT diagram of Vit. 1 during cooling (black squares) and during heating (red crosses). The figure has been created by digitizing the measurements of Kim et al. [53] for the TTT curve during cooling and plotting the data points in the measurements of Johnson et al. Therefore, we used a melting temperature of $T_M = 993$ K as reported in [53]. From [22]. Reprinted with permission from AAAS.

refer to reference [1].

2.6.1 Homogeneous nucleation

In the classical homogeneous nucleation, the formation of a little crystalline inclusion (also termed crystallite) within a metastable, amorphous matrix, as for instance in a supercooled liquid, requires a certain amount of energy in order to create the amorphous-crystalline interface (surface energy), on one hand, and, on the other hand, it gains energy because the energy state of a crystalline structure is lower than the energy state of an amorphous structure (bulk energy)[1, 55]. Both quantities, the surface energy as well as the bulk energy, are dependent on the radius r of the crystalline inclusion. The balance between surface energy and bulk energy can be expressed in the Gibbs' free energy ΔG of a crystalline inclusion in an amorphous matrix [55]:

$$\Delta G = \underbrace{4\pi r^2 \gamma}_{\text{Surface energy}} - \underbrace{\frac{4\pi}{3} r^3 \Delta\mu n}_{\text{Bulk energy}} \tag{2.5}$$

with the free energy of the crystal-amorphous interface per unit area γ, the difference between the chemical potential of the amorphous structure and the chemical potential of the crystal $\Delta\mu$ and the number density of particles in the crystalline structure n. Very small crystallites are formed by statistical fluctuations. In fact, it is energetically unfavorable to form a very small crystallite within a metastable, amorphous matrix because the surface energy exceeds the bulk energy. When the crystallite continues to grow, despite its unfavorable situation, it reaches a maximum in the Gibbs' free energy difference and in the work required to form a crystallite at

$$\Delta G^* = \frac{16\pi\gamma^3}{3\Delta G^2}. \tag{2.6}$$

The maximum work required to form a critical nuclei corresponds to critical radius of $r^* = 2\gamma/(\Delta\mu n)$. Above the critical radius, ΔG decreases and thus it is favorable for the nucleus to continue growing (Fig. 2.8).

The temperature where the nucleation rate has its maximum often differs from the temper-

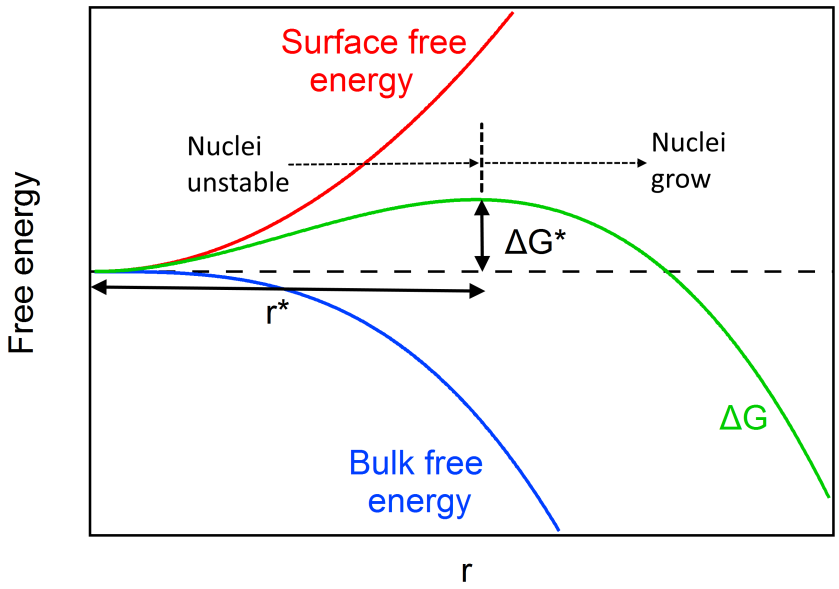

Figure 2.8: Gibbs' free energy as a function of radius.

ature of the maximum crystal growth rate [1]. In fact, the nucleation rate is very sensitive to changes in temperature [2]. In non-isothermal experiments, the change in temperature during crystallization, either by externally supplied heat or by the enthalpy release due to crystallization, has the consequence that the transformation from the amorphous to the crystalline phase of most of the volume is caused by crystal growth.

The crystal growth rate $U(T)$ is given by a product of a kinetic term U_{kin} which is mainly de-

termined by the viscosity η and a thermodynamic term which involves the difference $\Delta G_{cryst-liq}$ of the Gibbs free energies of the crystalline state and the supercooled liquid state.

$$U(T) = U_{kin}\left(1 - \frac{\Delta G_{cryst-liq}}{RT}\right) \tag{2.7}$$

where the kinetic term close to the liquidus temperature is given by

$$U_{kin} = \frac{k_B T}{3\pi l^2 \eta}. \tag{2.8}$$

It is visible that Eq. 2.7 becomes very small close to the liquidus temperature since the Gibbs free energy difference $\Delta G_{cryst-liq}$, which indictes the driving force for crystallization, also gets very small. Close to the glass transition temperature, the growth rate is mainly determined by the kinetic term since the viscosity is strongly increasing with decreasing temperature [56]. Thus, the growth rate is also very small close to the glass transition temperature.
In recent experiments, Ediger et al. and Orava et al. could show that the relation $U_{kin} \propto \eta^{-\xi}$ with $\xi = 1$ breaks down close to the glass transition temperature (see Fig. 2.9)[56, 21]. Fig. 2.9 shows a double logarithmic plot of the kinetic coefficient of crystal growth as a function of viscosity η. When approaching the glass transition at a viscosity of $10^{12} Pa \cdot s$ the slope of the curve in the log-log plot deviates from the high temperature (low viscosity) behavior of -1. So the growth rate decouples from the kinetics close to the glass transition. Ediger et al. found that the factor ξ is mostly smaller than one. In fact, the value of ξ depends on the fragility $m = \mathrm{d}log(\eta)/\mathrm{d}(T_G/T)$. The authors argue that the change in ξ is caused by the growing sizes of dynamical heterogeneities when approaching the glass transition temperature.

Nucleation and crystal growth causes a certain volume faction $X_{cryst}(t)$ to crystallize after the time t. In general, the increase in X_{cryst} with time can be described by the Johnson-Mehl-Avrami (JMA) equation

$$X_{cryst} = 1 - exp(-(kt)^n) \tag{2.9}$$

with the Avrami coefficient n and the kinetic exponent k [57]. The kinetic coefficient is closely related to crystal growth rate while the Avrami coefficient contains information about the growth mode. The JMA equation was derived for cases where the following three assumptions are fulfilled [57]:

- Isothermal crystallization conditions
- Homogeneous nucleation or heterogeneous nucleation at randomly dispersed second phase particles
- The growth of the new phase is dependent on temperature and independent on time

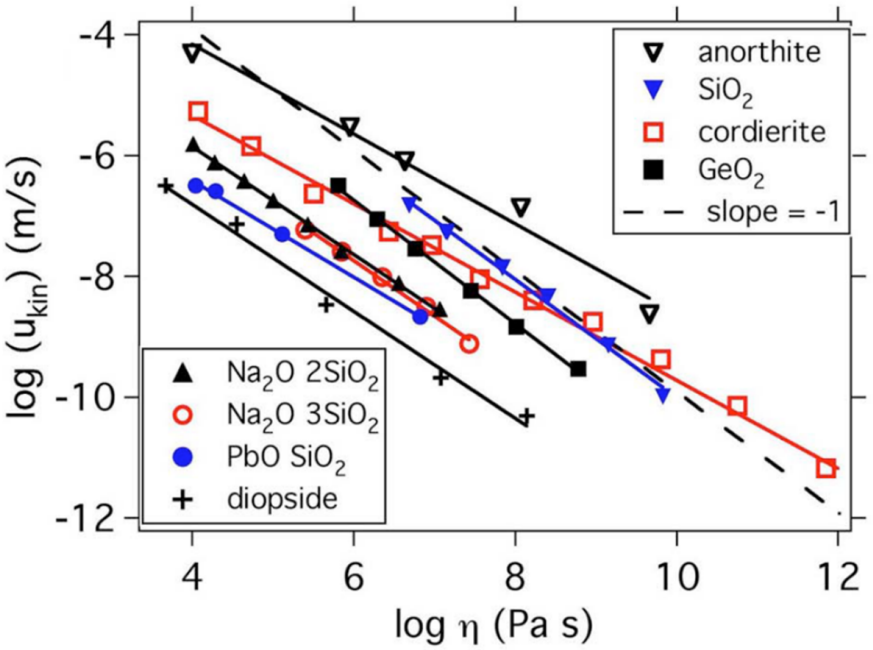

Figure 2.9: Decoupling of kinetic coefficient of crystal growth from the viscosity for several glass formers. Reprinted with permission from [56]. Copyright 2008, AIP Publishing LLC.

In few cases, the JMA equation can also be applied to non-isothermal data. However, the application of the equation must be verified otherwise the interpretation of the fitting parameters leads to wrong conclusions in those cases.

2.6.2 Heterogeneous nucleation

In most experiments, crystallization is not governed by homogeneous nucleation on random sites in the system. Instead, the new phase forms at preferred sites such as dissolved impurities or interfaces [29]. This process is called heterogeneous nucleation. The driving forces for heterogeneous nucleation are lower than for homogeneous nucleation and the heterogeneous nucleation rate crucially depends on the number of atoms in contact with the nucleation centers [1]. Therefore it is difficult to completely avoid heterogeneous nucleation. Even if the liquid is intrinsically pure and free of impurities, container walls during the quenching process may lead to heterogeneous nucleation.

As a consequence, in metallic glasses there is always a certain amount in the order of 10^6 quenched-in nuclei within the amorphous matrix [1]. The small amount of quenched-in nuclei are usually not detectable by X-ray diffraction techniques. In some cases the number of nuclei in the nanometer range is becoming significantly large but since they are still randomly orientated they are indistinguishable in X-ray diffraction patterns. In those cases the transformation from

the remaining amorphous amorphous volume to the crystalline structure is governed exclusively by crystal growth and heterogeneous nucleation is inhibited. This change in the crystallization process has a different signature in the enthalpy release rate which can be measured in standard calorimetry measurements [58]. In the case of crystallization by nucleation, the enthalpy release

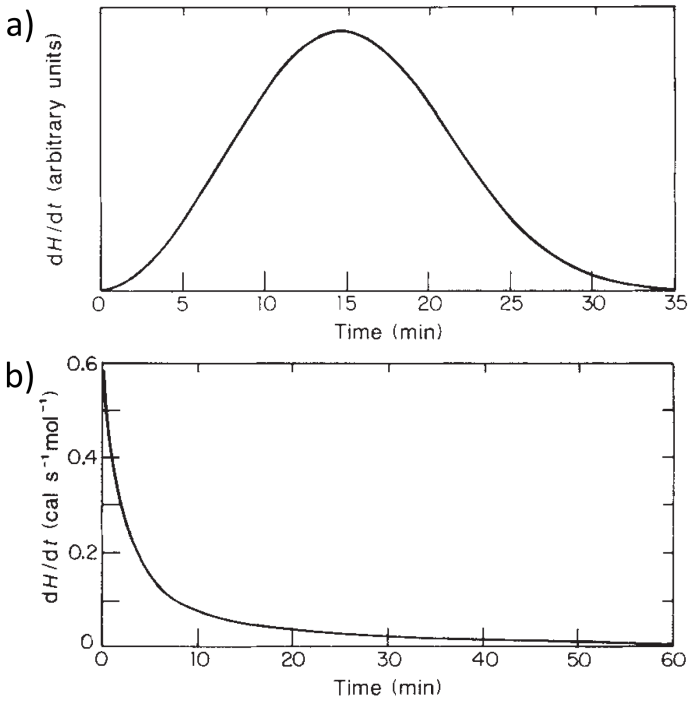

Figure 2.10: Enthalpy release rate as a function of time during a) crystallization by isothermal nucleation and b) crystallization governed by grain growth. Reprinted by permission from Macmillan Publishers Ltd: Nature (Ref. [58]), copyright (1988)

rate as a function of time exhibits a clear maximum while in the case of the crystallization governed by crystal growth, the enthalpy release rate simply decays as a function of time (see Fig. 2.10).

2.7 Determination of the crystallized volume fraction

We determined the crystallized volume fraction by the ratio of the peak areas of the crystalline peaks and peak areas of both amorphous and crystalline diffraction peaks. We followed the analysis described by Riello et al. [59] and also performed by Bednarcik et al. [60]. They report that the crystallized volume fraction can be calculated by the equation

$$X_{cryst} = \frac{M_{cryst} \sum_{i=1}^{n_{cryst}} m_i}{M_{total} \sum_{i=1}^{n_{sample}} m_i} \tag{2.10}$$

with

$$M_{cryst} = \frac{\int_{q_{min}}^{q_{max}} I_{cryst}(q) q^2 \mathrm{d}q}{\sum_{i=1}^{n_{cryst}} \int_{q_{min}}^{q_{max}} \left[|f_i(q)|^2 + I_i^{inc} \right] q^2 \mathrm{d}q} \tag{2.11}$$

and

$$M_{total} = \frac{\int_{q_{min}}^{q_{max}} I_{total}(q) q^2 \mathrm{d}q}{\sum_{i=1}^{n_{sample}} \int_{q_{min}}^{q_{max}} \left[|f_i(q)|^2 + I_i^{inc} \right] q^2 \mathrm{d}q}. \tag{2.12}$$

The quantities n_{cryst} and n_{sample} represent the number of atoms in the unit cell of the crystalline phase and the number of atoms in the composition unit of the sample, respectively. The intensities I_{cryst} and I_{total} are the bragg peaks of the crystalline phase and the intensity of all peaks, respectively, I_i^{inc} is the incoherent scattering intensity, m_i refers to the atomic weight and f_i is the atomic scattering factor of the i-th atom [61].
In order to integrate the peaks from different phases the X-ray diffraction spectrum were fitted with a multiple Gaussian function. More details on the data analysis can be found in the results section 4.12.

2.8 Micro-alloying

The macroscopic properties of glass forming alloy are very sensitive to small changes in the composition. This fact may complicate the reproducibility of literature data and it makes it difficult to compare results with literature data. In order to ensure the comparability of the results in this work, we usually used a single ribbon for one set of measurements. In case that two or more ribbons were used, we compared EDX results (see section 4.2) and performed test measurements in order to verify that both ribbons behave similarly.
One example where the properties of the glass change is the composition $Ce_{70}Cu_{20}Al_{10}$. When 1 at% of Ce is replaced by Nb or only 0.5 at% of Ce by Co the glass-forming ability, measured by a critical maximal casting diameter, increases from 2 mm to 10 mm in both cases [62]. Additionally, with the addition of 1 at% of Nb the self-diffusivity of Cu atoms decreases about 74 % and the temperature dependence changes from Arrhenius to non-Arrhenius behavior [63]. For industrial applications, it might be interesting to note that the toughness, shear modulus, yield strength and Poisson's ratio can be varied, for example, by the addition of 1 at% Si to the composition $Cu_{47}Ti_{34}Zr_{11}Ni_8$ [64]. One possible explanation for the effects of micro-alloying was found by Cohen et al. in pinning a small fraction of particles in their simulated system, i.e. not allowing any movement to the particles except the affine displacement. When the fraction of randomly pinned particles exceeded 2.5 %, the slow β-process, which appears as a low-temperature or high-frequency wing of the primary α-process, disappears while the α-process is only slightly affected and pushed to lower frequencies [65]. Additionally it could be

found that pinning a small amount of particles affect mechanical properties, such as toughness, shear modulus and yield strength [66].
Apart from the correct composition, it is important that all components are well dispersed in the system in order to obtain a homogeneous alloy. It is well known, that the components of an alloy intermix well, when the enthalpy of mixing is strongly negative. A negative enthalpy of mixing could also be identified to be a factor for good glass-forming ability [67].
Some glasses also exhibit chemical phase separation upon cooling in the supercooled liquid, as for instance the Zr-based glass former Vit. 1 [53], which may enhance the already remarkable variation in the local properties like the elastic modulus found in $Pd_{77.5}Cu_6Si_{16.5}$ [68].

2.9 Temperature dependence of the electrical resistance of metallic glasses

The electrical resistance of the metallic glass samples plays a key role in our measurements. The metallic glass only heats up during the capacitor discharge when the resistance of the sample is large at all temperatures in comparison to the rest of the circuit (see section 3.3). Therefore, the electrical resistance and its temperature dependence of a metallic glass are briefly explained in this section.
As described in section 3.6, one condition for homogeneous heating is that the thermal coefficient of resistance $\alpha_\rho = \frac{1}{\rho}\frac{\partial \rho}{\partial T}$ is small. A confirmation of such condition was found by Mooji who analyzed thermal coefficients of electrical resistance of several glasses as a function of specific electrical resistance [31]. He found that the thermal coefficient of resistance is very small and monotonically decreases with increasing specific electrical resistance (Fig. 2.11a). The graph crosses zero at a value of about 150 $\mu\Omega$cm. Therefore, all glasses with a specific electrical resistance smaller than 150 $\mu\Omega$cm exhibit a very small positive thermal coefficient of resistance while all glasses with a specific electrical resistance above that threshold have a negative thermal coefficient of resistance. Upon temperature increase all specific electrical resistances approach the threshold value of 150 $\mu\Omega$cm (Fig. 2.11b).

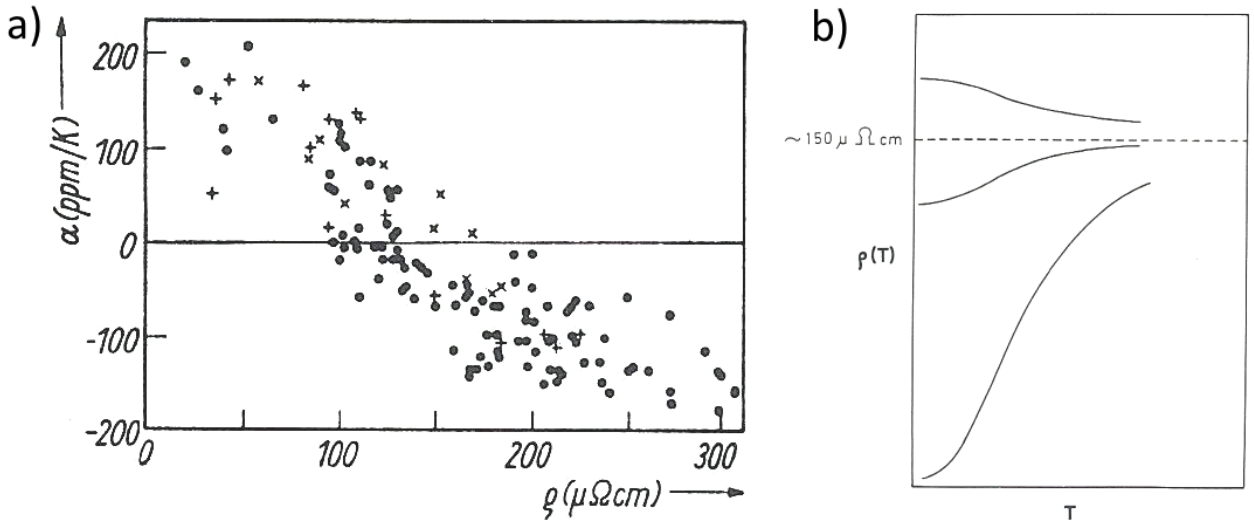

Figure 2.11: a) Thermal coefficient of electrical resistance of several glasses as a function of specific electrical resistance. From [31]. b) Specific electrical resistance as a function of temperature for three exemplary glasses. Springer and the original publisher [69] is given to the publication in which the material was originally published, by adding; with kind permission from Springer Science and Business Media.

Chapter 3

Experimental and analytical methods

3.1 Preparation of metallic glasses by melt spinning

For the experiments, we used melt spun ribbons of the nominal composition of $Zr_{65}Cu_{27.5}Al_{7.5}$. In order to prepare these samples, we prepared a crystalline pre-alloy of the same nominal composition in an arc-melter in a 600 mbar argon atmosphere. The purity of the used elements Zr,Cu and Al was 99.935%, 99.999% and 99.999%, respectively. The resulting alloy was broken into pieces using a hardened steel mortar in order to fit the alloy into the glass tube which was installed in the melt spinner. For the melting and subsequent quenching of this alloy, the chamber of the melt spinner was six times fluxed with argon and eventually set to a an argon pressure of 400 mbar in the main chamber and 700 mbar in the pressure tubes. After the final evacuation, before the fluxing with argon, we reached a pressure of the order of 10^{-6} mbar in the chamber. The frequency of the copper wheel was set to 40 Hz and the nozzle of the glass tube had a diameter of 2.0 mm. During quenching the temperature was recorded using a pyrometer. The sample was inductively heated to a maximum temperature of 2173 K in the case of ribbon A and a maximum temperature of 1423 K for ribbon B right before it was quenched. These temperatures are 1023 K and 273 K higher than the expected melting temperature of 1150 K [70]. In order to quench the molten alloy, the over pressure in the pressure tubes was released which squeezed the molten alloy through the nozzle on the rotating copper wheel. The resulting ribbons had a thickness of about 42 μm.

3.2 Characterisation of metallic glasses

The amorphicity of the samples has been tested using X-ray diffraction experiments. The samples which have been used during our synchrotron studies were tested with the high energy

X-ray beam of 70 keV prior to the measurement. The beam transmits the sample while some of the photons are scattered. The energy corresponds to a wavelength of $\lambda = 0.17712$ Å^{-1}. Using the large flat panel detector Perkin Elmer XRD 1621 (see below) we cover a q-range up to $q = 12$ Å^{-1}. In the case of an amorphous sample, one can observe broad, diffuse maxima in the structure factor as well as in the pair distribution function which are decaying in intensity towards higher q-values. These diffuse diffraction maxima of amorphous samples are correlated to the fluctuations in the nearest neighbor distance and also to the second-, third- and higher nearest neighbor distances of the atoms. The decay of intensities of the maxima towards higher q-values are caused by the relatively pronounced short range order and the lack of long range order in glasses.

The amorphicity of the samples which have been measured in the laboratory in Goettingen were tested using a Siemens D8 diffractometer. The diffractometer uses Cu K_α radiation with a wavelength of $\lambda = 1.574$ Å.

The glass transition temperature, as well as the crystallization temperature and the crystallization enthalpy contain valuable information about the state of the prepared sample. For instance, the difference ΔT between the glass transition temperature and the crystallization temperature is related to the resistance towards crystallization and thus makes a statement about the quality of the glass [67]. In the case of one of the compositions $Zr_{65}Cu_{27.5}Al_{7.5}$ which we used in this work, the type of crystallization (single or multiple crystallizations) also exhibits whether or not a metastable intermittent phase, like for instance a quasicrystalline phase, is formed before the final phase is established. In this composition, Murty and coworkers showed that a quasicrystalline state is only formed in those cases where a sufficient amount ($\geq 0.43at\%$) of oxygen is incorporated in the composition. These oxygen atoms act as nucleation centers for a quasicrystalline icosahedral phase which was also discussed in the section "Microalloying" [71]. Accordingly, there is also a noticeable difference in the crystallization enthalpy and ΔT between the two crystallization types.

Apart from that, the heat flow below the glass transition gives information about relaxation processes which are closely linked to the β-relaxation and which can be enhanced, for instance, by previous deformation [72]. Therefore, we measured the heat flow our samples in a power compensated Differential Scanning Calorimeter 7 (DSC 7) from Perkin Elmer. The analyzed sample is in the first of the two sample holders and a reference material, in our case it was left empty, is placed in the second one. Both sample holders are equipped with a separate heater and a Pt13 resistance, which is used to measure the temperature. A controller assures the consistency of the previously set heating rate, it does not regulate the same temperature in the two holders. The output signal is the heat flow difference between the sample and the reference which is sensitive to relaxation processes, such as glass transition and crystallization. It can

also be related to the specific heat of the sample. A more detailed description of the setup can be found in [73, 74].
For our measurements, we varied the available heating rates from 10 to 200 K/min. During the measurement, the sample holder was fluxed with Argon in order to avoid pressure fluctuations and to hinder oxidation. We calibrated the temperature axis of the DSC 7 prior to the measurement of metallic glasses with the melting temperatures of Indium ($T_m = 429.6$ K [75]) and Zinc ($T_m = 692.47$ K [75]). The heat flow axis we calibrated with the heat of fusion of Indium. Apart from DSC measurements, we also performed Energy Dispersive X-ray diffraction measurements in a Supra 35 Zeiss REM with an EDX addition in order to test the composition. As described in the section "Microalloying", slight variations in the composition can have significant effects. Therefore, it is essential to verify that the correct amount of the constituents is obtained after the sample preparation.

3.3 Ultrafast heating using a capacitor discharge technique

In order to achieve heating rates in the order of 10^6 K/s we used a capacitor discharge with a very small characteristic time constant $\tau = R \cdot C$. Here, R represents the resistance of the discharge circuit. Despite this feature, the capacity C still had to be large enough so that the energy supplied to the sample is sufficient to heat it up above its liquidus temperature.
The entire circuit is shown and explained in Appendix A. The main components of the discharge circuit are shown in Fig. 3.1. We use a capacitor with a capacity of 1 μF and a charge voltage of 0-500 V. The discharge of the capacitor is initiated via a thyristor which has a switching time of 3 μs. The electrical connections to the sample are made of massive copper rods and plates. In this way, the conductors can handle large currents and the resistance of the circuit without the sample R_0 is kept small which increases the efficiency of the system given by $\epsilon = R_S/(R_0 + R_S)$, where R_S is the resistance of the sample. The efficiency determines the amount of heat dissipated in the sample.
During the measurement, we determined the temperature locally of the sample using a Kleiber KGA 740 pyrometer (later on termed as "low temperature pyrometer"). The pyrometer measures the emitted infrared radiation of the surface of the sample on a spot of 1 mm diameter in a wavelength range of 1.58 - 2.2 μm and a temperature range of 433 - 1273 K. The response time for the analog voltage read out is 6 μs. In certain measurements, we used another pyrometer, the Impac IGA 740 (later on termed as "high temperature pyrometer"). It has the same specifications as the KGA 740, e.g. a response of 6 μs, except that it measures in a wavelength

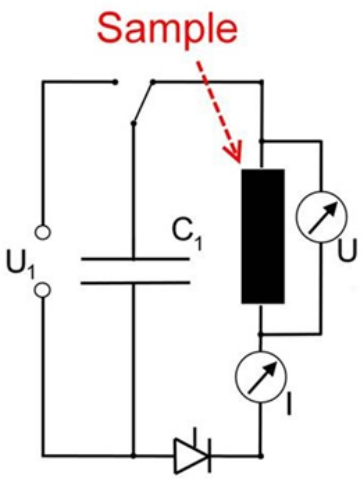

Figure 3.1: Discharge Circuit

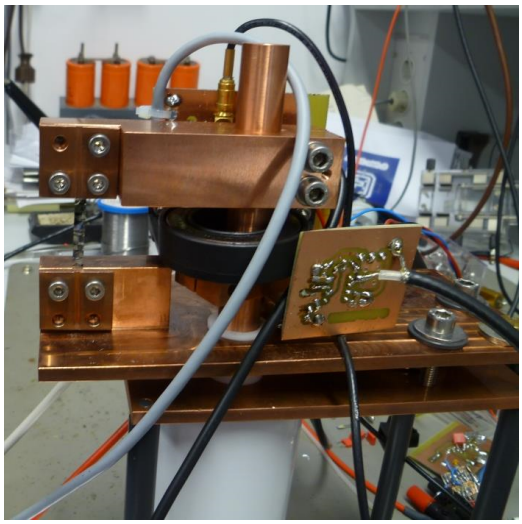

Figure 3.2: Photograph of Discharge Circuit

range of 2.0 - 2.2 μm and a temperature range of 573 K - 2573 K. In case we used the latter pyrometer, it is mentioned in the text.

For the data acquisition, we used a analog-to-digital converter (ADC) NI PCI 6133. It has 8 simultaneously recorded channels which have a resolution of 14 bits at an input voltage range from -10 to 10 V and a read out frequency of 2.5 MHz. Therefore, we obtain a resolution of $1.22 \cdot 10^{-3}$ V which, for instance, results in a temperature resolution of 0.2 K for the low temperature pyrometer and 0.5 K for the high temperature pyrometer since the voltage output of the two pyrometers is from 0 - 10 V.

For the voltage measurement, we installed a voltage divider with a voltage ratio of 1/100 in order not to exceed the required input voltage range of the -10 to 10 V of the ADC during a discharge.

We performed the current measurements with two methods. First, we installed a Hall sensor Honeywell CSLA2EN and second, we wound a Rogowski coil Admess LFR 30/300 around one of the copper rods. The Rogowski coil can measure AC currents with a frequency 45 Hz - 20 kHz and therefore it is capable of resolving the current change during our discharge. The sensitivity of the coil can be switched between 1 mV/A with a peak current of 6 kA and 0.1 mV/A with a peak current of 60 kA. The Hall sensor can also measure direct currents and has a temporal resolution of 3 μs, a peak current of 950 A and a sensitivity of 0.788 A.

3.4 Ultrafast heating using multi-step rapid capacitor discharges

As an addition to the rapid capacitor discharge technique with a single capacitor of $C_1 = 1000\ \mu$F, we installed four small capacitors of about $C_{2-5} = 200\ \mu$F which can be charged with up to 300 V in the setup (Fig. 3.3). The additional capacitors are installed in the same way in

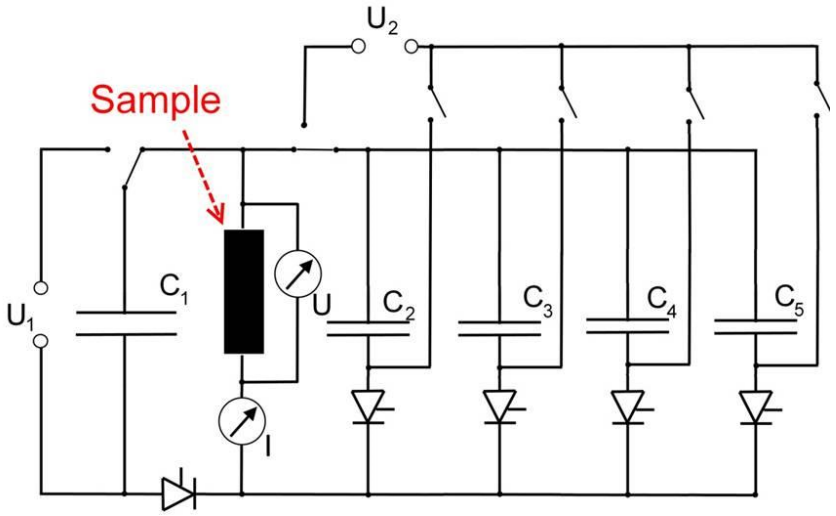

Figure 3.3: Rapid capacitor discharge technique using multiple discharges.

the discharge circuit as the primary capacitor C_1. All four capacitors are charged by the same power supply U_2 and they can be discharged via the same type of thyristors as used for the main capacitor. In the measurement, these capacitors are usually discharged after the main capacitor and one after the other. Between the discharges the user can set a waiting time. In this way, the capacitors are charged with small voltages of about 20 V and they are discharged when the sample is at high temperatures. Each of them leads to a very small temperature increase of about 3-7 K. The key feature of these four capacitors is that the characteristic discharge time of $7.8 \cdot 10^{-5}$ s is also very small due to the relatively small capacity. This allows studies of the specific heat at high temperatures after the main capacitor discharge is over.

3.5 Intermediate heating using a programmable power supply

There is a certain gap of about five orders of magnitude between the heating rate range of the calorimeter DSC 7 with a maximum heating rate of 5 K/s and the heating rates of the capacitor

discharge which are in the order of 10^6 K/s. In order to fill this gap, we heated up metallic glasses with a programmable power supply SM 70-22 from Delta Eletronika. For this purpose we integrated the power supply in the aforementioned circuit shown in Fig. 3.1 and removed the previous power supply, the capacitor and the thyristor. The power supply SM 70-22 has a power of 1500 W and is able to apply a maximum current of 22 A within 0.47 ms [76]. We controlled the power supply in the constant current (CC) mode using a LabView program. In this mode, the power supply adjusts the voltage in order to obtain a user-defined current in the circuit. With the LabView program we were able to set different current ramps which result in different heating rates.

3.6 Conditions for homogeneous heating during the capacitor discharge

In order to properly interpret and compare the results and, particularly, determine quantitatively the specific heat capacity during the primary capacitor discharge it is important to verify that the samples heat up homogeneously during the capacitor discharge. Johnson et al. identified three conditions which need to be met in order to achieve homogeneous heating [22]:

1. A highly uniform cross section
2. A small value of the thermal coefficient of resistance $\alpha_\rho = \frac{1}{\rho}\frac{\partial \rho}{\partial T}$
3. A dynamic electromagnetic skin depth $\Lambda = 2\rho/mu_0\omega$ at the frequency ω is much larger than the sample dimension normal to the applied field

The first condition can be fulfilled during the sample preparation. The second condition was described above in section 2.9. And for the third condition we calculated the skin depth in our setup for the composition $Pd_{77.5}Cu_6Si_{16.5}$ to be $\Lambda = 2.2$ cm using a specific electrical resistance of $\rho = 8.6 \cdot 10^{-7}$ Ωm and a frequency of $\omega = 1/\tau = 1/R \cdot C = 2.778 \cdot 10^3$ s^{-1}. This skin depth is larger than a typical width of 3 mm and a typical thickness of 40 μm and therefore the third condition is also fulfilled.
The ultrafast heating technique using a capacitor discharge cannot be applied to crystalline metals because in crystalline metals ohmic dissipation tends to spatially localize. Additionally, due to the positive thermal coefficient of resistance every heating increases electrical resistance which, again, amplifies localized dissipation again. During the melting of the crystal the electrical resistance makes a sudden jump which enhances localized heat dissipation additionally.
In previous measurements the homogeneity of the heating process during a capacitor discharge

was tested using a fast infrared camera [22]. Fig. 3.4 shows the very homogeneous temperature distribution during the capacitor discharge. The full width at half maximum of the temperature distribution over the entire sample is 7 K.

Unfortunately, we were not able to test homogeneity of the heating process with our setup and

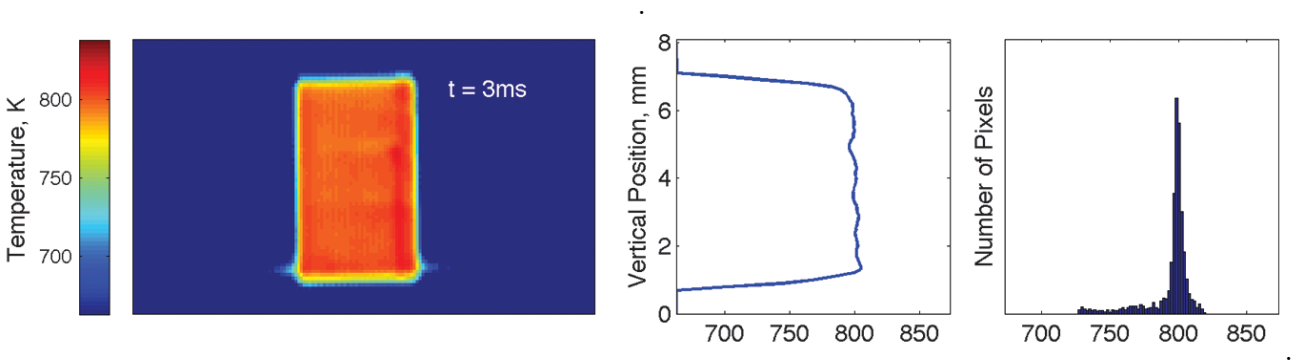

Figure 3.4: Temperature distribution in a bulk metallic glass rod during the capacitor discharge (left panel). The middle panel shows the average temperature along the vertical position. The right panel shows the temperature distribution among different pixels of the camera. From [22]. Reprinted with permission from AAAS.

with our samples. We could only ensure that the samples have a homogeneous diameter and that the length is long in comparison to the width and the thickness.

3.7 Calibration of Hall sensor

The Hall sensor Honeywell CSLA2EN was calibrated using a simple electrical circuit consisting of a power supply and a resistance. The cable was wound three times through the loop of the current sensor. This setup had two advantages. First, the accuracy during the calibration is increased and second, we could reach higher currents and thus cover a wider current range. The current of the power supply has been increased in steps of 5 A which leads to measurement intervalls of 15 A up to maximum current of 300 A. The data points have been approximated with a linear fit $y = m \cdot x + b$ with a slope of $m = 0.00292\ V/A$ and an intercept of $b = -0.00465\ V$. The fit has a coefficient of determination of $R^2 = 0.99999$ which verifies the linear dependence of the output voltage on the current.

3.8 Calibration of pyrometers

A pyrometer converts the measured intensity of infrared light to temperature. In order to determine the correct temperature from the emission of infrared light from the sample's surface, the

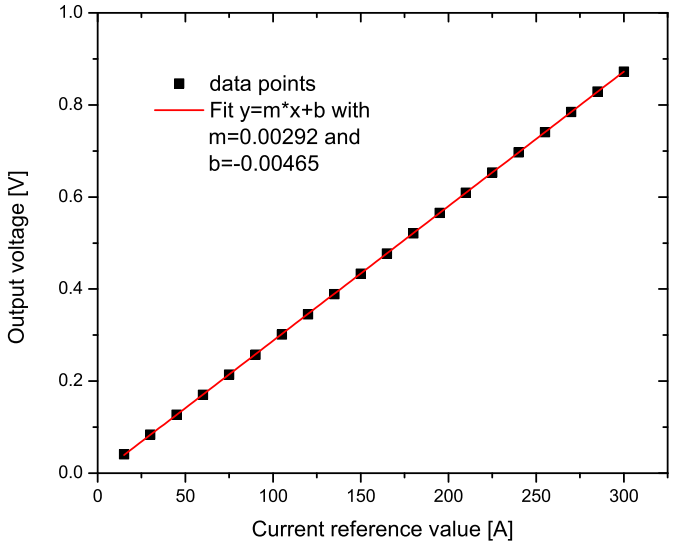

Figure 3.5: Output voltage of the Hall sensor as a function of output current of the power supply.

pyrometers had to be calibrated prior to the measurement. The pyrometers used in these measurements, KGA 740 and IGA 740, are single color pyrometers, i.e. they measure the emitted light of one wavelength within a certain wavelength range. Upon heating, the factor between the temperature and the radiant power, the emissivity ϵ of the sample, is changing due to its temperature dependence. However, for single color pyrometers the emissivity is set prior to the measurement and cannot be changed in a very fast heating experiment on the appropriate time scale. Therefore, we needed to choose a value for the emissivity in the measurements which is, in general, only correct for one temperature and accordingly leads to a systematic error in the temperature measurement.

In the calibration, we determine the temperature of a nickel disc with a thermocouple of type K which is welded on the disc's surface. At the same time, we measure the temperature of the nickel disc with the pyrometer on a spot directly next to the thermocouple. The nickel disc is mounted on a heater using a Macor suspension. The input voltage for the heater is controlled via a phase-fired controller.

In order to account for possible changes in the emissivity due to oxidation, the nickel alloy has been annealed for several hours at 1273 K. Afterwards, the alloy was fully oxidized. Additional heating until 1273 K did not affect the emissivity anymore. The temperature of the thermocouple as a function of output voltage of the pyrometer KGA 740 is plotted in Fig. 3.6.

The emissivity of the pyrometer has been set at a temperature of 573 K. For this purpose, the

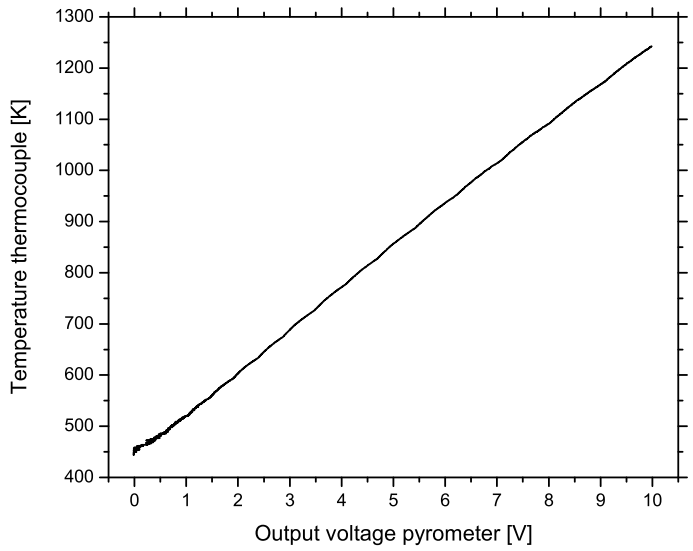

Figure 3.6: Output voltage of the Hall sensor as a function of output current of the power supply.

temperature measured by the pyrometer has been calculated from the output voltage by the simple linear approximation

$$T_P = 84 \cdot U_{out} + 433. \tag{3.1}$$

This approximation is motivated by the range of the output voltage U_{out} from 0 to 10 V and the range of the detected temperature T_P of 433 - 1273 K. At a thermocouple temperature of $T_T = 573K$ the emissivity of the pyrometer has been tuned until the temperature T_P calculated from the output voltage of the pyrometer matches T_T.
It is visible that the output voltage range matches the nominal temperature range well. This points to the fact, that the temperature dependence of the emissivity of the oxidized nickel is not noticeable.

3.9 Sequence of a rapid heating measurement

The capacitor discharge is fully controlled by a Labview program. The program does not only control the discharge, it also provides a certain security since there are a couple of LEDs installed which inform the user about the status of the discharge. Red LEDs light up whenever it is dangerous to touch the setup, which is during charging of the capacitor and after a certain

waiting after the discharge. The waiting time is set by the user before the measurement in order to make sure that the capacitor is indeed discharged. Green LEDs turn on when it is save to touch the setup and, for instance, exchange the sample. In this moment, the capacitor is connected to a 3.3 kΩ protective resistor which leads to a discharge of the capacitor to 36.8 % within 3.3 s, in case it was not entirely discharged during the measurement.
At the first stage of the measurement the program connects the capacitor to the power supply for 30 s. The time is variable but it is shown to be sufficient to charge the capacitor with the supplied voltage. Afterward the capacitor is disconnected from the power supply and the discharge is initiated by a little voltage pulse on the thyristor. After another waiting time of 5 seconds the discharge is expected to be over and the user is asked to save or discard the measurement. After the user finished this step, the capacitor is connected to the protective resistor and it is save to exchange the sample.

3.10 Characteristics of the temperature profile during rapid heating

The capacitor discharge rises the temperature T_s of the sample after the time t to a value which can be calculated by [77]

$$T = T_0 + \frac{R_S C U_{tot}^2}{2C_P} \left\{ 1 - \exp\left(-\frac{t}{\tau}\right) \left[1 + \frac{t}{\tau} \left(1 + \frac{t}{2\tau} \right) \right] \right\} \tag{3.2}$$

This equation does not account for the glass transition. An exemplary measured temperature curve of a metallic glass with nominal composition $Zr_{65}Cu_{27.5}Al_{7.5}$ is displayed in Fig. 3.7. Additional processes can lead to further increases or decreases. The glass transition is sometimes accompanied with an overshoot in the heat flow which indicates an endothermal reaction. This causes a little kink in the temperature curve. Crystallization is an exothermal process which causes an additional increase in the temperature curve. In Fig. 3.7, the second temperature increase is caused by crystallization. In this case, crystallization is well separated from the temperature increase due to the capacitor discharge but, particularly at higher heating rates, the discharge may overlap with crystallization. The apparent delay in the temperature increase in comparison to the current increase in Fig. 3.7 is related to the lower temperature limit of the pyrometer of 433 K. Naturally, the temperature of the sample increases when there is a current flowing but the pyrometer cannot detect it before the temperature overcomes the lower temperature limit of 433 K.

Eq. 3.2 shows that the heating rate of sample can be modified either by changing the

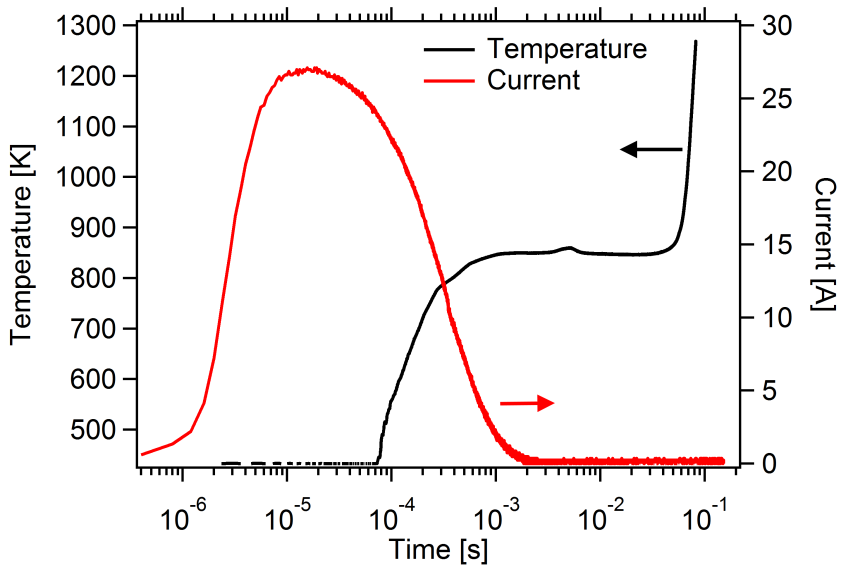

Figure 3.7: Exemplary temperature and current versus time curves.

capacity of the capacitor or by varying the charge voltage. The first one also affects the characteristic discharge time $\tau = R \cdot C$ of the capacitor and therefore it is easier to change the charge voltage U_{tot}.

As mentioned in section 3.4, we also performed several measurements with a multiple discharge technique. In these measurements, we discharged four small capacitors after the first main capacitor one after the other (Fig. 3.8). The main capacitor raises the sample temperature to a value around or above the glass transition temperature, here 610 K. At this point the other capacitors were discharged after a certain waiting time. This causes every time a little increase in the sample temperature of about $3 - 7$ K. It is visible that apart from the little increases due to the discharges, the temperature remains almost constant. There is almost now energy exchanged with the environment on such short timescales. Therefore, we treated this as an adiabatic situation and calculated the specific heat accordingly (see section 4.5.2).

3.11 Measurements at the High Energy Synchrotron beamline P07 at DESY

We performed rapid heating measurements at the synchrotron beamline P07 of PETRA III at DESY. The X-rax measurements with a beam energy of 70 keV and a corresponding wavelength of λ=0.117712 Å were performed in-situ during heating. For these measurements, we used the two-dimensional flat panel X-ray detector Perkin Elmer XRD 1621 with 2048×2048 pixels and a

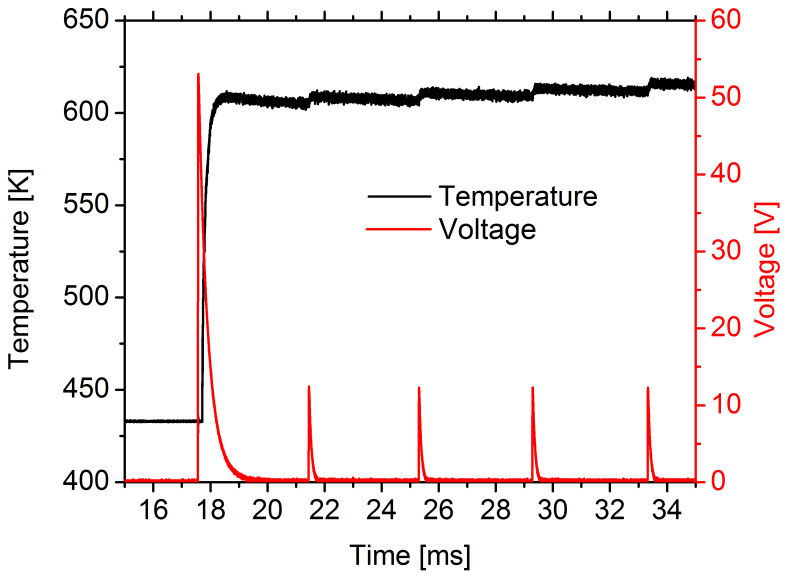

Figure 3.8: Temperature profile of a metallic glass ribbon of nominal composition $Pd_{77.5}Cu_6Si_{16.5}$. Additional to the initial main capacitor discharge, four smaller capacitors have been discharged after the sample reached a temperature of about 610 K. Between the discharges, there was time interval of 4 ms.

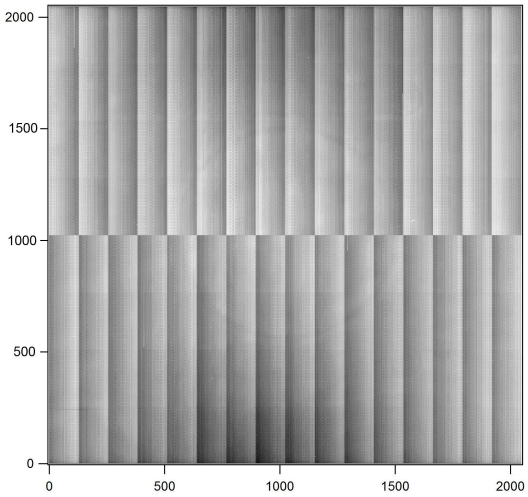

Figure 3.9: Raw detector image without beam.

pixel size of 200×200 μm [78]. This detector has a read out frequency of 15 Hz and, accordingly, a temporal resolution of 66 ms. The read out procedure of this detector is important for the subsequent data analysis and therefore, it is explained in this paragraph in more detail.
The detector Perkin Elmer XRD 1621 is an amorphous silicon flat panel detector [78]. Flat panel detectors consist of active matrix arrays of thin film transistors (TFT). They use an

indirect conversion as a detection method for the X-ray photons. This means that the X-ray beam first hits a scintillator which converts the ionized beam into visible light. This light is converted into an electronic signal by an array of photodiodes which can be detected by small structures of amorphous silicon [79, 80].
In the raw image of the detector it becomes clear that the detector is read out in 32 sections of 128×1024 pixels simultaneously (Fig. 3.9). Each of these sections is read out from top to the bottom which takes about 66 ms. This means that each pixel of one section is illuminated for 66 ms before it is read out but since the pixels are not evaluated at the same time, each of them contains information from different times. This effect has to be considered when the X-ray image is split up by the chopper system into section which are also illuminated at different times.

3.12 The chopper system

This section has been reprinted with permission from [81]. Copyright 2014, AIP Publishing LLC. During our experiments, it was necessary to increase the temporal resolution of the 2D flat panel detector from Perkin Elmer XRD 1621 of 66 ms (15 Hz) available at beamline P07 at PETRA III, DESY. Due to the isotropic, disordered structure of these materials, the X-ray diffraction patterns have a circular shape and contain nearly the same information in each direction from the beam center. Thus, in order to obtain momentary structural information, it is only necessary to know the diffraction in one direction from the beam center and it is not necessary to integrate over the entire diffraction ring.

Therefore, we installed the chopper system between the sample and the detector so that the diffracted beam is temporally partly blocked by the chopper (Fig. 3.10). The chopper divides the diffraction pattern into 13 sections and these sections are illuminated successively. Hence, with the aid of the chopper system, the temporal resolution could be increased from 66 ms (15 Hz) up to 5.1 ms (195 Hz).

The whole system consists of two axis (labeled with "Axis A" and "Axis B") and the chopper suspension (Fig. 3.11a). There are two chopper discs integrated in the chopper suspension which rotate in opposite directions at different frequencies. Axis A is driven by the brushless EC servomotor nanotech DB87M01-S with a nominal torque of 1.4 Nm. It rotates with the same frequency as the fast chopper disc. On this axis, there are two gears and two discs for photo sensors attached. The sensors are used to record the moment when a new section on the detector starts to be illuminated. The first gear on the axis has 40 teeth (and a diameter of d = 40 mm) and the second one has 72 (d = 110 mm). Both are connected to gears on axis B, the first is directly connected to another gear with 124 teeth (d = 130 mm) and the second one

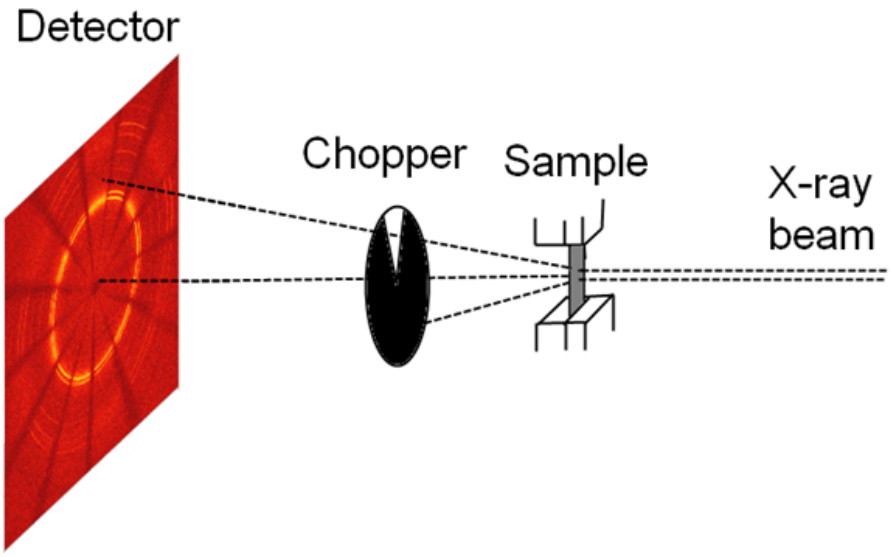

Figure 3.10: Setup at the synchrotron beamline P07 at DESY.

via a gear belt to a gear with 18 teeth (d = 25 mm). The latter gear is attached to the axis via a ball bearing, so that it can rotate in the opposite direction than this axis itself. Both gears on the second axis are coupled via gear belts to the outer suspension of the chopper.
The choppers are mounted on the outer edge to a gear with 72 teeth instead of a central suspension in order not to lose any information close to the beam center (see Fig. 3.11b) and to achieve a higher mechanical stability. The chopper discs are made of lead and rotate in opposite directions. The discs have a thickness of 3 mm. At an energy of the X-ray beam of 70 keV, this thickness causes a decrease of the intensity by a factor of $3.18 \cdot 10^{-6}$. Apart from this, the discs have an outer diameter of 100 mm and a remaining lead center with a diameter of 3 mm. The first, fast rotating disc has one slit and the second slow one has six slits (Fig. 3.11d). These numbers are variable but this combination has been proven to fulfill the required conditions discussed below while maintaining a sufficient mechanical stability of the lead choppers. The frequency of the fast chopper is adjusted to be two times the read out frequency of the detector. Fig. 3.11c shows a photograph of the chopper system used at the beamline P07 at PETRA III, DESY.
For the construction, it is helpful to know that the ball bearings on the first and on the second axis must be made for 1800 rpm. The ball bearing which is used to attach the first gear on axis B need to stand 3600 rpm since the gear rotates in the opposite direction than its axis. Additionally, in order to keep the gear belts under tension, we attached the chopper suspension to a movable rail and added another movable clamping fixture for the gear belt between axis A and axis B. Please note that this clamping fixture is not included in the schematic drawings

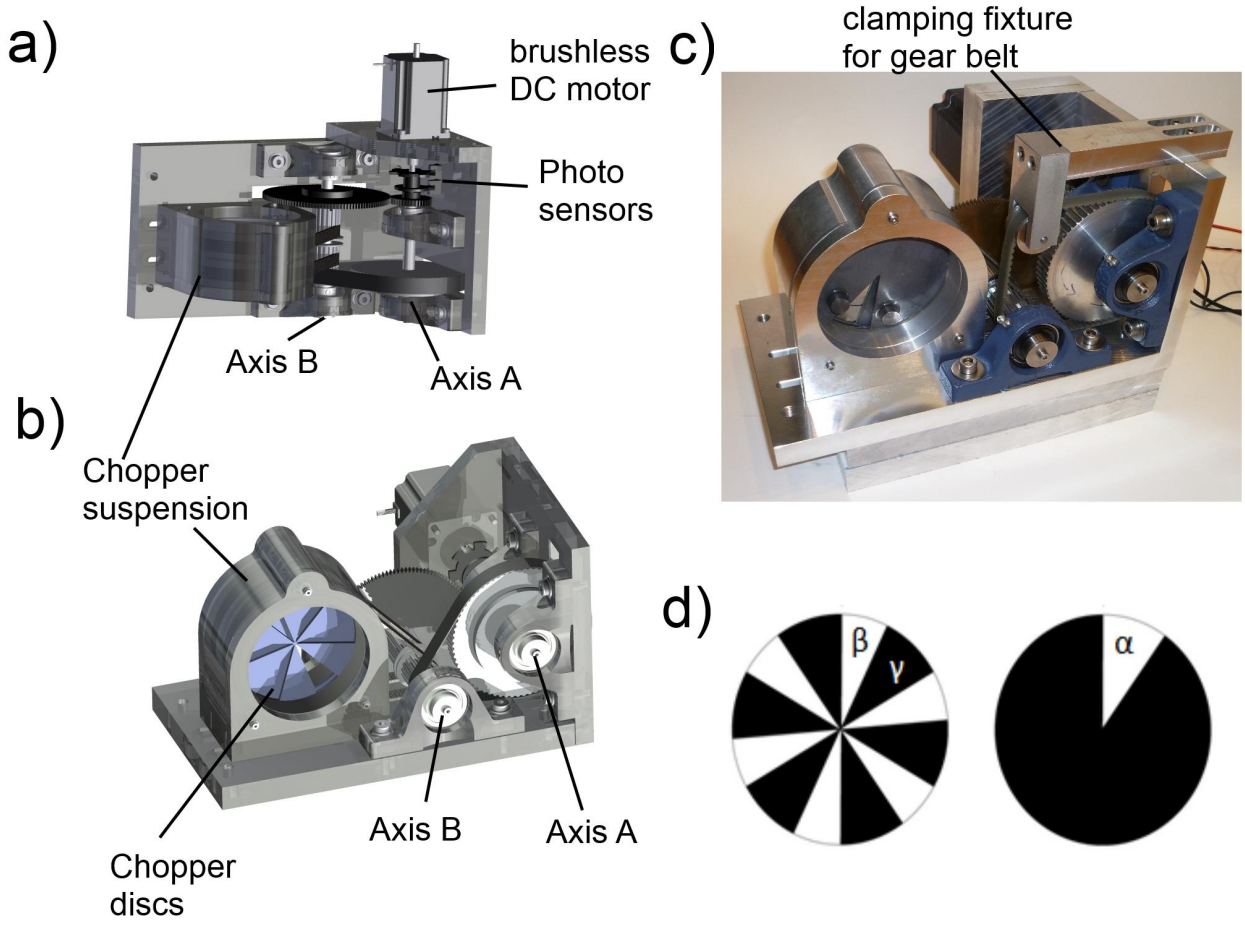

Figure 3.11: a) Technical drawing of the chopper system (top view), b) Technical drawing of the chopper system (front view), c) Photograph of the chopper system, d) the two chopper discs.

in Fig. 3.11a and 3.11b but in the photograph in Fig. 1c. On top of the first, fast rotating chopper disc with only one slit, we also added two round lead pieces in order to compensate the asymmetric mass distribution due to the single slit of this chopper disc.

In order to check the performance of the chopper, we calculated the position of the slits as function of time (Fig. 3.12). The grey regions correspond to the positions of the slits at a certain time. White regions occur at the angle and time where two slits overlap and thus this particular area on the detector is illuminated. An overlap of the angles of the white regions would lead to the situation where a certain angle on the detector contains information from different time zones. This means that a discrimination between the information during the analysis would not be possible. Therefore, it is essential that the angles of the white sections do not overlap (as it is shown by the red lines in Fig. 3.12). This condition is manifested in the following inequation which relates the fraction between the rotational periods of the two

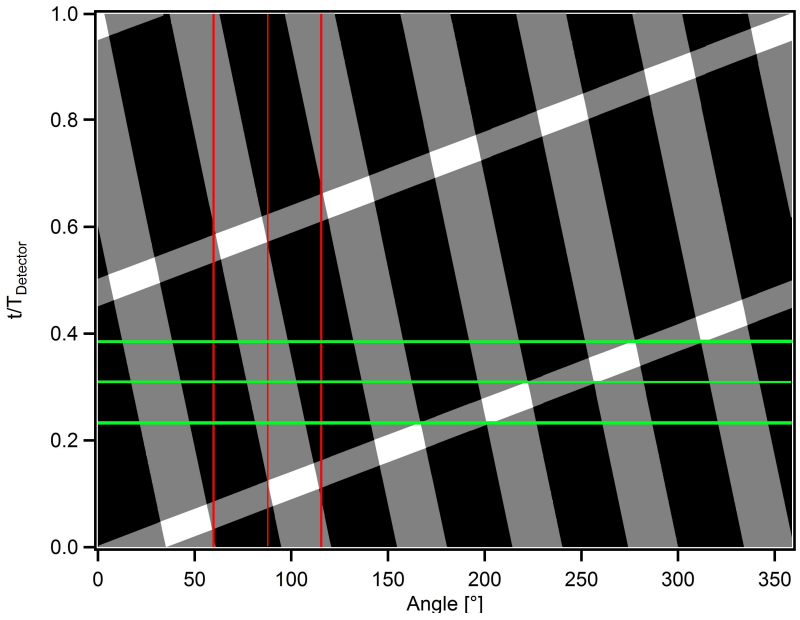

Figure 3.12: Progress of the two chopper discs plotted in a time versus angle plot. The graph demonstrates the time when certain sections are illuminated (white regions). The green and red lines show that there is no overlap between neighboring sections.

choppers $\frac{T_2}{T_1}$ and the sizes of the slits

$$\frac{360° - \alpha}{\beta} \geq \frac{T_2}{T_1} \geq \frac{360° + \alpha}{\gamma} \tag{3.3}$$

where α is the opening angle of the only slit of the fast chopper, β is the opening angle of the six slits of the slow chopper and $\gamma = 360°/n - \beta$ reflects the angle between two slits of the slow chopper. The factor n is the number of slits in the slow chopper.
Additionally, we tried to avoid that the times of the white sections of different regions overlap (as indicated by the green lines in Fig. 3.12). This is not an essential condition but simplifies the analysis. The condition relating the opening angles of the slits of the two choppers is reflected in the equation

$$\beta = \frac{360°}{n} - \alpha \tag{3.4}$$

When constructing the chopper system, one can choose the parameters in the way that a section starts exactly at the same angle and time where the previous one ended. So, there is not gap neither in time nor in the angle between two adjacent white regions in Fig. 3.12. This choice is considered to be the most efficient case since the sections on the detector are largest and longest illuminated. It occurs when the two expressions on the left and on the right side in inequation 3.3 are equal and can be solved when considering equation 3.4. This combination results in

$\alpha = 32.7273$ and $\beta = 27.2727$. These values, in turn, lead to the ideal fraction between the rotational periods of $\frac{T_2}{T_1} = 12$. This efficient construction has a technical disadvantage, which is the difficulty to discriminate between two neighboring sections. Therefore, we slightly varied the parameters to the values of $\alpha = 35°$ and $\beta = 25°$ and a fraction between the rotational periods of $\frac{T_2}{T_1} = 12.4$. Thus, there is always a little gap remaining between two sections in the detector image but there is no gap in time between two sections (see Fig. 3.13).

The chopper system was first used during our beamtime at P07 at DESY in Hamburg in

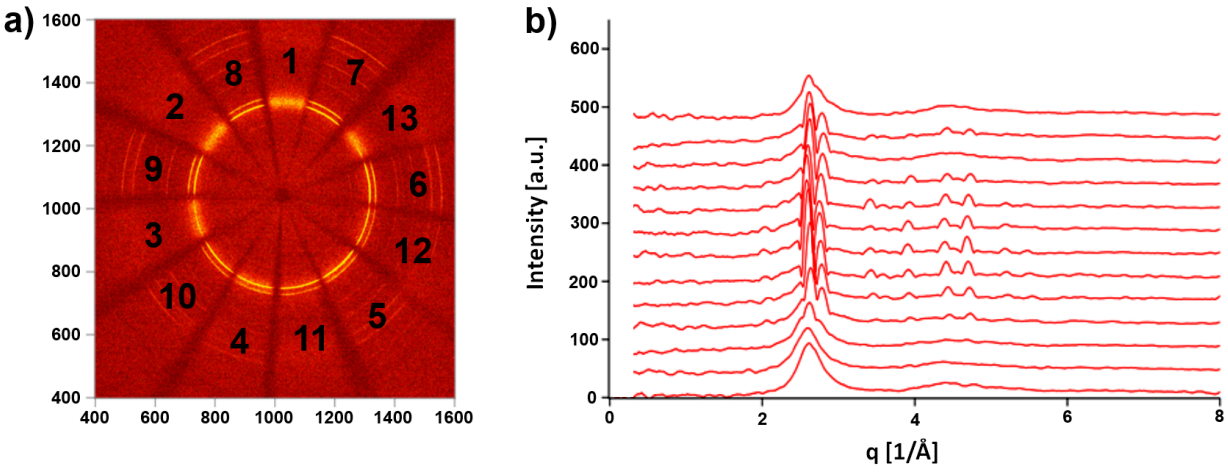

Figure 3.13: Output voltage of the Hall sensor as a function of output current of the power supply.

2012. We investigated the crystallization of metallic glasses during fast heating. At high heating rates the crystallization process takes place rapidly. With the aid of the chopper, we were able to resolve the formation and growth of crystals even at high heating rates (Fig. 3). The numbers in Fig. 3a show that neighboring sections are not temporally sequenced but the second-next neighboring ones are. The chopper system enables a significant increase of the temporal resolution, in our case, by a factor of 13. Particularly for high energy synchrotron beams, this technique is a simple and cost-efficient way to increase the temporal resolution. The signal to noise ratio is considerably decreased, in the current setup by a factor of 169. However, the signal to noise ratio is sufficient to clearly resolve the crystallization behavior of metallic glasses. In principle, the chopper system can be applied to any, also faster framing 2D detector. Given a different detector, the speed of the motor must be set to be as twice as high as the read out frequency. Currently, the installed motor, with 3000 rpm, limits the use of the chopper system to detectors with a temporal resolution of 40 ms (25 Hz). However, there are much faster accurate brushless motors available. For example, with a motor of 13000 rpm and appropriate ball bearings the chopper system could be used for detectors with a resolution of about 9.2 ms (108 Hz) and accordingly increase this temporal resolution up to 0.7 ms (1408 Hz).

This value even exceeds the highest temporal resolution of current Pilatus detectors. Given a beam with a higher intensity, the temporal resolution could also be increased by modifying the number of slits n of the second slow chopper. The fraction between the rotational periods and the angle of the slits can be calculated using ineq. 3.3 and eq. 3.4.

3.13 Sequence of the rapid heating measurements at the synchrotron beamline

During the measurement, it was necessary to synchronize several devices in order to record the X-ray pattern and initiate the discharge at the right moment. Apart from the discharge, the chopper and the detector we also controlled a fast piezo shutter which was installed in front of the sample and could either block the beam or let the entire beam pass. It has an opening time and closing time of 2.5 ms.

Before we initiated the discharge, we incorporated a sequence of opening and closing of the

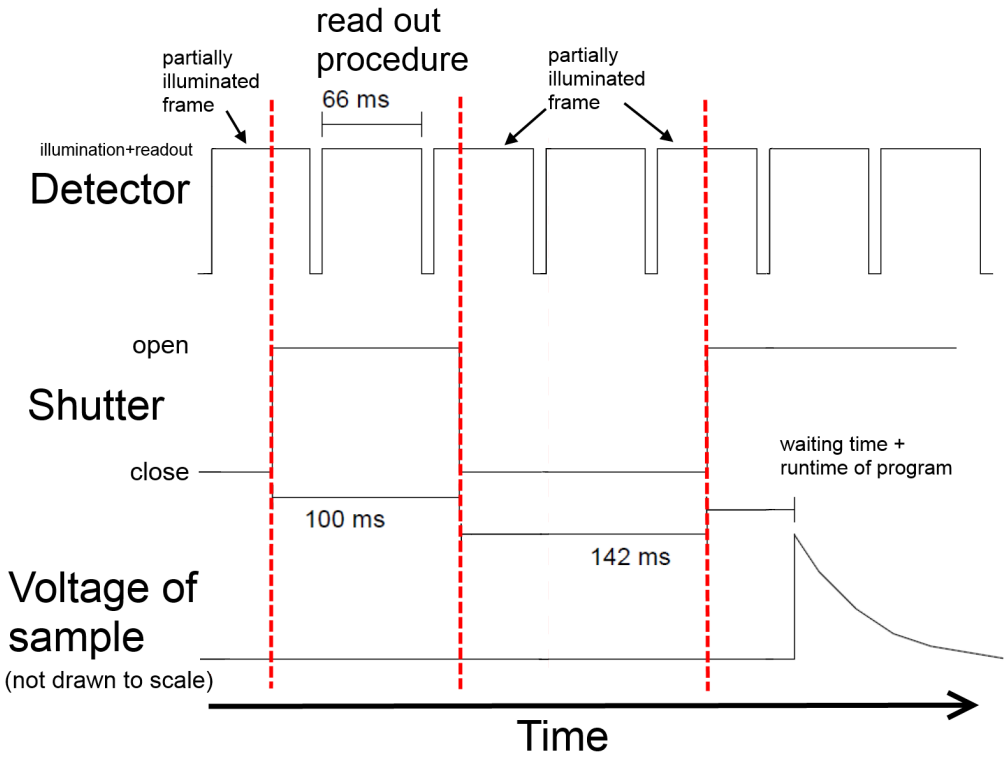

Figure 3.14: Schematic drawing of the synchronization of the detector, the fast shutter and the capacitor discharge.

beam shutter once (Fig. 3.14) while he chopper was already running. The opening and closing

was dependent on the TTL-signal which reflects the read out periods of the detector. Before the program was started, the shutter was closed. If the detector is in a read out period when the program starts, the shutter open for 100 ms and closes afterwards. Again, if the detector is within a read out period in this moment, the shutter starts to wait exactly 142 ms and opens afterwards. After this final opening, it requires the runtime of the program and a certain waiting time which was previously set by the user until the discharge is initiated.
With this opening and closing procedure of the shutter, we obtain exactly three X-ray patterns which has been only partly illuminated. More precisely, there are two images where only the last sections are illuminated and one image in which only the first sections are illuminated. These partly illuminated images unambiguously allow the determination of that section which is illuminated first in each X-ray pattern for each measurement. Additionally, we can make a statement about the overlap of the illumination of the 13 sections caused by the chopper and the readout of the 32 sections of the detector and correct pattern accordingly.

3.14 X-ray image processing

For the data analysis, it was necessary to determine the center of the X-ray beam on the detector. For this purpose, we installed a polycrystalline CeO_2 sample in the beam and fitted the diffraction rings with an ellipsoidal function. The analysis was performed using the software fit2D and afterwards the results were confirmed with a program written in the data analysis software IGOR. We fitted 20 points which were distributed along the sharpest diffraction ring with the highest q-value with the attempt to decrease the error in this procedure. The fit with an ellipsoidal function returned that the beam center is located at the pixel x=1024 and y=1044 and that the two axis of the ellipsoid are equally long. Thus, the diffraction rings have a circular shape which verifies that there is no tilt in the detector. This result was confirmed in the second procedure and it was always considered when the image was turned.
In the following, the order is explained in which each diffraction pattern is analyzed. All points in this procedure were performed automatically using an IGOR program.
In the first step, the dark frame was subtracted from the diffraction pattern of the sample. The dark frame was recorded before each measurement with a closed shutter. It contains the same image noise and the same dead pixels as the measurement and, therefore, a subtraction of the dark frame reduces the noise in the recorded diffraction pattern of the sample.
Afterwards, the program assigns a radial distance $r_{x,y}$ in millimeter from the beam center (c_x, c_y) to each pixel (x, y) by the equation $r_{x,y} = 0.2 \cdot \sqrt{(x - c_x)^2 + (y - c_y)^2}$. The factor 0.2 results from the pixel length. With this equation it was possible to determine the scattering

vector by

$$q_{x,y} = \frac{4\pi}{\lambda} \sin\left(\arctan\left(\frac{r_{x,y}}{d}\right)/2\right) \tag{3.5}$$

with the wavelength of the X-ray beam $\lambda = 0.17712$ Å and the distance of the sample to the detector $d = 800$ mm. Additional to the distance to the beam center, we assigned an angle to each pixel. This was necessary in order to relate each pixel to its corresponding section given by the chopper. Therefore we defined the horizontal line from the beam center to the outer right edge of the X-ray pattern as the angle zero and accordingly 360°. This line is arbitrary and does not affect the following analysis.

As mentioned earlier, the parameters of the chopper system has been chosen in the way that there is always a small region between two neighboring sections which is not illuminated at all in order to discriminate between the two sections. In this step the program separates the sections caused by the chopper. It is doing this by finding the minima in the integral of the intensity over the radial distance as a function of angle (Fig. 3.15). The minima were determined by the

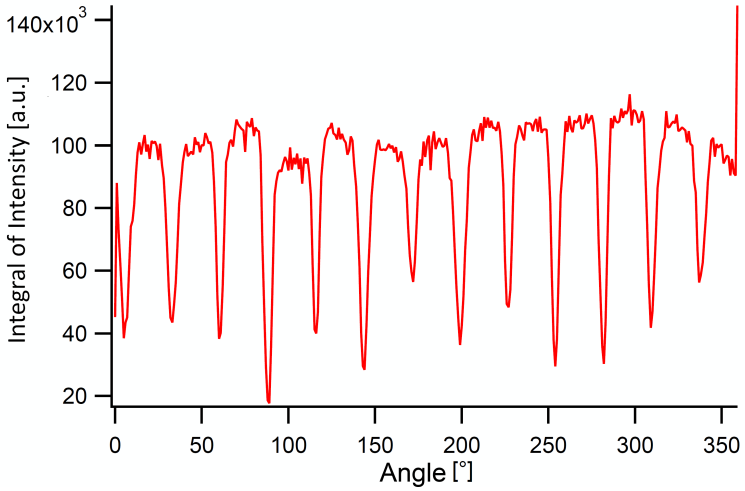

Figure 3.15: Example of the integral of the intensity over the radius as a function of angle.

following algorithm. The program calculates the average value of the integral of intensities and subtracts this value from the integral. Then, it determines the minima from all negative and connected regions. Afterwards, the program lets the user check this first attempt to find the minima and the user has the chance to correct a minima in case it was determined wrong. For the correction, the user has to give a lower and an upper limit where the minimum is located in between. After this check, the minima are found correctly and they are stored. For the next frame, the program tries to find the minima in the close vicinity of the section divisions of the previous frame and lets the user check this attempt as well.

The intensity as a function of scattering vector q has been integrated over all angles which

belong to the same section. It has been normalized by the number of pixels of one section which belong to the same angle.
Eventually, in the final step, the background has been subtracted from the intensity. The background has been determined from five different measurements without sample but with the chopper running. We performed all steps as mentioned above and obtained, accordingly, the intensities for 13 sections in each measurement. We observed that the intensities from different sections differ slightly. Therefore, we averaged the background intensities of sections 1-4, sections 5-7, sections 8-10 and sections 11-13 of all five measurements and, hence, we obtained 4 different curves for the background intensities (Fig. 3.16). Particularly, it is noticeable that the background for sections 11-13 show an increase at high q-values. The reason for this behavior is not known. As mentioned earlier, a tilt in the detector in respect to the beam can be excluded as a possible explanation for the different backgrounds. These four different background curves have been subtracted from the corresponding sections of each measurement.

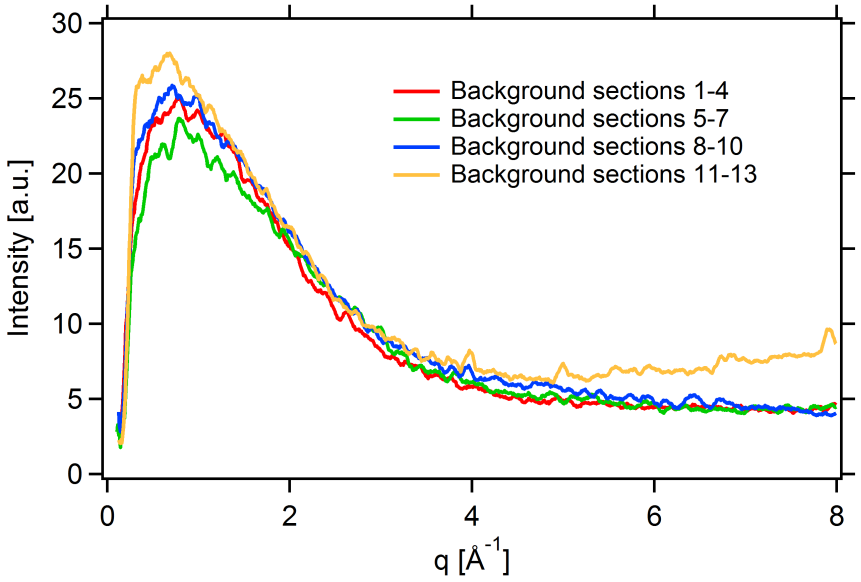

Figure 3.16: Plot of the four different backgrounds depending on the region on the section.

3.15 Determination of the first section in the temporal order

In order to make an exact decision which section is the first in the temporal order in each frame, we analyzed the three frames which have been only partly illuminated before each measurement

(Fig. 3.17). As mentioned above, the sections of two of these three frames (Fig. 3.17a,c) belong to the last illuminated sections of the temporal order and the sections in the other frame (Fig. 3.17b) correspond to the first illuminated sections. This fact can also be seen in Fig. 3.14.

The 13 sections in Fig. 3.17 have been labeled with the letters A-M. The labels always start

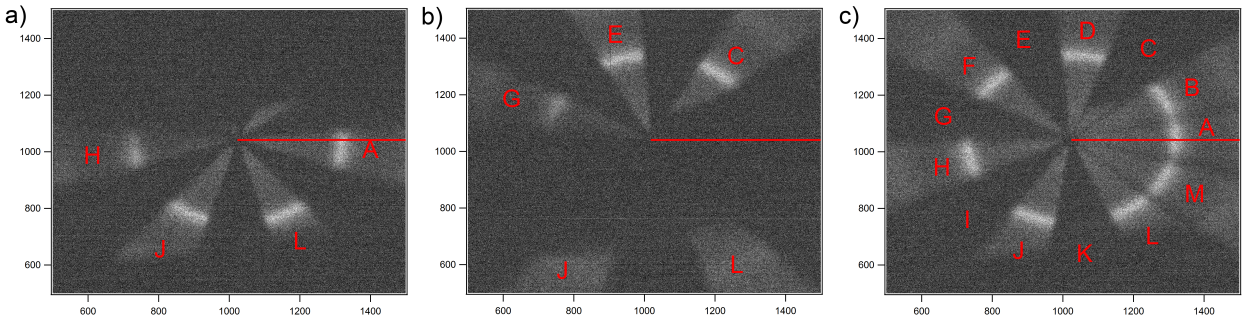

Figure 3.17: Example of the three frames which have been partly illuminated before each measurement in order to determine the temporal order of the sections. The red line starts in the beam center and determines the angle zero.

with the letter A at the angle zero (red line) and continue counterclockwise. Thus, these labels do not indicate the temporal order, but the eventual temporal order of illumination will also be counterclockwise. In Fig. 3.17a, there are four sections (H, J, L, A) illuminated and therefore it is obvious that section A is the very last section illuminated in this frame. Section A is also the very last section in a certain number of frames of the whole measurement until the sections have turned as much as the next section crosses the angle zero and is labeled with A from that moment on (see section 3.16). Consequently, section C is the very first illuminated section in this measurement. This can be seen in Fig. 3.17b where the first sections C, E and G are illuminated. The assignment of the first section may also change during the progress of the measurement in the same manner as the last one could. Fig. 3.17c confirms the previous observation, that section A is illuminated at the very end of the frame. In this figure, the five sections C, E, G, I, and K from the beginning of the frame have not been illuminated.

3.16 Correction of sections

The intensity of the sections given by the chopper system needed to be corrected in various ways which will be explained in this section. One of the systematic errors, which we could not avoid during the progress of the measurement, was that the start of a new section matches with the start of a new frame. Mostly, parts of the first section of a frame are already illuminated in the previous frame. This behavior can be seen in section C in Fig. 3.17b. A small part of section C has already been illuminated in the frame Fig. 3.17a but the bigger part of section

C is illuminated in the subsequent frame. In Fig. 3.17b it is also visible that a small part of section C is missing which was already illuminated in the previous frame. In fact, we would define this section as the last section if the bigger part of the section had been illuminated in the previous frame. This error has been corrected by replacing the corresponding pixels from the first section by the pixels from the same section of the previous frame.
Another systematic error in the data acquisition results from the temporal mismatch of the readout of the detector and the illumination time of a section from the chopper. Sometimes the readout of a certain part of the section took already place when it illuminated by the chopper. Consequently, this section is split up and a part of the section is in the subsequent frame. This behavior can be observed in sections J and L in Fig. 3.17. The parts at high q-values of sections J and L correspond to the frame which were recorded just before the frames which are shown in Fig. 3.17a,b and c. The pixels in the sections which are affected from this error have been replaced by the pixels which fit in the temporal order.
The last error which is explained here results from a little mismatch in the readout period of the detector and the rotational period of the chopper. The rotational period of the chopper has been monitored using two light sensors additionally to the speed control of the brushless servo-motor. This period was constant over time and it was matched to the nominal readout period of the detector. However, it is obvious that the positions of the sections caused by the chopper change a little between two subsequent frames. As a consequence, the sections between two frames seem to move slightly counterclockwise. This behavior can be observed in a movement of the minima in Fig. 3.15 and is about 1-3° between two frames. As mentioned above, this shift can cause a change in the section which overlaps with the angle zero and therefore it can also change the temporal order. This change in the temporal order can also be observed in the minima in Fig. 3.15 and would be corrected in case it occurs.
Therefore, all the aforementioned errors can be corrected and do not have consequences on the quality of the result.

3.16.1 Temporal assignment of temperature to the X-ray frames

For the experiment at the beamline P07, it was necessary to use two different computers. The first one controlled the detector and recorded the X-ray frames. The second one regulated the capacitor discharge and recorded the temperature, voltage, current, the chopper signal from the light sensors and a TTL signal which monitors the readout periods of the detector as shown in Fig. 3.14. In order to compare both measurements, it was necessary to assign the same time axis to both data files. This was done in two ways. First, we looked at the TTL

signal of the detector together with the signal from the light sensors and the temperature (Fig. 3.18). In this graph, it is possible to determine the moment when the a new detector frame

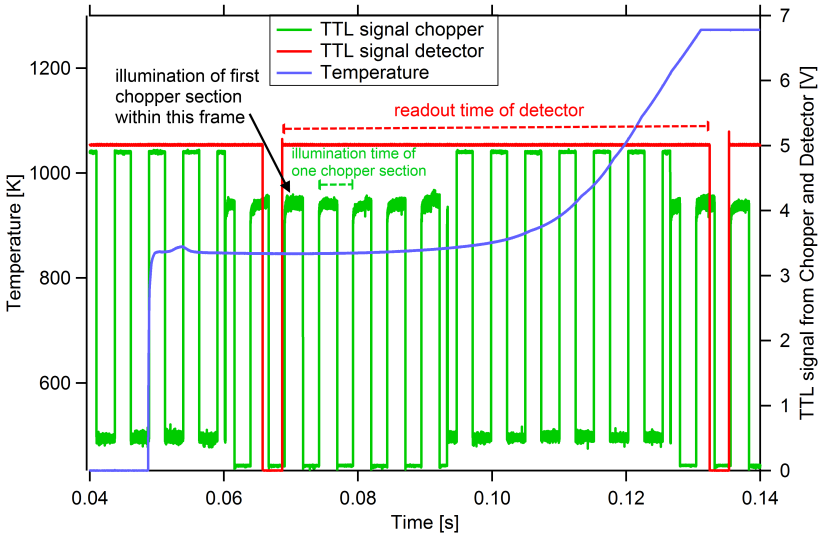

Figure 3.18: Exemplary temperature curve, TTL signal from the detector and the TTL signal from the light sensors of the chopper system plotted versus the same time axis.

starts. This is when the TTL signal of the detector rises to a value of 5 V. In this particular example, the temperature rises due to the capacitor discharge at a time around 0.048 s. This moment is difficult to determine in the X-ray images and is therefore not suitable for a time assignment. Additionally, the temperature starts rising again at a time around 0.10 s. This indicates a crystallization process which is well visible in the X-ray images. Thus, this frame can be identified and used to assign a single time axis to the X-ray frames and the temperature measurements.

Another method deals with the evaluation of those measurements in which the sample broke during the discharge. In these measurements, the moment of breaking has a signature in temperature since it drops quickly because the pyrometer does not point on the sample surface anymore and it also has a signature in the X-ray images since the sample mostly leaves the beam and there is only the background recorded from that moment on. We used method to determine the time it takes from the last opening of the shutter until the start of the discharge (see Fig. 3.14). This time is the sum of a waiting time set by the user and the runtime of the program. We evaluated 8 measurements in which the sample broke during the discharge. Between the last opening and the disappearance of the diffraction pattern, there are in average 21 sections which corresponds to 107.1 ms. This time interval is consistent between different measurements and therefore also be used to assign the temperature to the X-ray data. In comparison, this assignment of the time to both, temperature and X-ray data, agrees well with

the previous method.

Chapter 4

Results

4.1 Corroboration of the amorphicity and the composition

For the interpretation of our measurements, it is most essential to validate that the metallic glass ribbons used in the present measurements have a purely amorphous structure after casting. Several ultrafast heating measurements were performed at the synchrotron beamline P07 at PETRA III at DESY. In these measurements the amorphicity was confirmed by evaluating the 2D X-ray frames. We integrated one of those frames which were recorded before the discharge was initiated for this purpose. One example of such frames is shown in Fig. 4.1.

In this case, the separation of the diffraction image by the chopper was not taken into account

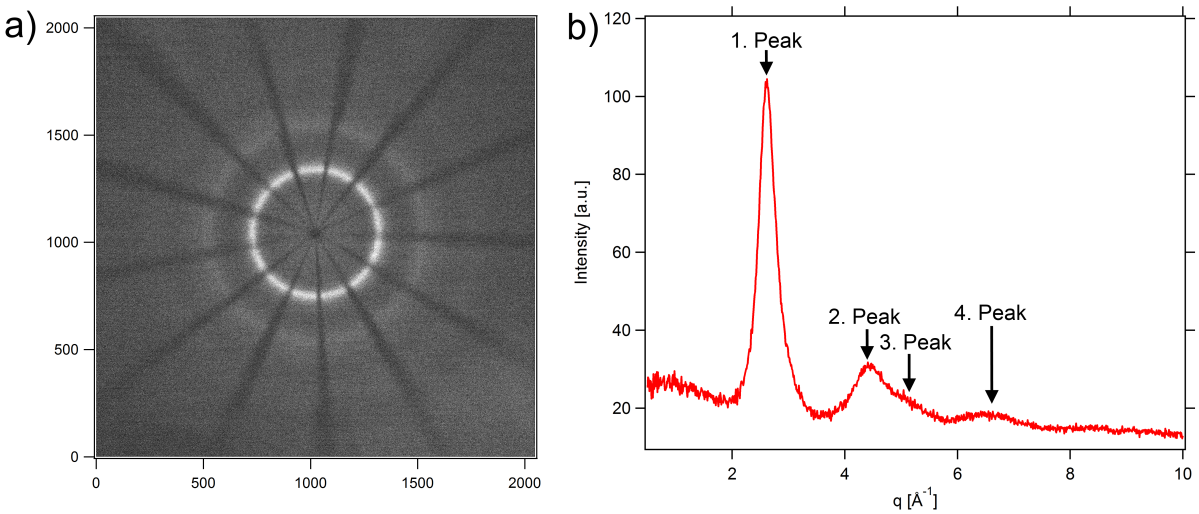

Figure 4.1: a) Exemplary X-ray image of an amorphous sample before the discharge was initiated. b) Diffraction intensity integrated over 360° in the q-range from 0 to 10 Å^{-1}.

for the integration, i.e. that the intensity has been integrated over the entire diffraction ring. In the q-range between 0 and 10 Å there are 4 broad diffraction peaks visible. The first peak occurs at $q_1 = 2.61$ Å^{-1}, the second one at $q_2 = 4.43$ Å^{-1}, the third peak appears as a shoulder of the second one with a maximum at $q_3 = 4.99$ Å^{-1} and the fourth peak is located at $q_4 = 6.56$ Å^{-1}. These broad peaks indicate the purely amorphous structure of the sample since there is no signature of sharp peaks due to Bragg reflection. Please note that the background has not been subtracted in Fig. 4.1. That is why there is a slightly quadratic polynomial decrease in the noise level.
As mentioned in section 3.12, each section which is caused by the chopper is illuminated for about 5.1 ms. Therefore, the intensity, when integrated over the entire diffraction ring, is reduced by a factor of 13 in comparison to a X-ray frame recorded without the chopper at the same temporal detector resolution of 66 ms. Here, the signal to noise ratio SNR when considering the relatively high noise in the q-range of $1-2$ Å^{-1} SNR=18.1 and when considering the low noise in the q-range of $7-8$ Å^{-1} it is SNR=47.2.

4.2 Analysis of composition

We performed energy dispersive X-ray measurements with 9 different ribbons. For each ribbon we analyzed an exemplary sample on six different positions which are distributed over the entire surface. All results of the analysis are presented in Appendix A. In this section we only show the average values from the six positions for each sample together with the error which is calculated from the standard deviation. Apart from the results, each table also contains information about the nominal composition.

Ribbon	A	A (nom.)	B	B (nom.)	C	C (nom.)
Zr [at%]	63.1 ± 0.1	65	64.0 ± 0.3	65	43.4 ± 0.3	45
Cu [at%]	29.1 ± 0.2	27.5	28.3 ± 0.4	27.5	46.4 ± 0.5	45
Al [at%]	7.8 ± 0.1	7.5	7.8 ± 0.1	7.5	10.2 ± 0.2	10

Table 4.1: Average compositions of samples A, B and C.

In the tables, it is visible that the deviation of the actual composition from the nominal composition is usually about 1 at%. The measured composition of sample H is very close to the nominal composition. While the compositions of the sample B and F are fairly close to each other, the measured composition of A deviates stronger from the nominal one and also from the samples B and F in the Cu and the Zr content. Also the measured compositions of samples D and H are quiet similar while the actual composition of E differs from the two.

Ribbon	D	D (nom.)	E	E (nom.)	F	F (nom.)
Zr [at%]	65.5 ± 0.3	66.5	63.2 ± 0.2	66.5	63.8 ± 0.1	65
Cu [at%]	34.5 ± 0.3	33.5	36.8 ± 0.2	33.5	28.2 ± 0.2	27.5
Al [at%]	-	-	-	-	8.0 ± 0.2	7.5

Table 4.2: Average compositions of samples D, E and F.

Ribbon	G	G (nom.)	H	H (nom.)	I	I (nom.)
Zr [at%]	44.0 ± 0.3	45	65.9 ± 0.4	66.5	-	-
Cu [at%]	45.9 ± 0.3	45	34.1 ± 0.4	33.5	6.0 ± 0.2	6.0
Al [at%]	10.1 ± 0.3	10	-	-	-	-
Pd [at%]	-	-	-	-	79.0 ± 0.2	77.5
Si [at%]	-	-	-	-	15.1 ± 0.3	16.5

Table 4.3: Average compositions of samples G, H and I.

4.3 Thermal analysis at low heating rates using differential scanning calorimetry measurements

Prior to the calorimetric analysis of our samples, the differential scanning calorimeter 7 from Perkin Elmer was calibrated using pure elements of Indium and Zinc. The melting temperatures of Indium ($T_{M,In} = 429.75\ K$) and Zinc ($T_{M,Zn} = 692.68\ K$) have been used to calibrated the temperature axis since the cover the commonly used scanning range of 293 K to 823 K sufficiently.

In order to obtain information about the shift of the glass transition temperature and the crystallization temperature with a heating rate, we studied a range of 10 K/min up to 200 K/min. Fig. 4.2 shows the heat flow normalized with the heating rate of the glass forming composition $Zr_{65}Cu_{27.5}Al_{7.5}$ as a function of temperature. The normalized heat flow versus temperature shows a slightly increasing trend below the glass transition temperature. At the glass transition temperature, a pronounced increase in the normalized heat flow sets in before it levels off in a plateau region which is the supercooled liquid regime. At the crystallization temperature, a sudden decrease in the normalized heat flow occurs. This decrease is caused by the enthalpy release due to the crystallization.

The glass transition temperature as well as the crystallization temperature were determined by the intersection point of two tangents. The two tangents are linear fits, one of them fits the data points in a certain interval below the transition and the other one above the transition (red lines in Fig. 4.2). The glass transition temperature as well as the crystallization temperature increase with rising heating rate (green points in Fig. 4.2).

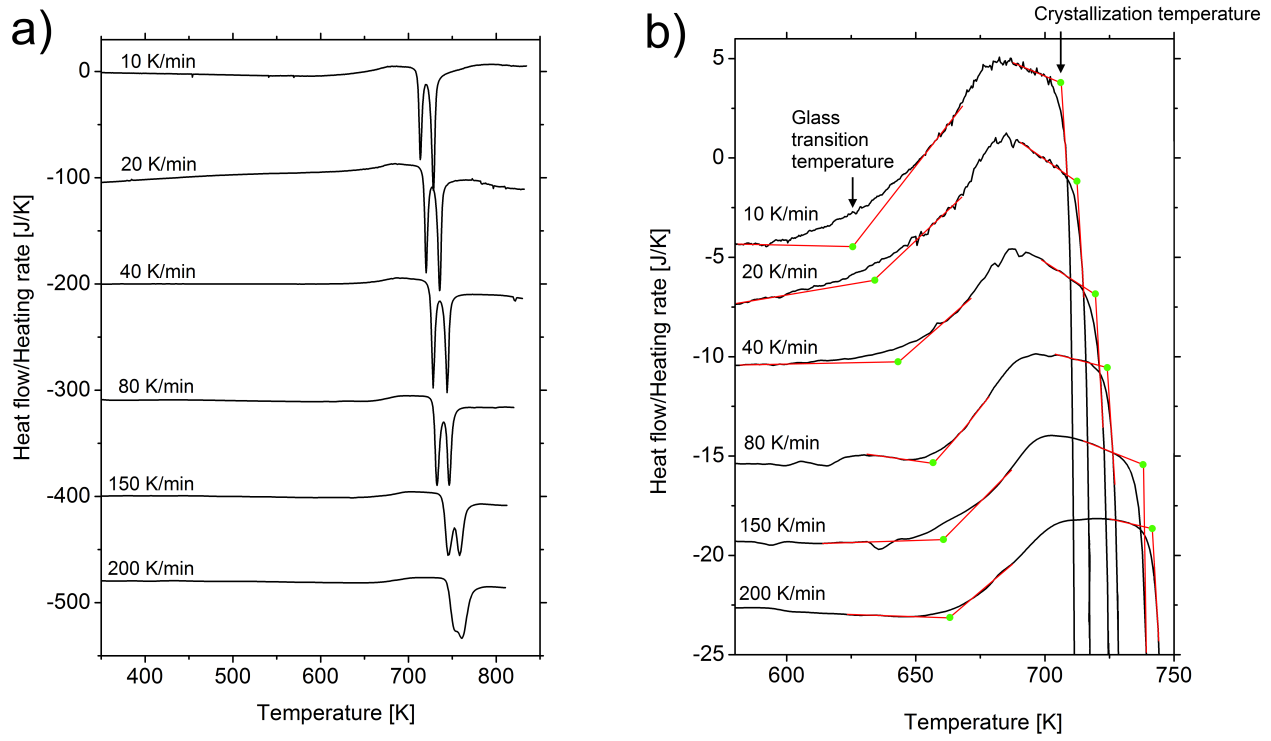

Figure 4.2: Calorimetry measurements of the metallic glass $Zr_{65}Cu_{27.5}Al_{7.5}$ for various heating rates. Panel a) shows the heating rate dependence of the two crystalline states. Panel b) shows the heating rate dependence of the glass transition temperature and the crystallization temperature of the first phase.

In Fig. 4.2a at 10 K/min it is obvious that the system $Zr_{65}Cu_{27.5}Al_{7.5}$ crystallizes in two steps (polymorphism). With increasing heating rate these two crystallization stages both move to higher temperatures. However, the first stage is more sensitive to the heating rate and thus moves faster two higher temperature than the second crystallization stage. This becomes evident when looking at the minima of the crystallization stages. At 200 K/min the two crystallization stages merge which is not an effect of the limited resolution. Please note, that the green dots in Fig. 4.2b for the crystallization temperature represent the onset of the first crystalline phase.

The shift of the glass transition temperature with heating rate of five compositions is illustrated in Fig. 4.3a. In order to fit these curves we used the Vogel-Fulcher-Tammann equation 2.1 and solved it to $T_G = T_{G,0} + A/\ln(\phi_c/\phi)$. Here, the parameter $T_{G,0}$ is interpreted as a lower limit of the glass transition temperature T_G, which means that this is the lowest possible glass transition temperature for a certain system which can be reached by, for instance, annealing, very slow quenching or by sputtering on substrates which are heated close to the glass transition temperature as it is done for ultrastable glasses(see below). ϕ_c is a critical rate at which the

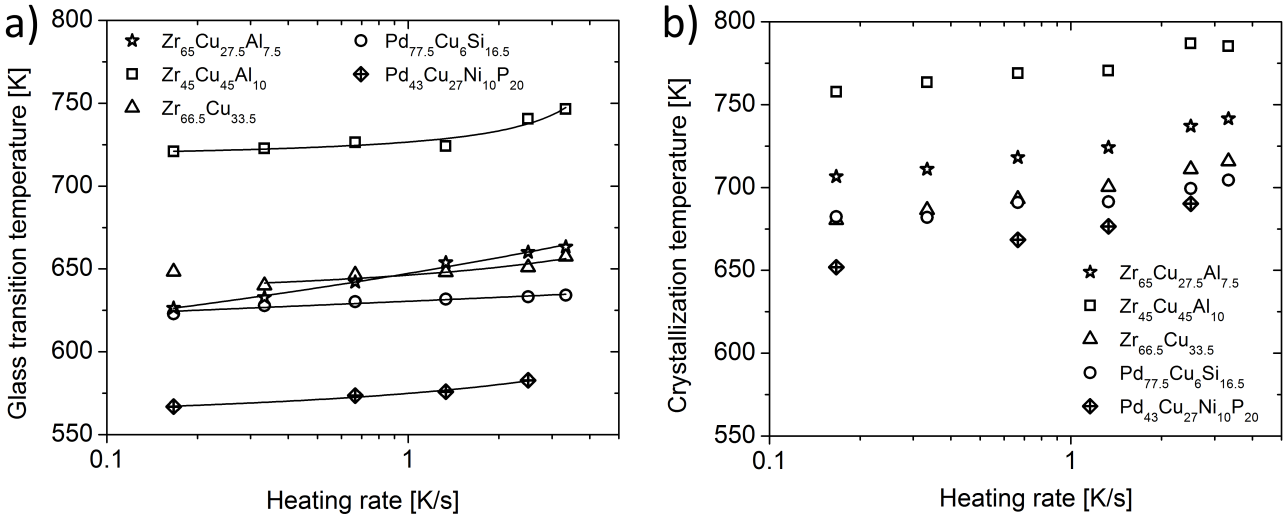

Figure 4.3: a) Glass transition temperature and b) crystallization temperature of five different compositions as a function of heating rate. The solid lines represent fits using the Vogel-Fulcher-Tammann equation.

equation for T_G has a pole and A is another material parameter.

The shift of the crystallization temperature as a function of heating rate is shown in Fig. 4.3b. In comparison with the shift of the glass transition temperature it is evident that the composition $Pd_{43}Cu_{27}Ni_{10}P_{20}$ exhibits the largest difference $\Delta T = T_x - T_G$ between the glass transition temperature and the crystallization temperature T_x. The difference is $\Delta T = 85$ K at a heating rate of 0.167 K/s and increases to $\Delta T = 108$ K at a rate of 2.5 K/s. The nominal composition $Zr_{45}Cu_{45}Al_{10}$ exhibits the smallest difference $\Delta T = 36$ K at a heating rate of 0.167 K/s and $\Delta T = 46$ K at 2.5 K/s.

4.4 Calorimetry measurements at high temperatures

We performed calorimetry measurements from room temperature to 1700 K in a Scanning Thermal Analyzer Netzsch STA 449 C with the compositions $Zr_{65}Cu_{27.5}Al_{7.5}$ and $Pd_{77.5}Cu_6Si_{16.5}$. Apart from the glass transition and the crystallization temperature, high temperature calorimetry measurements contain valuable information about the melting process and how close the alloy composition is located with respect to the eutectic point. We will later use the melting point as a reference value for the ultrafast heating measurements. The STA measurement of the composition $Zr_{65}Cu_{27.5}Al_{7.5}$ is shown in Fig. 4.4. The inset of Fig. 4.4 shows that the melting process exhibits three maxima. While the second and third maximum are merged, the first one can be clearly distinguished. The onset of the first maximum is at $T_{m,1} = 1179$ K and the onset of the second and third is at $T_{m,2} = 1198$ K.

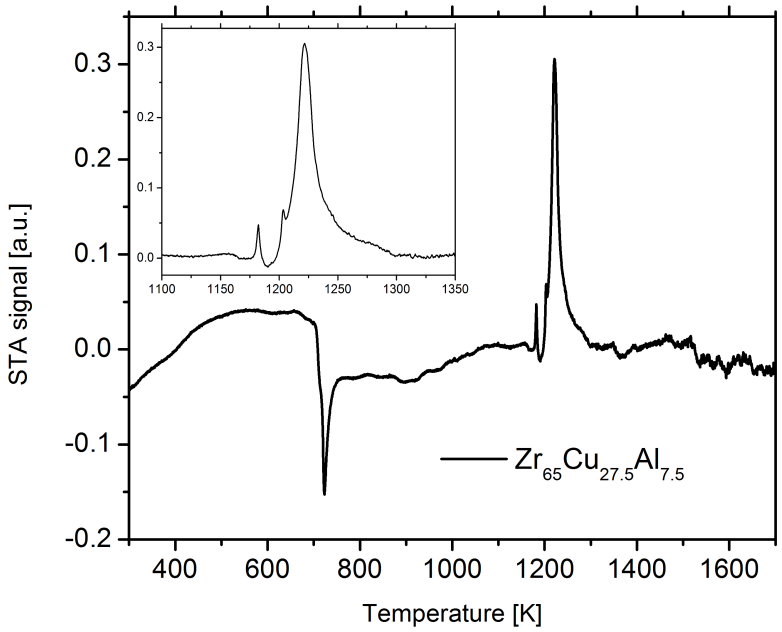

Figure 4.4: STA measurement of the composition $Zr_{65}Cu_{27.5}Al_{7.5}$ from room temperature to 1700 K. The inset enlarges the temperature region around the melting temperature.

The STA measurement of the composition $Pd_{77.5}Cu_6Si_{16.5}$ is shown in Fig. 4.5. Apparently,

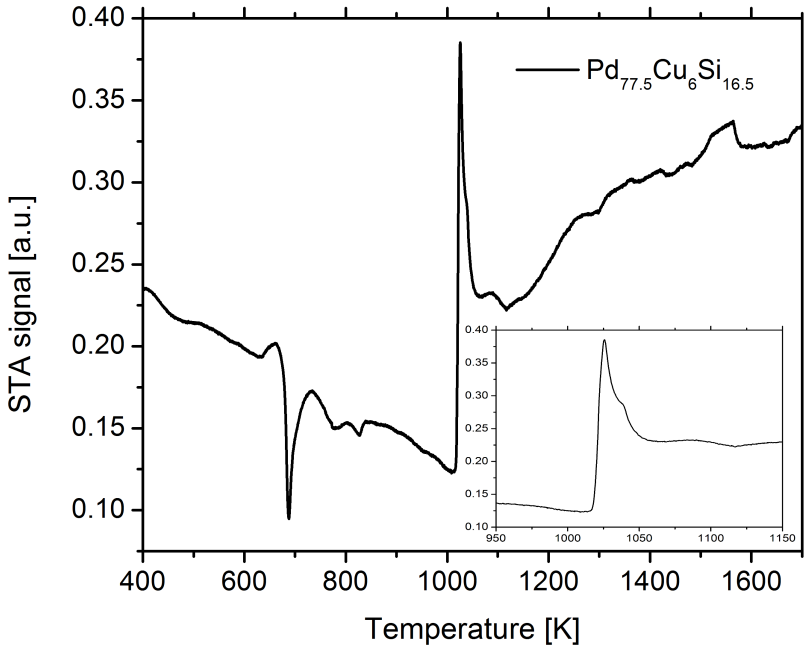

Figure 4.5: STA measurement of the composition $Pd_{77.5}Cu_6Si_{16.5}$ from room temperature to 1700 K. The inset enlarges the temperature region around the melting temperature.

the melting consists of two maxima which are merged and they are not clearly distinguishable anymore. The onset of the main maximum is $T_m = 1018$ K.

4.5 Specific heat capacity during ultrafast heating

The aforementioned differential scanning calorimetry method is a standard technique to determine the specific heat capacity of a sample. For metallic glasses, this technique allows specific heat capacity measurements until temperatures just above the glass transition temperature. Due to the low heating rates in the order of 10^0 K/s inevitably crystallization sets in above the glass transition temperature. The incipient crystallization process prevents the determination of the specific heat capacity at high temperatures in the supercooled liquid. The capacitor discharge technique reaches very high heating rates of the order of 10^6 K/s. With this high rates, the entire supercooled liquid from the glass transition to the melting temperature can be studied in specific heat capacity measurements. In this section, we present three different techniques to determine the specific heat capacity in the supercooled.

4.5.1 A first approach

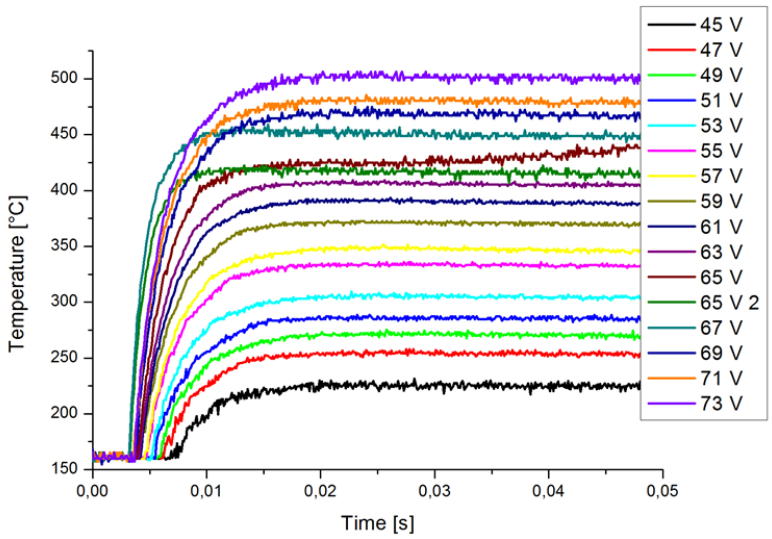

Figure 4.6: Several discharges of the capacitor with increasing voltages using always the same ribbon of the composition $Ni_{65}Cr_{20}Si_{15}$. We used always the same ribbon in order to keep the mass of the sample constant and vary only the voltage.

In these measurements, the charge voltage of the primary capacitor was increased in steps of 2 V (Fig. 4.6). We used one metallic glass sample of the composition $Ni_{65}Cr_{20}Si_{15}$ starting with the lowest voltage of 45 V. After the sample cooled down, the charge voltage was increased before the capacitor was discharged again. During the capacitor discharge, the temperature increases before it remains nearly constant in almost all of the measurements. A higher charge

voltage leads to the according increase in the final sample temperature. The measurement in which the capacitor is charged with 65 V (brown curve) shows an increase additional to the initial capacitor discharge. This increase is caused by crystallization. The capacitor has been charged again with 65 V (dark green curve, labeled with "65 V 2"). This measurement does not show this additional increase just as little as all the subsequent measurements at higher voltages.
The most simple determination of the specific heat consists of the evaluation of the overall temperature increase due to the main capacitor discharge. This section is called "A first approach" because this way of determining the specific heat assumes a constant specific heat capacity and emissivity in the entire range from room temperature to the final temperature. It also neglects all kinds of heat losses during heating, as for instance thermal radiation or heat losses to the connections, i.e. it assumes adiabatic conditions.
Therefore, the specific heat capacity in this case is calculated by the fraction of the energy supplied to the sample normalized by the mass and the consequent temperature increase ΔT

$$c_P = \frac{0.5 \cdot IU^2}{m\Delta T}. \tag{4.1}$$

The quantities U and I are the maximum voltage and the maximum current at the sample, respectively. This equation was applied to the measurements shown in Fig. 4.6. The nominator of Eq. 4.1 is plotted versus the denominator in Fig. 4.7a. The slope of this curve represents the specific heat capacity which is displayed in Fig. 4.7b. At low temperatures, the specific heat capacity remains constant at a value around 0.33 J/g·K. Between 614 K and 638 K the specific heat capacity rises to a value of 0.57 J/g·K, before it starts decaying between 638 K and 657 K. The increase in the apparent specific heat is related to the glass transition and the subsequent decrease to the crystallization. After the minimum the specific heat capacity even exhibits a maximum at 710 K before it levels off above 710 K at a specific heat value around 0.22 J/g·K.

4.5.2 Additional discharges

A more sophisticated method to determine the specific heat applies multi-step rapid capacitor discharges which is explained in section 3.4. The voltage of the main capacitor was varied in order to reach different temperatures around the glass transition temperature. Each 4 ms after the main capacitor was discharged, four additional small capacitors were discharged. In every measurement the small capacitors were previously charged with 20 V (see Fig. 4.8).

Here, we slightly modified equation 4.1 in the way that we integrated the power $I(t) \cdot U(t)$ over time in order to determine the energy put into the sample during the little discharges.

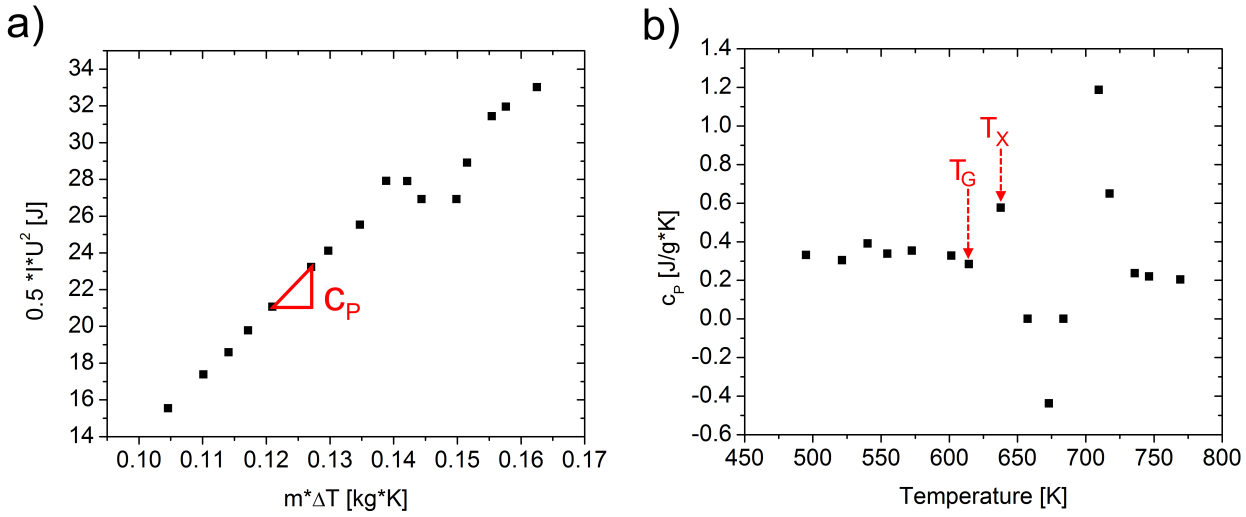

Figure 4.7: Panel a) shows the supplied heat from the capacitor versus consequent temperature increase. The slope of this curve, the specific heat capacity, versus temperature is displayed in panel b). The glass transition temperature occurs at some point between 614 K and 638 K and the crystallization starts between 638 K and 657 K. In both cases, we marked the lower limit of 614 K as the glass transition temperature and 638 K as the crystallization temperature.

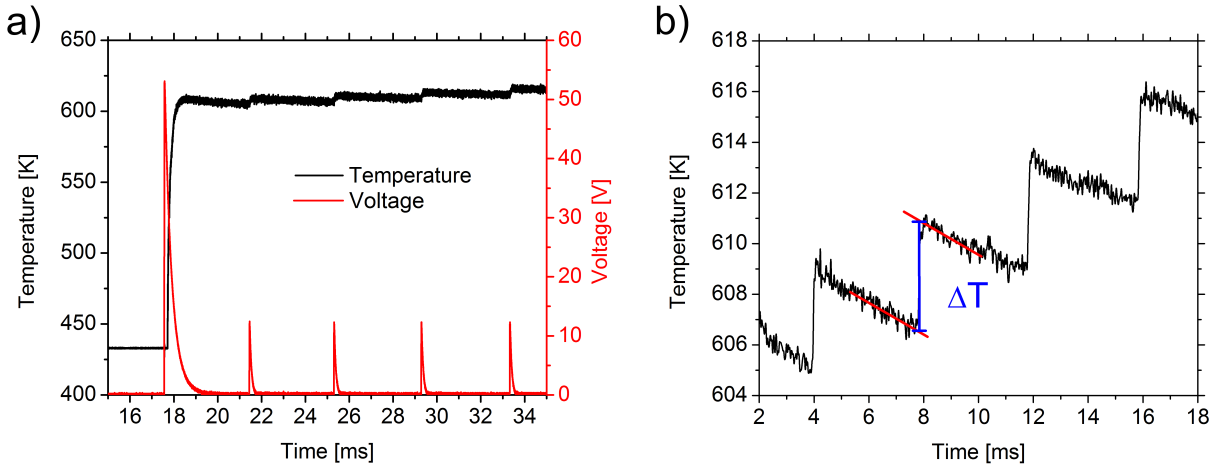

Figure 4.8: a) Exemplary temperature versus time curve with additional discharges each 4 ms. b) Temperature versus time curve zoomed in the high temperature regime after the initial capacitor discharge is over.

$$c_P(T) = \frac{\int I(t)U(t)\mathrm{d}t}{m\Delta T}. \tag{4.2}$$

In this equation, ΔT refers to the temperature increase due to the discharges of the little capacitors at high temperatures.

In the first measurement, we used only one sample of nominal composition $Pd_{77.5}Cu_6Si_{16.5}$. In this way, we avoid fluctuations in the specific heat due to errors in the determination of the correct mass which was actually heated up. The sample was heated up multiple times until it fused. We started with low voltages and increased the voltage by 2 V until we reached a temperature around 573 K from where we raised the voltage by 1 V.

Here, the specific heat capacity starts to increase at a value of about 0.275 J/g·K at 550 K

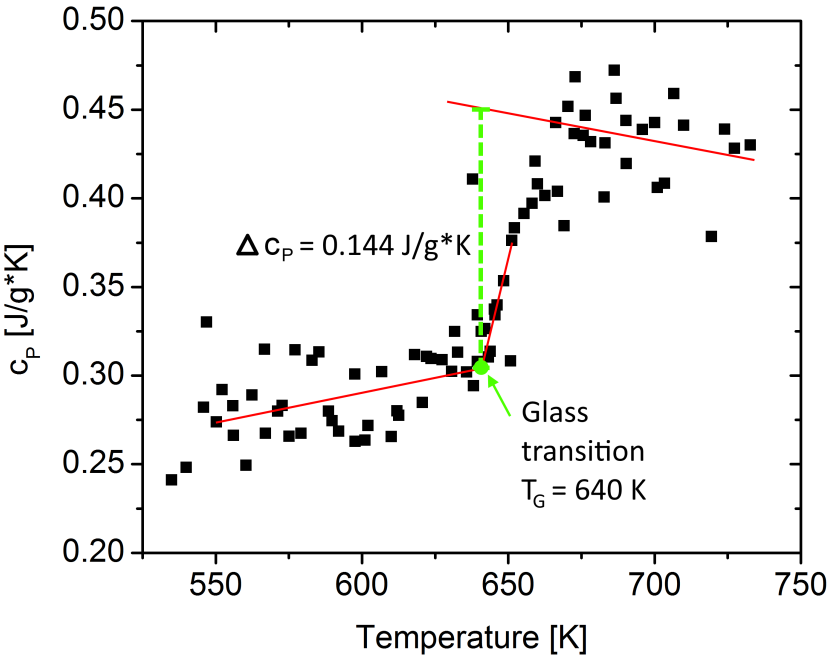

Figure 4.9: Specific heat capacity calculated by the temperature increase due to multiple discharges at high temperatures.

with an average linear slope of $3.4 \cdot 10^{-4}$ J/g·K^2 until 640 K where it starts to increase stronger. At 640 K we found the glass transition temperature by evaluating the intersection point of two tangents. In the supercooled liquid, the specific heat capacity decreases with an average slope of $2.79 \cdot 10^{-4}$ J/g · K^2. The jump between the specific heat in the glassy state and the specific heat in the supercooled liquid level is $\Delta c_P = 0.144$ J/g · K, evaluated at the glass transition temperature.

When we use only one sample for all the measurements, i.e. that we always reheated the same sample, the state of the sample is different for each measurement since the elevated temperatures during each measurement enhance aging process. This is an undesired effect and therefore one ideally would use a fresh sample for each measurement. Using a fresh sample for each measurement in turn has the disadvantage that the mass which is actually heated up

changes in every measurement. This parameter is difficult to determine and leads to errors in the determination in the specific heat capacity.

However, for the specific measurements shown in Fig. 4.10 we always used a fresh sample

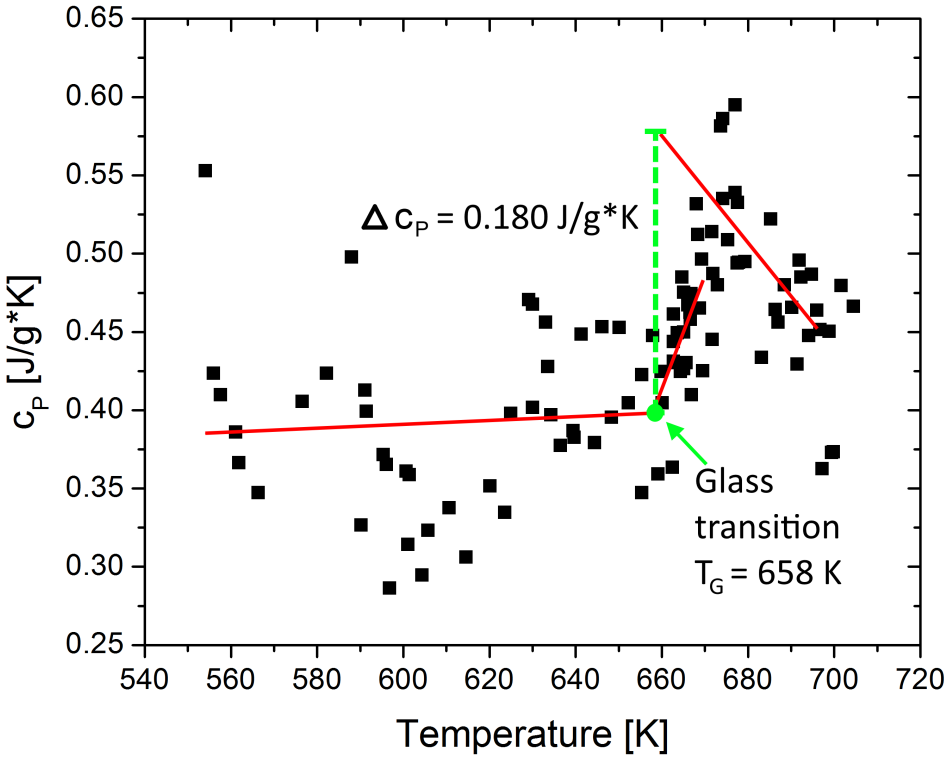

Figure 4.10: Specific heat capacity calculated by the temperature increase due to multiple discharges at high temperatures.

for each measurement. The data scatters more than in the case of a single sample but the characteristic features like the glass transition are still noticeable. At low temperatures, the specific heat increases with a slope of $1.21 \cdot 10^{-4}$ J/g $\cdot$ K^2 before the glass transition occurs at $T_G = 658$ K. The jump in the specific heat capacity between the glassy and the supercooled liquid state evaluated at the glass transition temperature is $\Delta c_P = 0.180$ J/g $\cdot$ K.

4.5.3 Specific heat measurements during the primary capacitor discharge

During the discharge of the main capacitor we recorded the voltage and the current with a high temporal resolution. Despite the fact, that the specific heat capacity is quantity which is commonly measured in equilibrium, we determined the specific heat during the primary capacitor discharge by dividing the temperature versus time curve as well as the power versus

time curve into small time intervals. The length of the time intervals we call "binning". For the specific heat measurements, the emissivity is also assumed to be constant since we are not able to measure it on very short timescales at the high temperatures in the supercooled liquid. To our knowledge, there is no literature data available. For the calculation of the specific heat c_P during heating, we evaluated the amount of electrical power $\Delta U \Delta I$ in the sample and the consequent temperature increase ΔT in time intervals of $\Delta t = 0.05$ ms. In order to reduce the error due to noise, we used a linear fit of both quantities in the aforementioned time interval. Therefore, we calculate the specific heat at a time $t = (t_1 + t_2)/2$ by:

$$c_P(T(t)) = \frac{\Delta Q}{m\Delta T} = \frac{\int_{t_1}^{t_2} I(t) \cdot U(t) \mathrm{d}t}{m\Delta T} = \frac{(I(t_1)U(t_1) + I(t_2)U(t_2))}{2m\Delta T} \cdot \Delta t \qquad (4.3)$$

with $\Delta T = T(t_2) - T(t_1)$. This time interval Δt has to be small in order to resolve rapid changes in the specific heat but also not too small in order not to over emphasize the noise.

The specific heat capacity determined during the primary capacitor discharge exhibits an

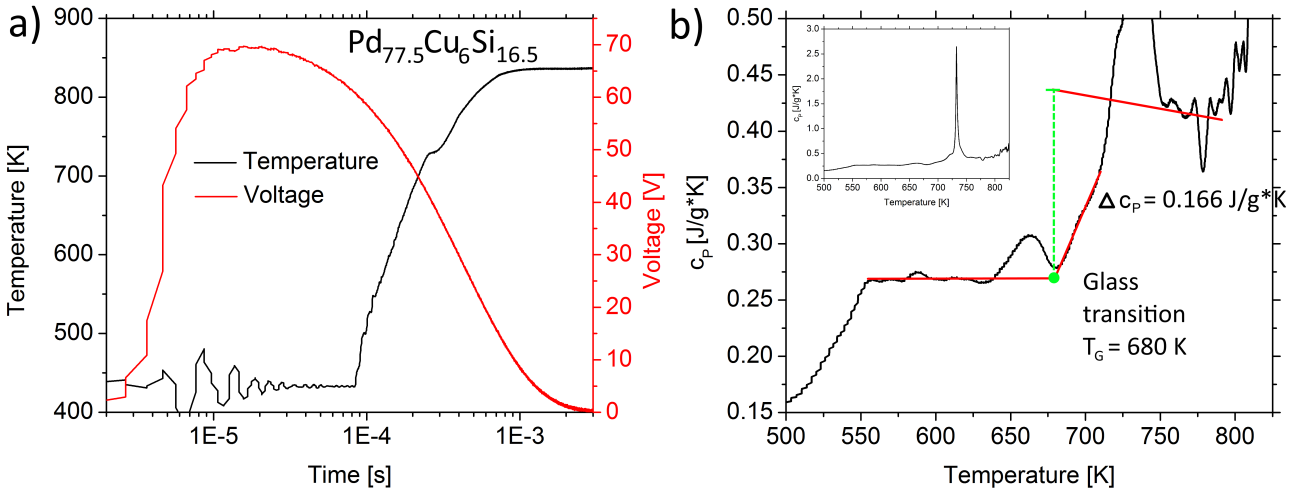

Figure 4.11: a) Temperature and voltage versus time curves of a $Pd_{77.5}Cu_6Si_{16.5}$ sample in the time regime of the first capacitor discharge. The specific heat capacity was calculated in the range until the primary capacitor discharge is over. b) Result for the specific heat capacity during the primary capacitor discharge of the measurement shown in panel a). The inset shows entire overshoot which occurs at the glass transition temperature.

increase of about 0.1 J/g·K from 500 K to about 550 K which is followed by a nearly constant regime (see Fig. 4.11). The glass transition is clearly visible at 680 K where the specific heat capacity shows a pronounced overshoot before it levels off in the supercooled liquid level. The difference in the specific heat capacity between the glassy state and the supercooled liquid regime is about 0.166 J/g·K. As mentioned above, we cannot determine the specific heat capacity as soon as the capacitor is entirely discharged. At this time there is usually a plateau

in the temperature versus time curve in the absence of endothermal or exothermal processes.

The specific heat capacity and the corresponding temperature versus time curves of a range

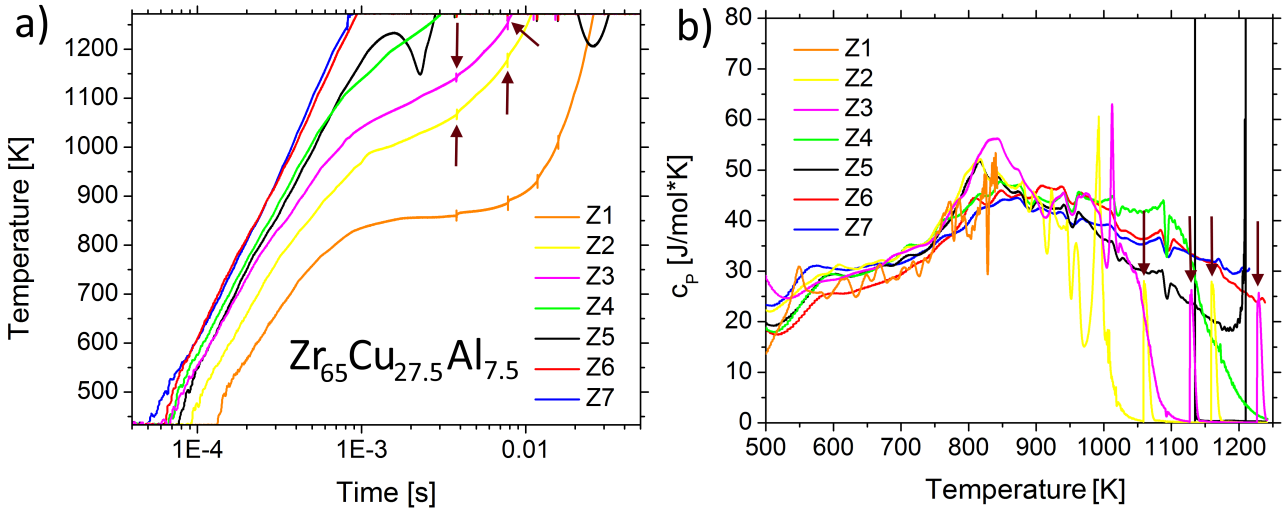

Figure 4.12: a) Several temperature versus time curves of $Zr_{65}Cu_{27.5}Al_{7.5}$ in a broad temperature regime. b) Specific heat capacity of the measurements shown in panel a) mainly determined during the primary capacitor discharge. The arrows indicate the moments where additional discharges take place.

of $Zr_{65}Cu_{27.5}Al_{7.5}$ samples are shown in Fig. 4.12. The specific heat capacity slightly increases until the glass transition temperature T_G where it increases stronger. After reaching the supercooled level, the specific heat capacity decreases again. In the measurement of the samples Z2, Z3 and Z4 the specific heat capacity in the supercooled liquid region goes to zero because the capacitor is completely discharged and thus there is no heat supplied anymore and the specific heat capacity cannot be determined anymore with some exceptions. The arrows in the temperature versus time curves as well as in the specific heat capacity curves of the samples Z3 and Z4 indicate additional discharge from the small capacitors. In the small moment of the capacitor discharges pf the small capacitors the specific heat capacity can again be reliably determined. Among these measurements, the absolute values of the specific heat, here in the units J/mol·K, are independent on the heating rate and well reproducible. It is noticeable that the values of the glass transition temperatures T_G and the differences between the specific heat in the solid glass state and the specific heat in the supercooled liquid state Δc_P are shown in table 4.4. With increasing heating rate from sample Z1 to sample Z7 the glass transition temperature rises while Δc_P remains almost unchanged.

	Z1	Z2	Z3	Z4	Z5	Z6	Z7	∅
T_G [K]	737	727	747	759	743	756	756	-
Δc_P [J/mol·K]	-	18.5	16.6	10.0	15.1	12.2	11.2	13.9 ± 1.2

Table 4.4: Glass transition temperature T_G and specific heat difference Δc_P

4.6 Glass transition temperature during intermediate heating

In the heating process with the programmable power supply we reach heating rates from 10^0 up to 10^5 K/s. Therefore, we call the heating with the power supply "intermediate heating". During the heating process we cannot assume adiabatic conditions since heat losses due to heat transfer to the holders and due to radiation cannot be neglected anymore. For an accurate determination of the specific heat capacity with this method, one would need to quantify these losses and take them into account. However, in this section our intention is not to determine the correct absolute values but the glass transition temperature, i.e. the fraction of heat transformed in the sample and subsequent temperature increase needs to be sensitive enough in order to resolve the relative increase of the specific heat at the glass transition.

For the determination of the fraction of heat transformed in the sample and subsequent temperature increase we varied the binning which is the time interval during which we evaluated the aforementioned fraction in accordance to the amount of points recorded. The evaluated temperature versus logarithm of time graphs of a ribbon with the nominal composition $Zr_{65}Cu_{27.5}Al_{7.5}$ is shown in Fig. 4.13. For comparison, we also added the temperature versus time curves of the lowest and the highest heating rate of the DSC measurements and a temperature graph from an ultrafast heating measurement using the capacitor discharge method all three in black dashed lines. It is visible that the intermediate heating technique covers the heating rate regime between the DSC and the ultrafast heating measurements well. The available range of heating rates of the intermediate heating technique even overlaps partially with the DSC heating rate regime. In fact, we were able to heat even with a lower heating rate than the lowest displayed heating curve with a rate of 2.5 K/s (grey curve in Fig. 4.13). Unfortunately, we could not identify the glass transition anymore.

In the measurements in this section, we were not able to calculate the specific heat capacity because of the aforementioned heat losses. Therefore, we evaluated the fraction of supplied heat and the subsequent temperature increase $\Delta Q/m\Delta T$ (see Fig. 4.14). The curves have been normalized and shifted vertically from the highest to lowest heating rate for clarity. We identified the glass transition temperature as the onset of the increase in $\Delta Q/m\Delta T$ which we determined by the intersection point of two tangents (marked with black triangles). The heat-

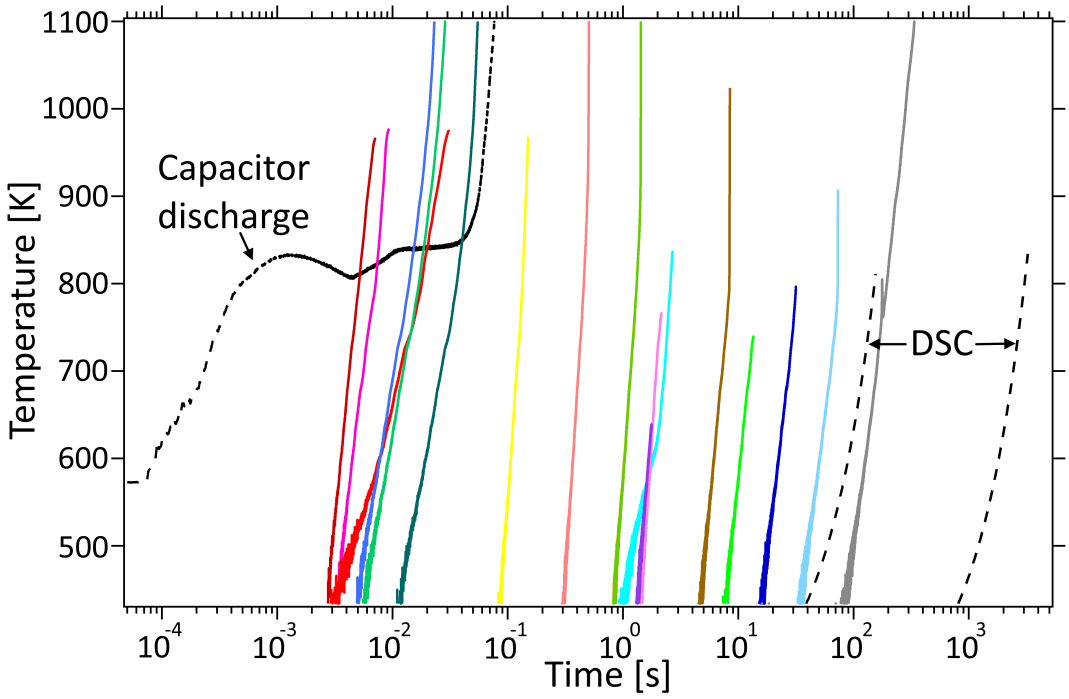

Figure 4.13: The temperature versus time curves during intermediate heating are displayed in color. The three black dashed lines correspond to two DSC measurements of the lowest and the highest possible heating rate and one ultrafast heating measurement using the capacitor discharge technique.

ing rate Φ of each curve in Fig. 4.14 was calculated by the average heating rate from the lower detection limit of the pyrometer of 433 K up to the glass transition temperature from Fig. 4.13. The glass transition temperature is plotted separately as a function of heating in Fig. 4.15. It is noticeable that the glass transition temperature is increasing monotonically from 644 K up to 727 K within a change of almost five orders of magnitude in the heating rate. The change in glass transition temperature with heating rate in context with the results from DSC and ultrafast heating measurements is discussed in section 5.4.

4.7 Heat losses during ultrafast heating

During the ultrafast heating measurement there are two main reasons for heat losses, heat transfer to the holders and the environment and thermal radiation. In comparison, it is noticeable that the timescale for heat losses are much longer than the timescales of heat supply from the capacitor discharge technique or from the intermediate heating on the fastest rates. Fig. 4.16a shows the temperature versus the logarithm of time plot during heating and cooling of a $Zr_{65}Cu_{27.5}Al_{7.5}$ sample which was heated up twice with the power supply on a fast rate

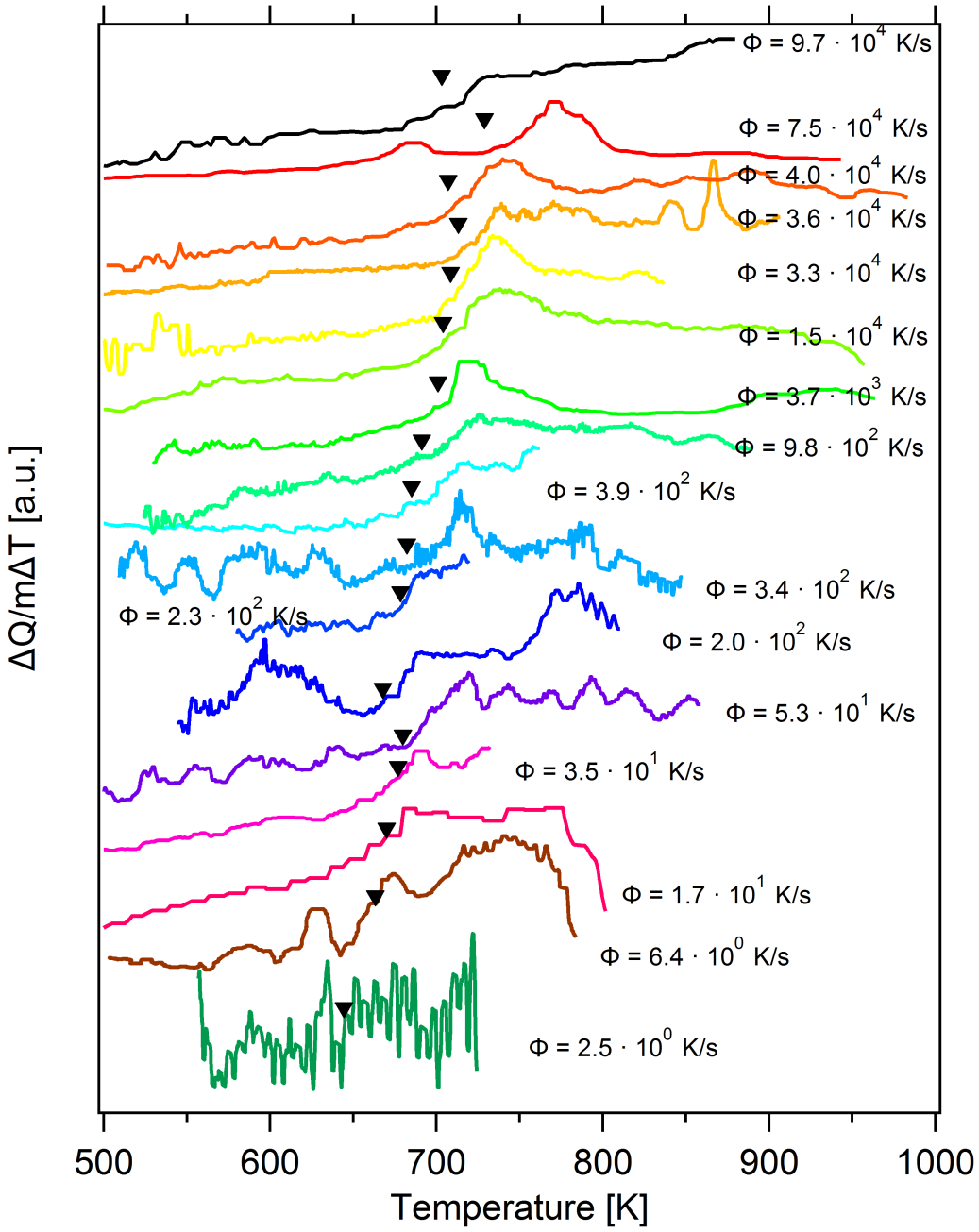

Figure 4.14: Fraction of supplied heat and subsequent temperature increase versus temperature. The black triangles indicate the onset of the glass transition.

of $1.47 \cdot 10^4$ K/s. In the first heating run, the sample was heated above the glass transition temperature while in the second run it was heated above the crystallization temperature. In the plot of the cooling rate versus temperature (Fig. 4.16b) there is a minimum of $dT/dt = -220$ K/s in the amorphous curve and a minimum of $dT/dt = -716$ K/s in the crystalline curve when ignoring the values of the noise at low temperatures. This corresponds to a characteristic

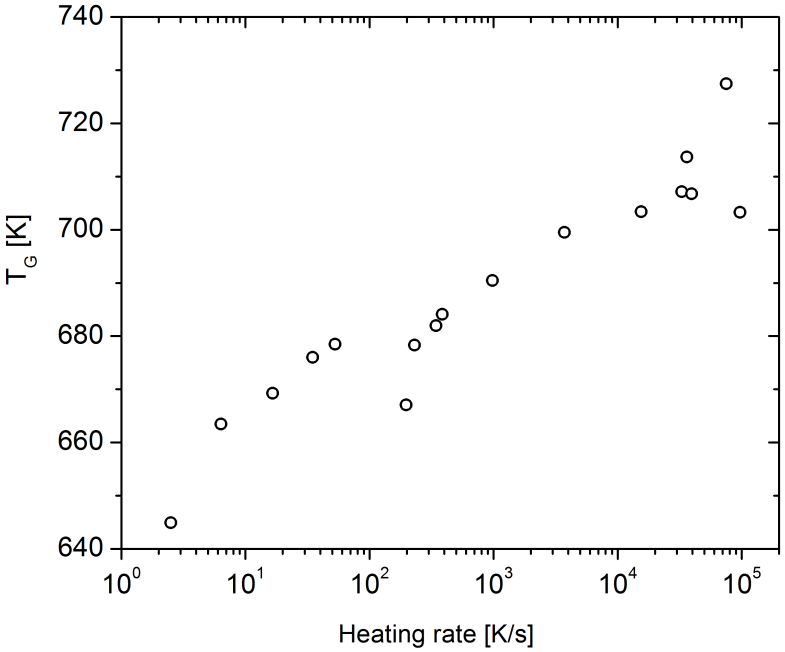

Figure 4.15: Shift of the glass transition temperature of $Zr_{65}Cu_{27.5}Al_{7.5}$ with changes in the heating rate.

power of $P = dT/dt \cdot c_P/A = 195$ J/s· mol·mm^2 for the crystalline state and a power of $P = 60$ J/s· mol·mm^2 for the amorphous state, with a surface area A = 147 mm^2 and specific heat capacity of $c_P = 40$ J/mol·K.

For instance, for the sample used in the measurement in Fig. 4.16 it means that the temperature decreases 0.036 K at most for the sample in the crystalline state and 0.011 K at most for the sample in the amorphous state. These two temperature decreases correspond to a time interval of $5 \cdot 10^{-5}$ s which we used to evaluate the specific heat capacity during ultrafast heating. The small capacitors which are discharged additionally to the primary capacitor at high temperatures are discharged with a characteristic time constant of $7.8 \cdot 10^{-5}$ s. Since we evaluate only amorphous samples well below 800 K with the additional discharge technique, we can expect that the temperature decrease during the discharges is not more than 0.017 K which is less than 0.5 % of the temperature increase which is between 3-7 K.

4.8 Crystallization during ultrafast heating

A Time-Temperature-Transformation (TTT) diagram reflects the time when the crystallization at different temperatures sets in. We performed a range of rapid heating measurements exploit-

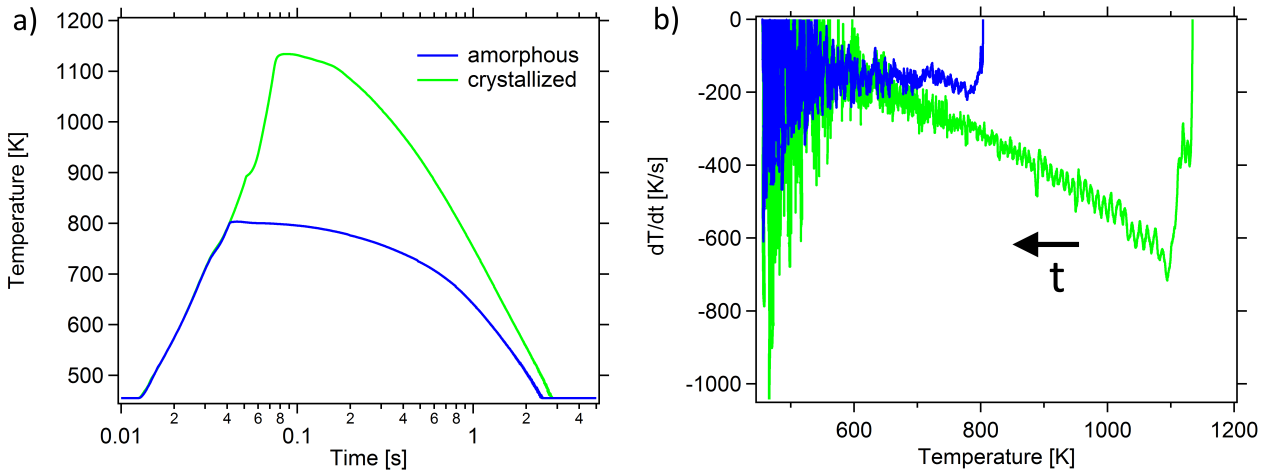

Figure 4.16: Cooling and heating curve during an intermediate heating experiment. a) Temperature versus time curve where in the first run a sample was only heated above the glass transition temperature (blue curve) and in the second run it was heated above the crystallization temperature.(green curve) b) Cooling rate versus temperature of the sample in the amorphous (blue) and in the crystalline state (green).

ing almost the entire crystallization nose for several glass forming compositions. We used a fresh sample for every measurement. As it was pointed out in section 3.10, the temperature which is reached by the capacitor discharge is proportional to the heating rate and both quantities depend on the charge voltage of the primary capacitor. Therefore, in the upcoming description and discussion we will only mention either the heating rate or the final temperature which is reached by means of the capacitor discharge, however, the other quantity is always implied.

The crystallization behavior of $Ni_{65}Cr_{20}Si_{15}$ is shown in Fig. 4.17. For the three relatively low heating rates we do not observe any additional temperature increase after the initial increase due to capacitor discharge, i.e. the three samples do not crystallize during the measurement. At higher heating rates there is an additional temperature increase noticeable, which becomes more prominent at higher heating rates. This means that the temperature increase due to crystallization is higher and takes place on a faster time scale. Even in the measurement with the highest heating rate, we still detect a crystallization process which is indicated by a noticeable deviation from the trend of temperature versus time curve due to the capacitor discharge. In the measurement with the highest heating rate J14 (grey curve) the sample breaks during the measurement. The temperature of sample J14 is only displayed until the point where the sample broke in Fig. 4.17 since the temperature measurement is not considered it to be reliable after breaking.

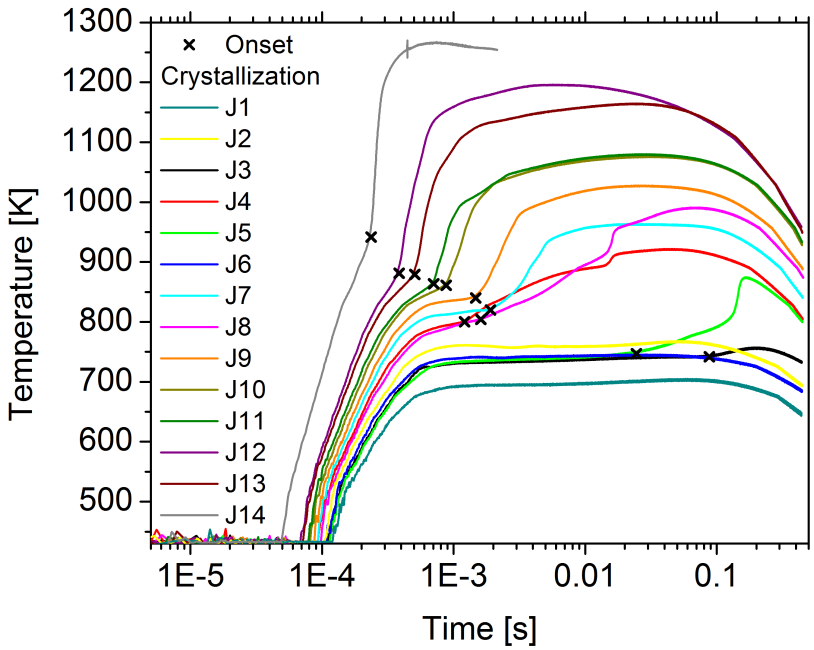

Figure 4.17: Various rapid heating experiments of the metallic glass $Ni_{65}Cr_{20}Si_{15}$. The crosses indicate the onset of crystallization in each measurement.

4.9 Analysis of crystalline phases at different temperatures in the TTT diagram

In this section, we present the results which we obtained during high energy X-ray measurements with an enhanced temporal resolution at the synchrotron beamline P07. The X-ray diffraction images were taken before and during the crystallization process at different temperatures. We investigated three different compositions $Zr_{65}Cu_{27.5}Al_{7.5}$, $Zr_{45}Cu_{45}Al_{10}$ and $Zr_{66.5}Cu_{33.5}$. In total, we analyzed 91 samples during rapid heating at the synchrotron beamline and in each measurement we recorded 100 detector images with 13 sections due to the chopper each. So there is total number of 118300 diffraction patterns which we analyzed. This amount of diffraction patterns cannot all be shown here and therefore we restricted the results of this section to a representative selection.

Fig. 4.19 shows the temperature versus time curve during rapid heating measurements and the crystallization process at various crystallization temperatures of the metallic glass $Zr_{65}Cu_{27.5}Al_{7.5}$. Apparently, the crystallization event in the measurement with the highest heating rate (green curve) sets in at a later time in comparison to the measurement with a slightly lower heating rate (blue curve).

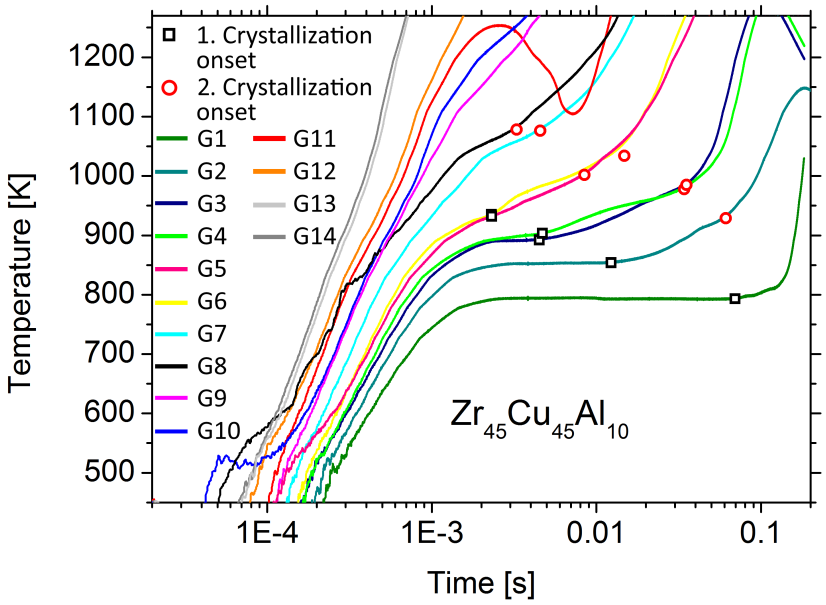

Figure 4.18: Various rapid heating experiments of the metallic glass $Zr_{45}Cu_{45}Al_{10}$. Here, a two-step crystallization takes place. The squares indicate the onset of the first crystallization process while the rings mark the beginning of the second one. For very high heating rates the onsets of crystallization are not unambiguously distinguishable from the heating due to the primary capacitor discharge.

For the analysis of the X-ray diffraction measurement, we recorded a series of 100 X-ray frames while the chopper was running. We integrated the intensity of each section of the chopper separately for each recorded X-ray frame. Each chopper section was assigned to a 5 ms time window in the correct temporal order. With this assignment, the integrated intensity was plotted in a grey scale versus the time and the scattering vector q. For this plot, the intensity is normalized by the maximum intensity of each section.

The integrated intensities of the sample with the highest heating rate, sample A9, the sample with the lowest heating rate, sample A1, and two samples with medium heating rates, samples A4 and A8, are plotted in Fig. 4.20. In the case of sample A1, it is visible that capacitor discharge starts 0.12 s after the start of the measurement which is indicated by the rise of the temperature curve. The integrated intensity of sample A1 exhibits three broad diffraction maxima at $q_1 = 2.8$ Å^{-1}, $q_2 = 4.4$ Å^{-1} and $q_3 = 4.9$ Å^{-1} until 0.15 s after the start of the measurement. At this time, the transformation into sharp peaks is accommodated by the second increase in the temperature curve. We call this crystalline phase "intermittent phase". 65 ms later, the sharp peaks broaden and a "diffuse regime" is established. The diffuse regime remains for about 0.23 s. Besides the broad maxima which are in the same q-range as the original broad

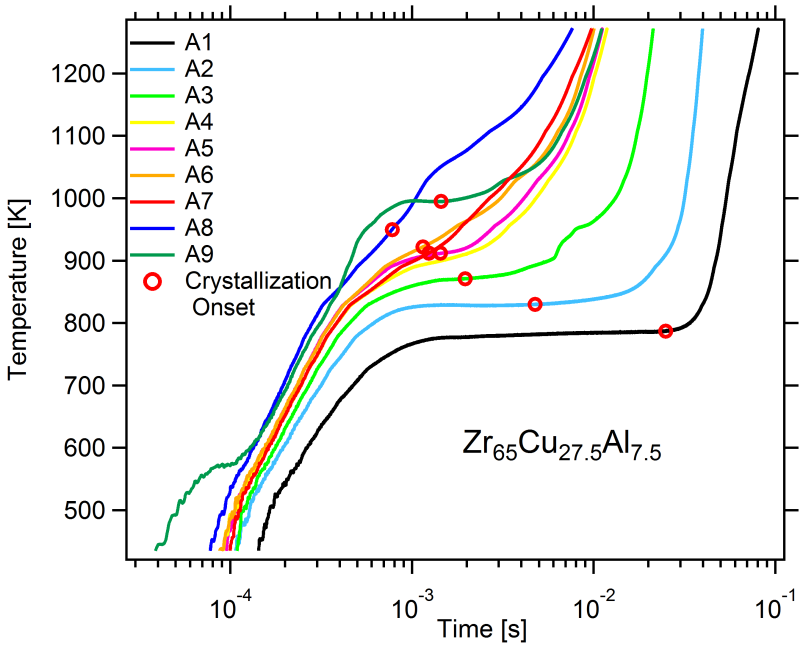

Figure 4.19: Various rapid heating experiments of the metallic glass $Zr_{65}Cu_{27.5}Al_{7.5}$. The circles mark the onset of the crystallization process.

maxima at the beginning of the measurement, there are also several sharp peaks visible. These crystalline peaks are at different positions than the peaks of the intermittent crystalline phase. Afterwards, there are only sharp peaks visible until the end of the measurement. Therefore we call this state "final phase". In the measurements with higher heating rates the same states occur as in the measurement A1. However the "lifetime" of the intermittent phase changes. The intermittent phase lasts 20 ms, 25 ms and 25 ms in the cases of samples A4, A8 and A9, respectively.

In order to identify the crystalline phases which occur in the temporal evolution of the system after the discharge started, we calculated the expected scattering angle 2θ from the scattering vector q with a wavelength of $\lambda = 0.1574$ nm (close to the nominal Cu K_α radiation) for our scattering experiments [82, 83, 71]. For this purpose, we applied the formula $2\theta = 2 \cdot \arcsin(\lambda\, q/4\pi)$. A comparison of the crystalline peaks of the intermittent phase with literature data from Lin et al. shows that the peak positions agree vastly with the positions of the tetragonal intermetallic Zr_2(Cu,Al) phase (see Fig. 4.21)[82]. This observation is also confirmed by [71]. For comparison the data of the Zr_2Cu and ZrO_2 phase have been digitized using the software "plot digitizer" from the work of Lin et al. and Toraya et al., respectively. The positions of two of the peaks which have been marked as Zr_2Al (at 35.1° and at 43.3°) match also with the positions of a quasicrystalline icosahedral phase. Apart from that, the peaks at 35.1° and at 38.7° overlap with peaks from the ZrO_2 phase. At this point, we cannot unambiguously decide

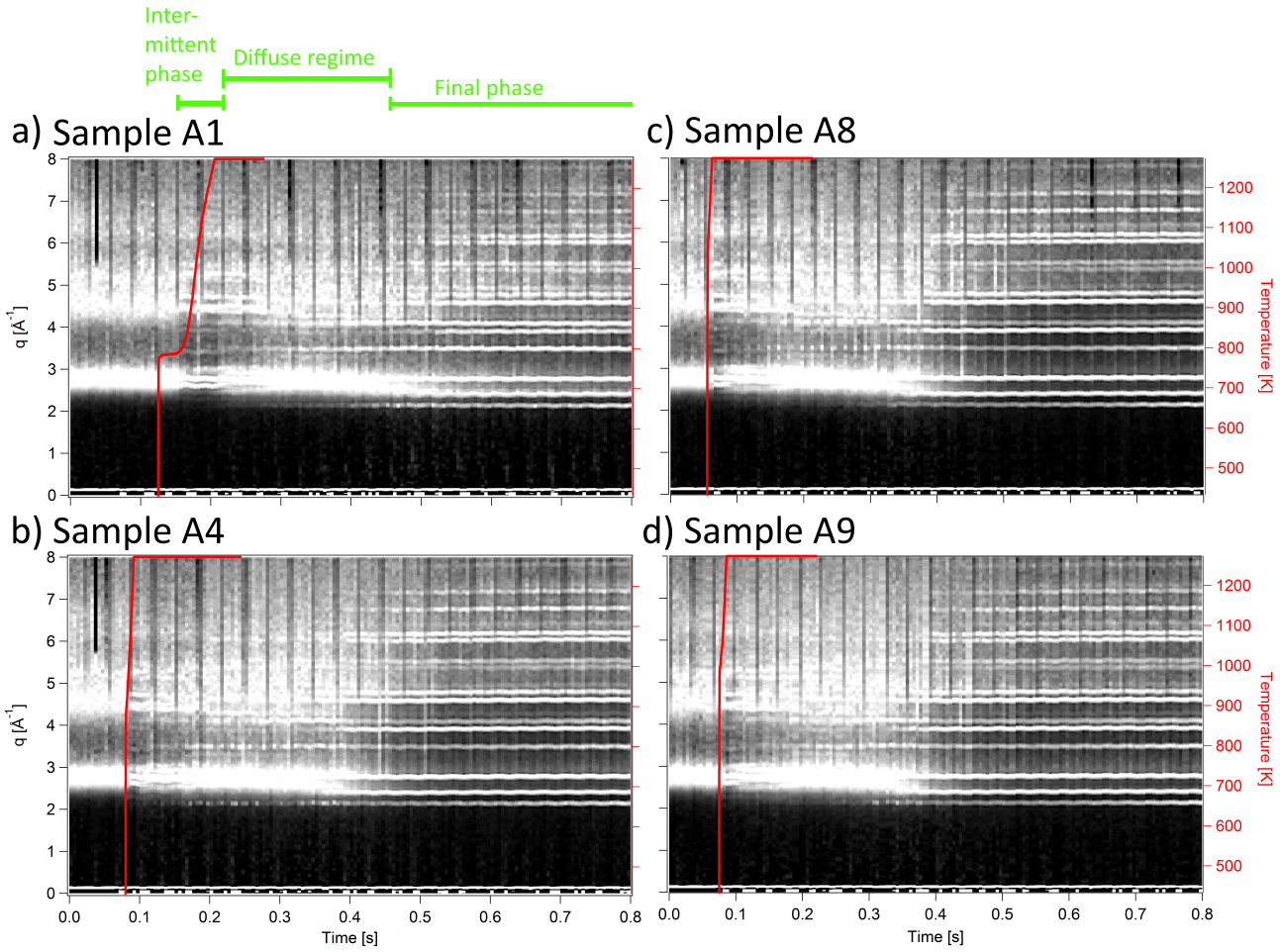

Figure 4.20: Integrated intensity of the samples A1, A4, A8 and A9 in a grey scale versus time and scattering vector q. The corresponding temperature curve is plotted on the same time axis in red.

to which phase these peaks can be assigned.

We also calculated the expected positions of several crystalline phases which are marked with crosses in the bottom of Fig. 4.21 using the equation

$$2\theta = 2 \cdot \arcsin\left(0.5 \cdot 0.1574 \sqrt{\left(\frac{h}{a}\right)^2 + \left(\frac{k}{b}\right)^2 + \left(\frac{l}{c}\right)^2}\right), \tag{4.4}$$

where h, k and l are the Miller indices and the parameters a, b and c represent the size of the respective unit cell. The final phase consists of the ZrO_2 phase and to the Cu_2O phase. There is also one dominant peak in the spectrum at 39.5° which matches with a position of the cubic ZrO_2 phase.

Fig. 4.22 shows the temperature versus time curves of another ribbon B consisting also of the

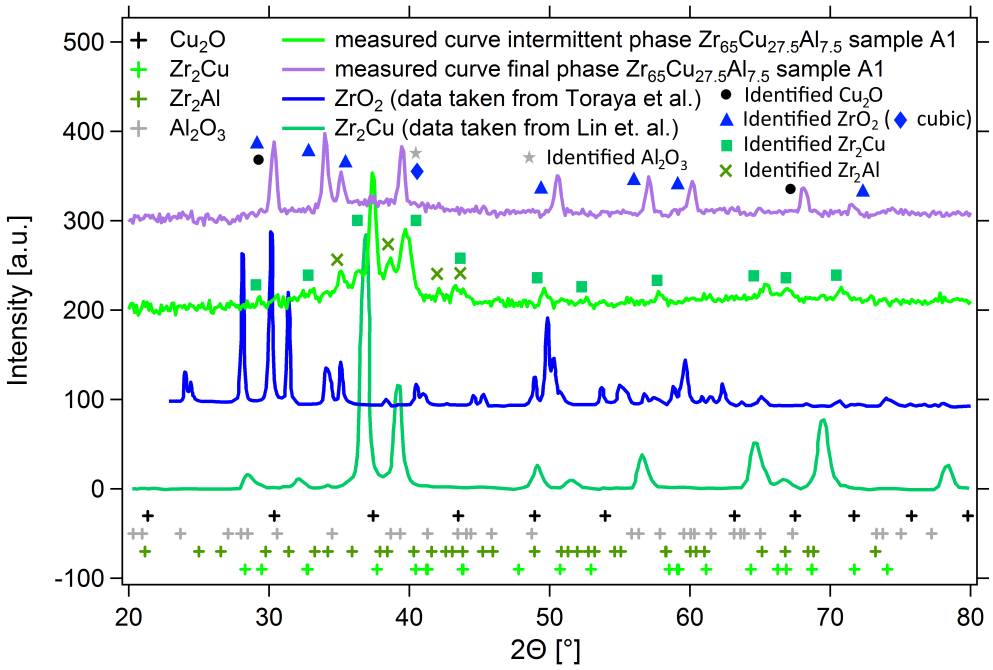

Figure 4.21: Assignment of crystalline phases to the intermittent and the final phase of $Zr_{65}Cu_{27.5}Al_{7.5}$ in sample A1.

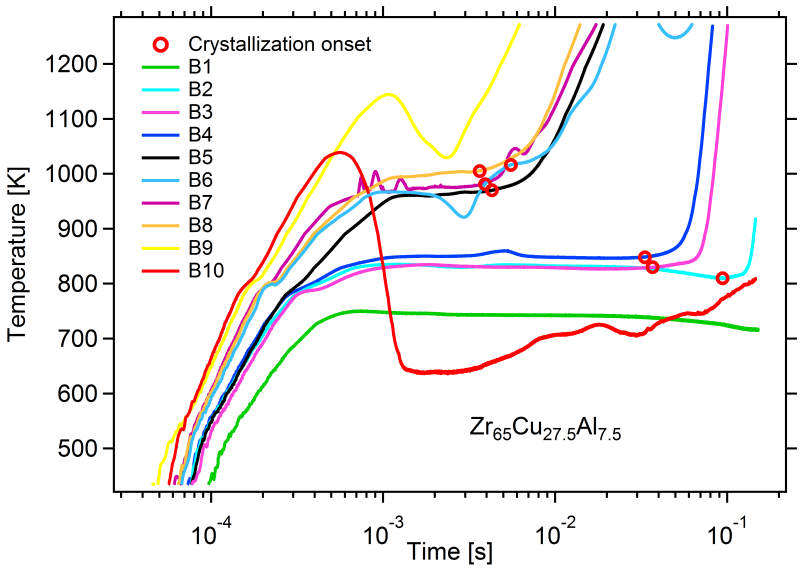

Figure 4.22: Various rapid heating experiments of the metallic glass $Zr_{65}Cu_{27.5}Al_{7.5}$. The circles mark the onset of the crystallization process.

composition $Zr_{65}Cu_{27.5}Al_{7.5}$. At the highest crystallization temperature of 1005 K, the crystallization sets in after 3.6 $\cdot 10^{-3}$ s. Apparently, a crystallization process takes place in the case of sample B9 (yellow curve) in Fig. 4.22 at a higher temperature than 1000 K but due to the distortion in the temperature curve, a determination of the crystallization temperature would

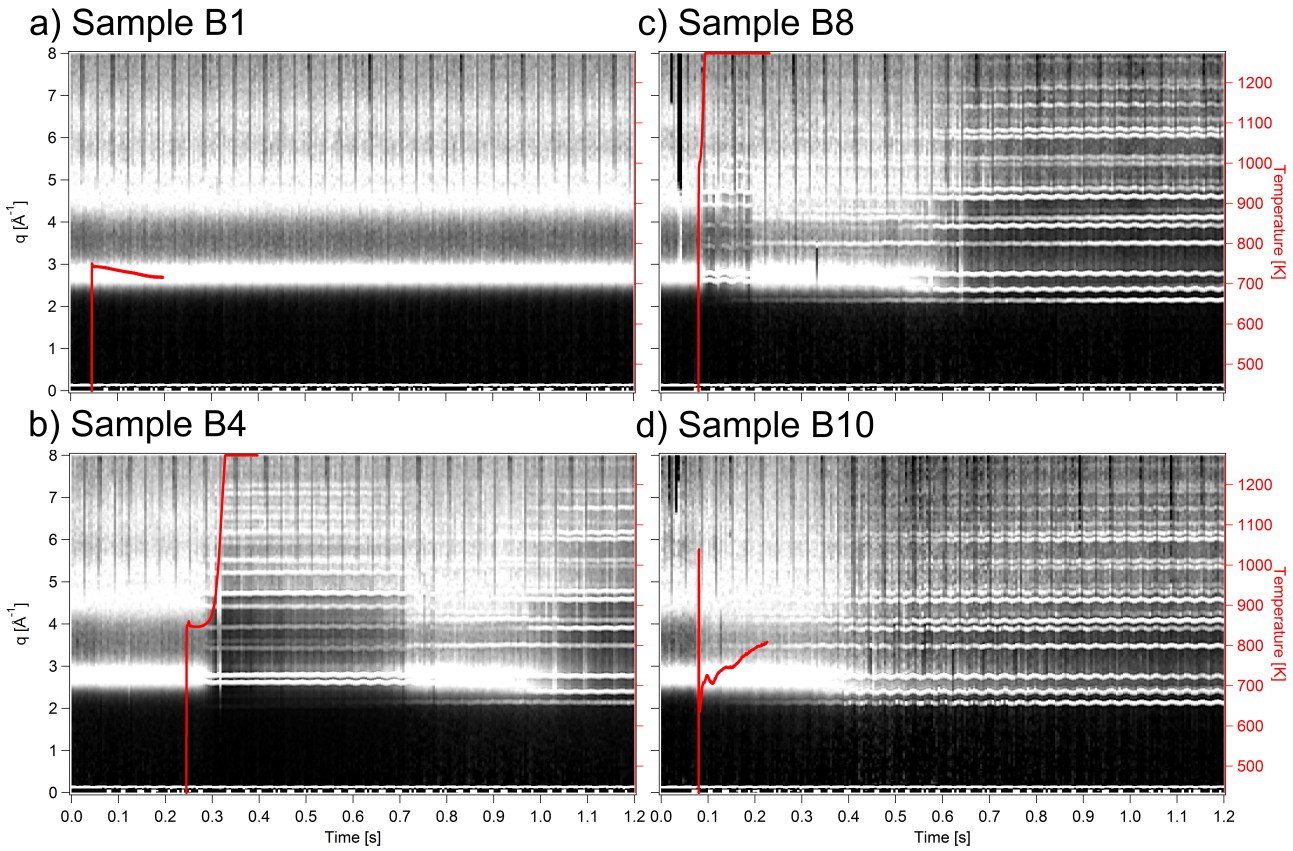

Figure 4.23: Temporal evolution of X-ray diffraction patterns of four different measurements of ribbon B.

be subject to large errors. At the lowest crystallization temperature of 810 K in the case of sample B2, the crystallization process sets in $9.4 \cdot 10^{-2}$ s after the discharge started.
Some curves show unusual distortions in the temperature behavior which are not reproducible. For instance sample B6 exhibits a minimum in the temperature curve at about $3 \cdot 10^{-3}$ s as well as sample B9 shows a pronounced minimum at $2 \cdot 10^{-3}$ s. Particularly, sample B10 exhibits an uncommon decrease after about $6 \cdot 10^{-4}$ s. In general, deviations from the common temperature versus time curve which are not reproducible are considered to be distortions and are not related to activated processes in the sample. Therefore, each distortion will not be discussed in detail, just general reasons for distortions are summarized and discussed below. Despite this distortion in the temperature curve of sample B10, the X-ray patterns were recorded and they are shown in Fig. 4.23d.
The progresses of the crystallization process of the samples B1, B4, B8 and B10 are captured in the X-ray diffraction patterns in Fig. 4.23a-d. The intensity of sample B1 shows broad diffraction peaks in the entire time regime of 1.2 s as an indication of its amorphous nature (Fig. 4.23a). 55 ms after the original discharge, the temperature of the sample B4 increases

again accommodated by the transformation of the broad diffraction peaks into sharp peaks which characterize the crystalline phase (Fig. 4.23b). This crystalline intermittent phase (in the following termed as intermittent phase) disappears at 0.7 s and is replaced by diffuse peaks in the q-range of the first and second initial amorphous maximums. However, several crystalline peaks are visible as well which will be identified in below. The diffuse maxima which occurred at 0.7 s transform 0.25 s after they appeared into sharp peaks which correspond to the final phase. The same behavior can be observed for the faster heated sample B8, but the intermittent phase already occurs 5 ms after the discharge started and lasts only for 0.1 s. The duration of the second diffuse maximum is about 0.3 s and thus remains unaffected by the heating rate. When the sample B10 is heated with the highest heating rate the behavior changes. After the discharge started, there is a diffuse maximum for about 0.25 s which is accompanied by sharp peaks of the final phase (Fig. 4.23d). The aforementioned intermittent phase does not occur at all. Instead, the sample directly transforms into the final phase.

The intermittent phase and the final phase of ribbon B can also be assigned to the Zr_2(Cu,Al)

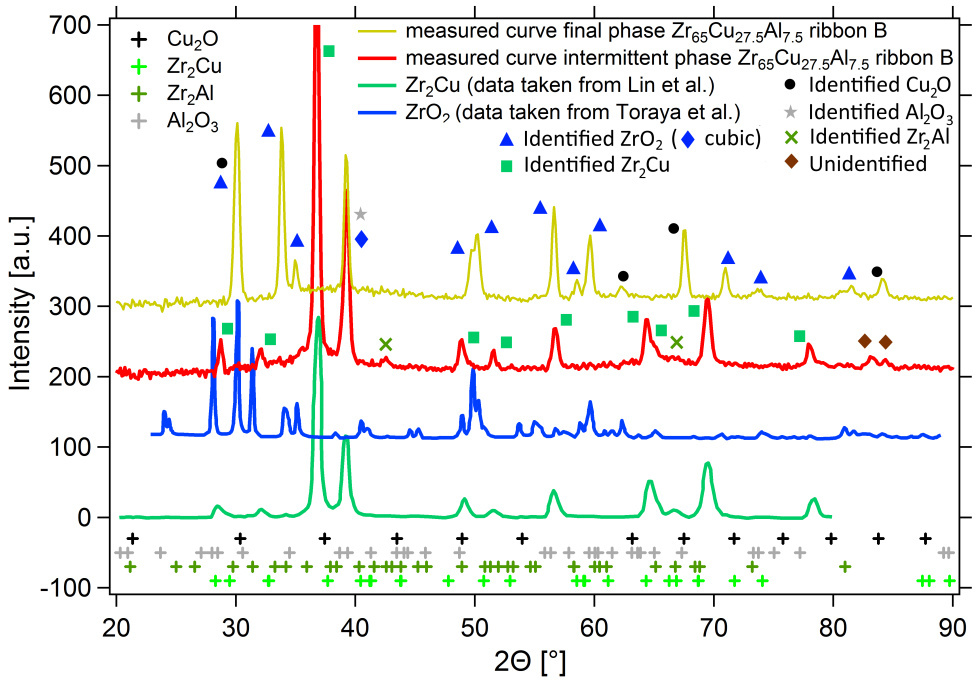

Figure 4.24: Identification of the crystalline peaks of the intermittent and the final phase of ribbon B.

on one hand and to the ZrO_2 and the Cu_2O on the other one, respectively (Fig. 4.24). However, the spectrum of the intermittent phase of ribbon B slightly differs from the intermittent phase of ribbon A. The peaks of the intermittent phase in the spectrum of ribbon A at 35.1° and 38.7° which were assigned to the Zr_2Al phase do not appear in the spectrum of ribbon B.

Fig. 4.25 shows the temperature versus time curve of sample C which consists of $Zr_{45}Cu_{45}Al_{10}$.

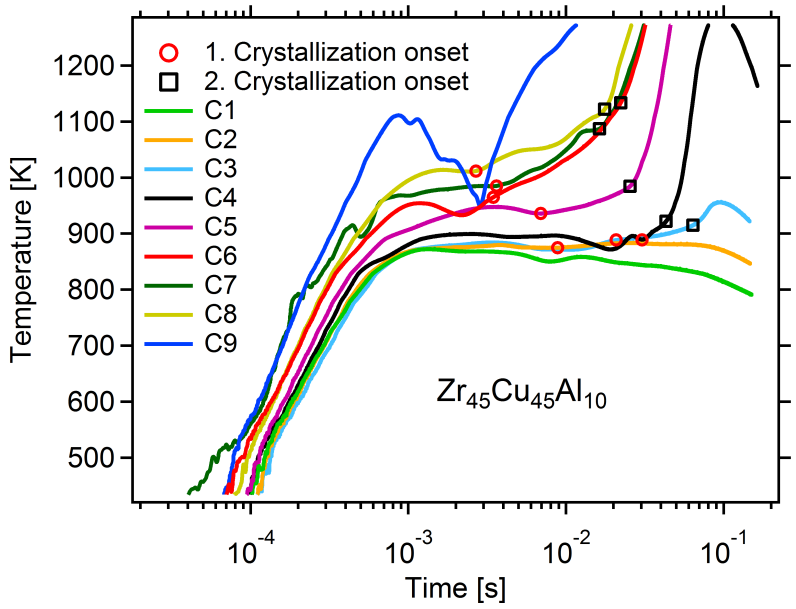

Figure 4.25: Various rapid heating experiments of the metallic glass $Zr_{45}Cu_{45}Al_{10}$. The circles mark the onset of the primary crystallization process while the crosses indicate the start of the secondary crystallization process.

The sample with the highest heating rate C9 again exhibits a similar distortion as sample B9 which manifests in a decrease around 1100 K and therefore the crystallization temperature cannot be identified. However, it is noticeable that the temperature increases again significantly after $2.5{\cdot}10^{-3}$ s. At this time the discharge is already over and therefore, this increase suggests a crystallization event. At the highest crystallization temperature of 1012 K, the crystallization takes place after $2.6{\cdot}10^{-2.7}$ s. At the lowest temperature of 889 K the crystallization is activated after $3{\cdot}10^{-2}$ s. A second crystallization event which follows the first one is also visible. This behavior was also observed in the measurements of the same composition in Fig. 4.18.
The temporal evolutions of the X-ray diffraction patterns of samples C are shown Fig. 4.26. The crystallization behavior does not seem to be affected by the change in the crystallization temperature due to the variations in the heating rate. The temporal evolution enhanced by the chopper is sufficient to record a number of frames in case of sample C5 after the first crystallization but before the second crystallization event sets in.

Fig. 4.27 shows a closer analysis of the X-ray diffraction intensities during the temperature increase due to the two crystallization events. The crystalline phase does not seem to change between the two crystallization stages. But apparently, the first crystallization stage rather promotes the increase of the peaks which belong to the ZrAl phase besides the Zr_2Cu while only peaks belonging to the Zr_2Cu are enhanced during the second crystallization stage.

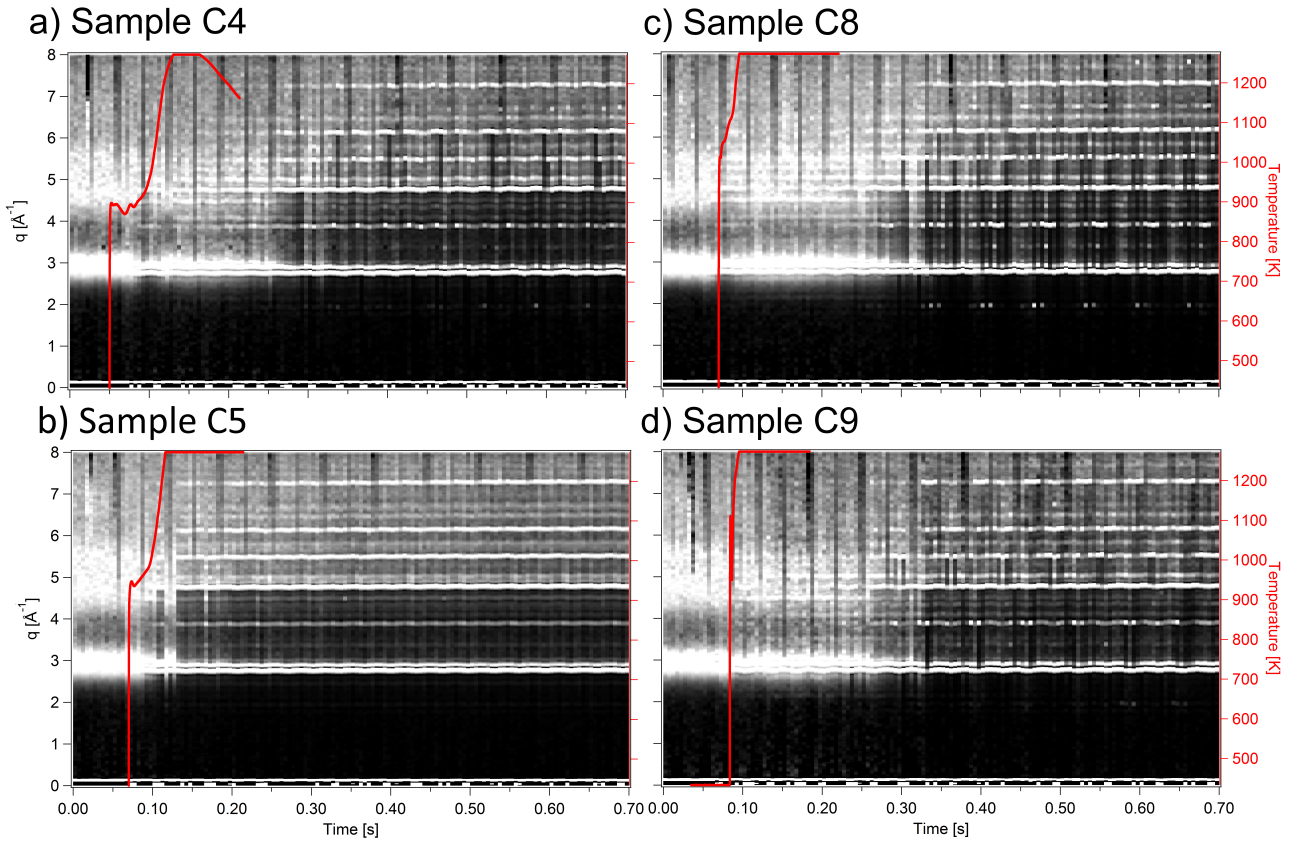

Figure 4.26: Temporal evolution of X-ray diffraction patterns of four different measurements of ribbon C.

The temperature versus time curves of ribbon D with a nominal composition of $Zr_{66.5}Cu_{33.5}$ shows that we observed the highest crystallization temperature of this composition at 871 K after $1.1{\cdot}10^{-3}$ s (Fig. 4.28). At the lowest crystallization temperature of 685 K the crystallization occurs after $6.1{\cdot}10^{-2}$ s. The temperature curves of the samples D4 and D5 exhibit an earlier temperature increase (at 704 K after $1.2{\cdot}10^{-2}$ s and at 734 K after $1.2{\cdot}10^{-2}$ s, respectively) due to crystallization than the sample D6 which crystallizes after $2.0{\cdot}10^{-2}$ s at a higher temperature of 765 K. Additionally to this observation, the shape of the temperature increase due to crystallization of sample D5 and sample D3 distinguish from the shape of the temperature increases of the other samples. These two observations may indicate that the primary crystalline phase of sample D5 and possibly also the primary crystalline phases of sample D3 and D4 are different in comparison to the other samples wihtin this set of measurements of ribbon D. However, the X-ray diffraction patterns do not reveal any influence of the point in the TTT diagram on the crystallization behavior (see Fig. 4.29).

Several measurements of samples from another ribbon E with the same composition $Zr_{66.5}Cu_{33.5}$ are showing a similar behavior as the measurements of sample D (see Fig. 4.31). At the highest

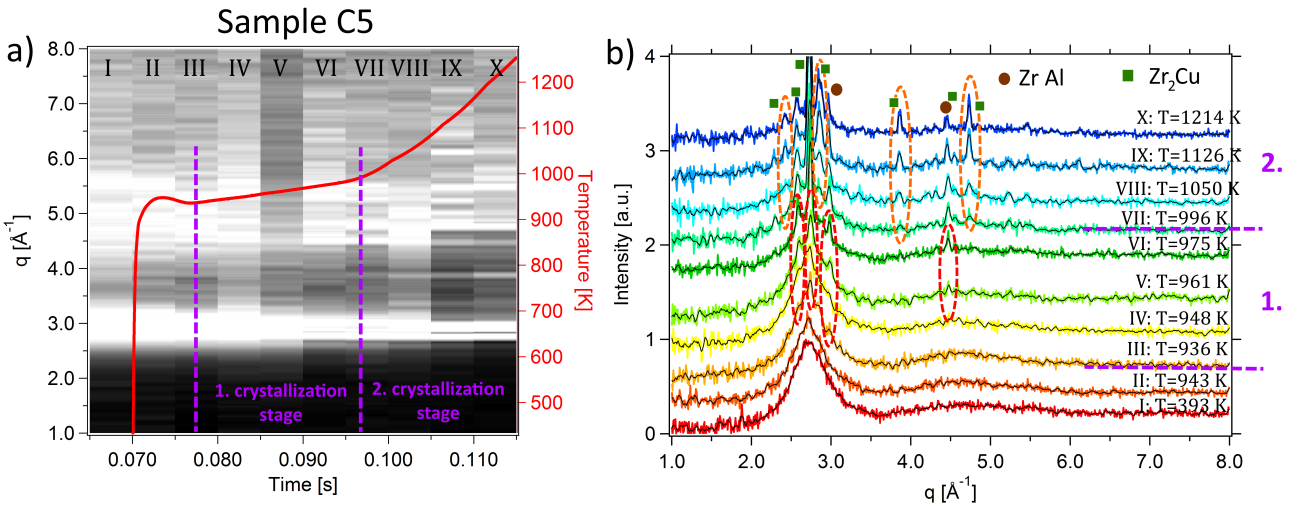

Figure 4.27: a) Sequence of X-ray diffraction frames around the temperature increase due to the capacitor discharge and the crystallization process of sample C5. The slope of the temperature increase during the crystallization changes in the frame number VII. Therefore, we divided the crystallization process into a 1. crystallization stage and a 2. crystallization stage. b) Analysis of the X-ray diffraction intensities during the first and second crystallization stage. The black lines which are superimposed to each curve represent the smoothed version of each curve. Red ellipsoids highlight the peaks which are primarily formed within the first crystallization stage orange ellipsoids highlight the peaks which are formed during the second crystallization stage additionally to the ones formed during the first stage. The given temperature value corresponds to the average temperature during each section.

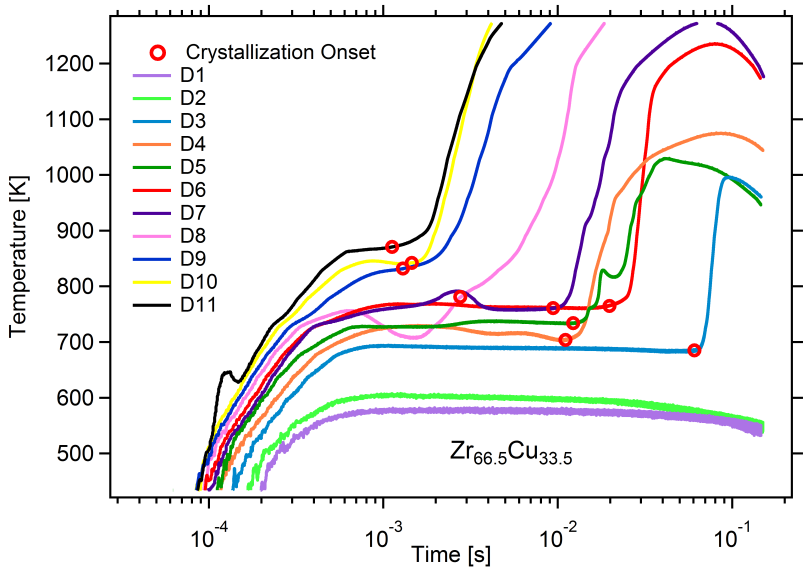

Figure 4.28: Various rapid heating experiments of the metallic glass $Zr_{66.5}Cu_{33.5}$. The circles mark the onset of the crystallization process.

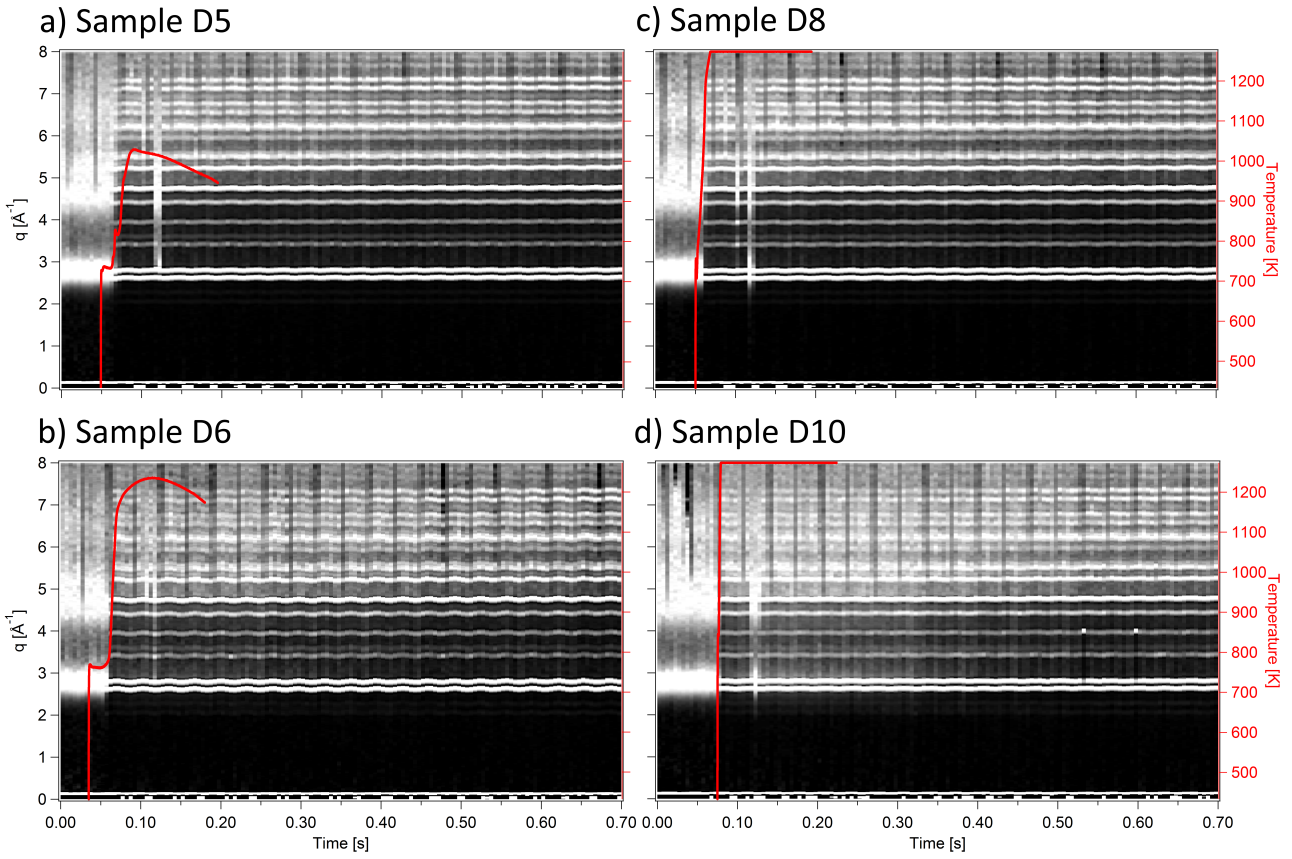

Figure 4.29: Temporal evolution of X-ray diffraction patterns of four different measurements of ribbon D.

crystallization temperature of 970 K the crystallization sets in after $1.1{\cdot}10^{-3}$ s. At the lowest crystallization temperature of 769 K the crystallization starts after $5.1{\cdot}10^{-2}$ s.

The progresses of the crystallization process of the samples E5, E7, E8 and E13 is displayed in the evolution of the X-ray diffraction images in Fig. 4.31. For the three lowest crystallization temperatures shown here, the crystallization sequence is not affected by the change in crystallization temperature. At the highest crystallization temperature which occurs in the measurement of sample E13 the crystallization behavior changes. First the system crystallizes in the same phase as the other three samples E5, E7 and E8. Around 0.22 s later the peaks around the q-value of the first amorphous phase broaden and a rather diffuse regime establishes. Several peaks at higher q-values disappear and around 0.16 s after the initial phase disappeared the system assembles in another crystalline phase which is accommodated with the end of diffuse regime. The crystalline peaks belong to the final phase which does not change anymore until the end of the measurement. This behavior is similar to the behavior observed in the ribbons A and B. The position of the peaks of ribbon D match well with the peaks of the spectrum of the Zr_2Cu phase (Fig. 4.32). This is also the case for the exemplary curve of

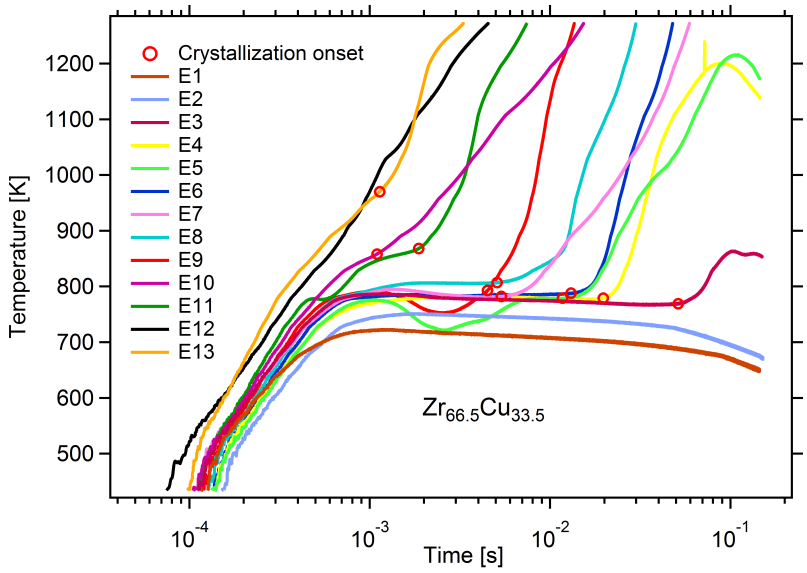

Figure 4.30: Various rapid heating experiments of the metallic glass $Zr_{66.5}Cu_{33.5}$. The circles mark the onset of the crystallization process.

sample E5, however there two unidentified peaks at 38.7° and 42.1°. The intermittent phase of sample E13 coincides well with Zr_2Cu phase. The final phase of sample E13, in turn, can be assigned to the Zr_2O phase and the Cu_2O. Hence, for the highest heating of the composition $Zr_{66.5}Cu_{33.5}$ we observe a similar behavior as for the majority of the measurements of the composition $Zr_{65}Cu_{27.5}Al_{7.5}$ (ribbons A and B).

4.10 Relationship between second temperature increase and X-ray diffraction pattern

As mentioned above, during the measurements at the synchrotron beamline P07 we used the high speed pyrometer Kleiber KGA 740 with a temperature regime of 433 - 1273 K. In several measurements the sample temperature exceeded the available temperature regime of the pyrometer which limits the temperature assignment to the X-ray data. Therefore, we performed additional measurements with the ribbons B and F with the nominal composition $Zr_{65}Cu_{27.5}Al_{7.5}$ additionally with the high speed pyrometer IGA 740 with the same temporal resolution as the previous one but with a higher temperature regime of 573 - 2573 K (shown in Fig. 4.33). These measurements are presented in this section. We tried to cover a comparable range of heating rates and thus crystallization temperatures.

The temperature versus time curve of the measurements shown in Fig. 4.33a exhibit a first temperature increase which is caused by the capacitor discharge before they reach a nearly con-

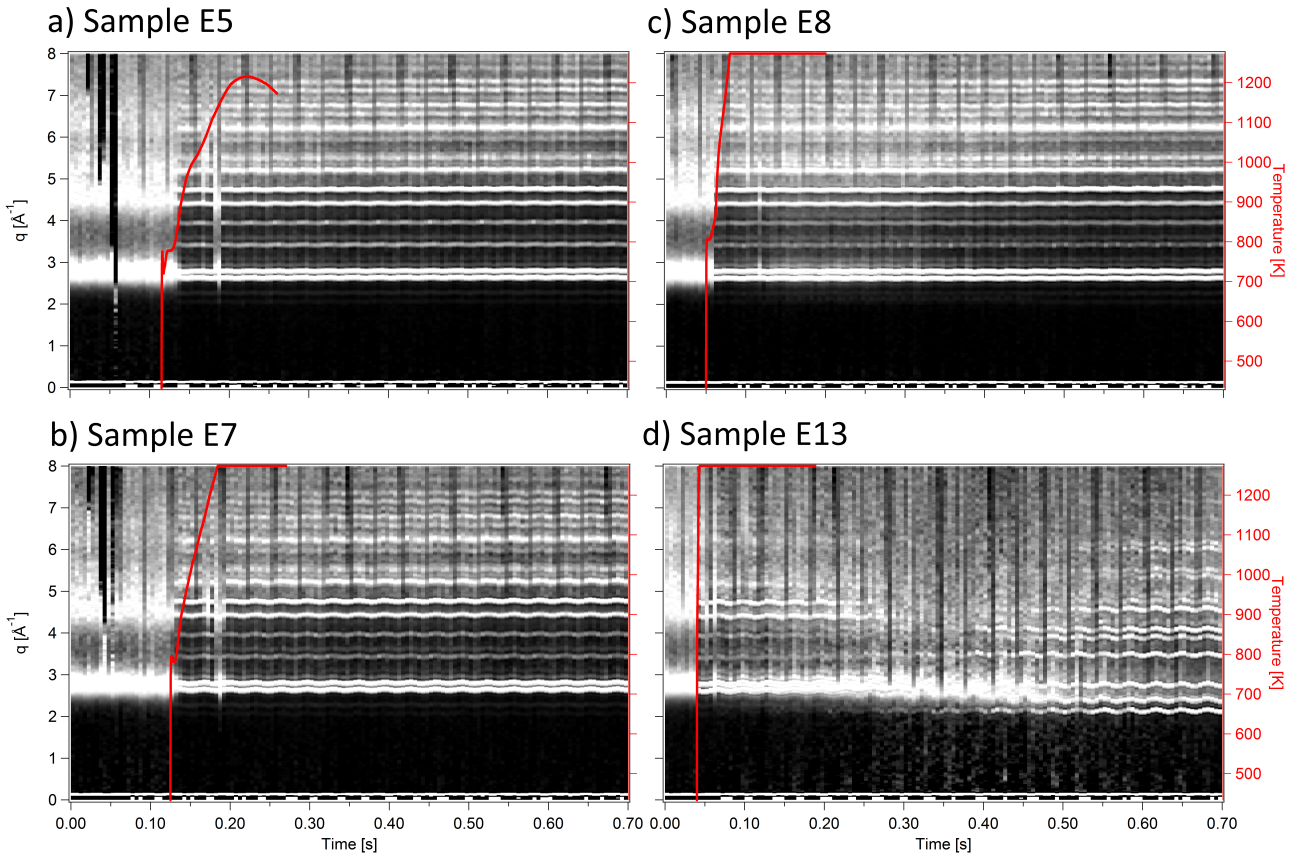

Figure 4.31: Temporal evolution of X-ray diffraction patterns of four different measurements of ribbon E.

stant temperature regime. At the end of this plateau the temperature increases again due to a crystallization as already observed in previous measurements. At around 1350 K the increase ends with a maximum followed by a minimum before the temperature starts rising again for a third time. We labeled the time interval between the onset of the second increase in the temperature versus time curve and the subsequent maximum with Δt. The duration of this temperature increase matches well with the lifetime of the intermittent Zr_2(Cu,Al) phase of ribbon B (see Fig. 4.33b).

4.11 Identification of the third increase in the temperature versus time curve

This section is devoted to the analysis of the third increase in the temperature versus time curve observable in Fig. 4.33a. We already saw, for instance in the curves of Fig. 4.25 and Fig. 4.28, that this third increase is not a universal feature of all temperature evolutions after

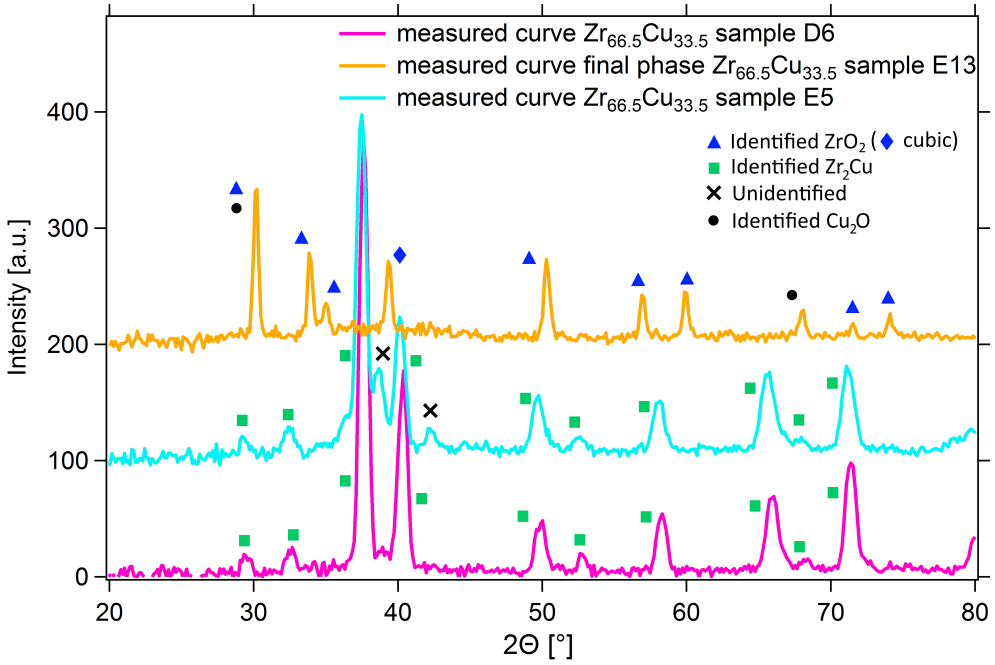

Figure 4.32: Identification of the crystalline phases of sample D and E.

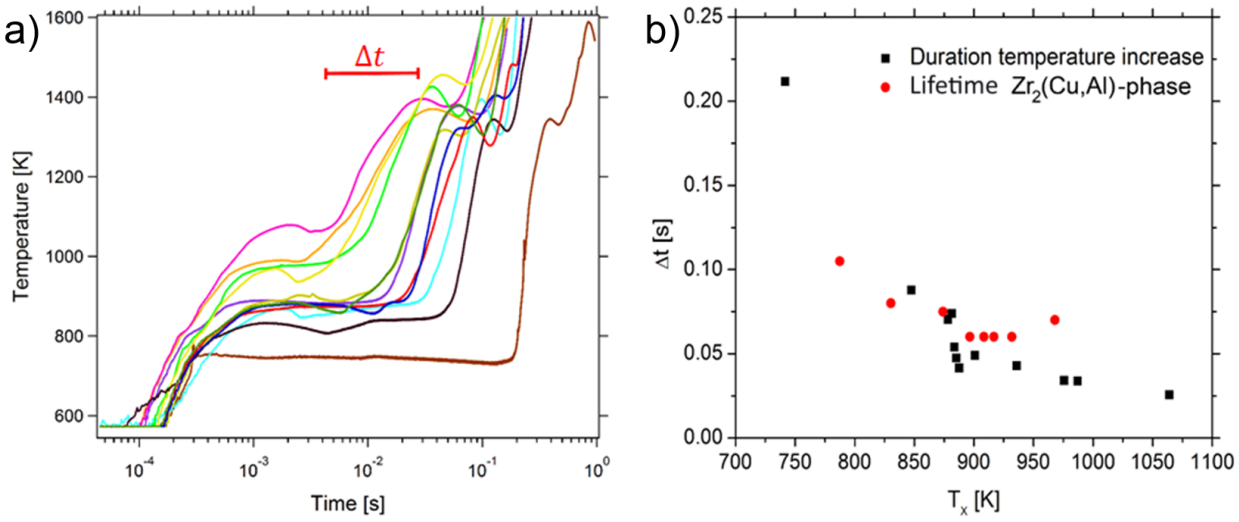

Figure 4.33: a)Temperature versus time curve of several samples of $Zr_{65}Cu_{27.5}Al_{7.5}$ during crystallization measured with high temperature pyrometer IGA 740. b) Comparison between the time interval Δt of the second increase in the temperature versus time curve which is caused by crystallization with the duration of the intermittent crystalline Zr_2(Cu,Al) phase observed in the temporal evolution of X-ray diffraction patterns of ribbon A, B, E. Here, we used the data for the duration of the Zr_2(Cu,Al) phase of ribbon B which exhibits the same composition as the samples in the measurements of panel a). Figure taken from [61].

the discharge. We tested the hypothesis whether the third increase is related to structural changes at high temperatures. The composition $Zr_{65}Cu_{27.5}Al_{7.5}$ transforms after the end of the intermittent phase eventually into the Zr_2O phase. Therefore, we performed a number of discharge experiments with ribbons made of $Zr_{65}Cu_{27.5}Al_{7.5}$ in a protective Argon atmosphere with a purity of 6.0.

In the rapid heating experiments in the protective Argon atmosphere the temperature decays

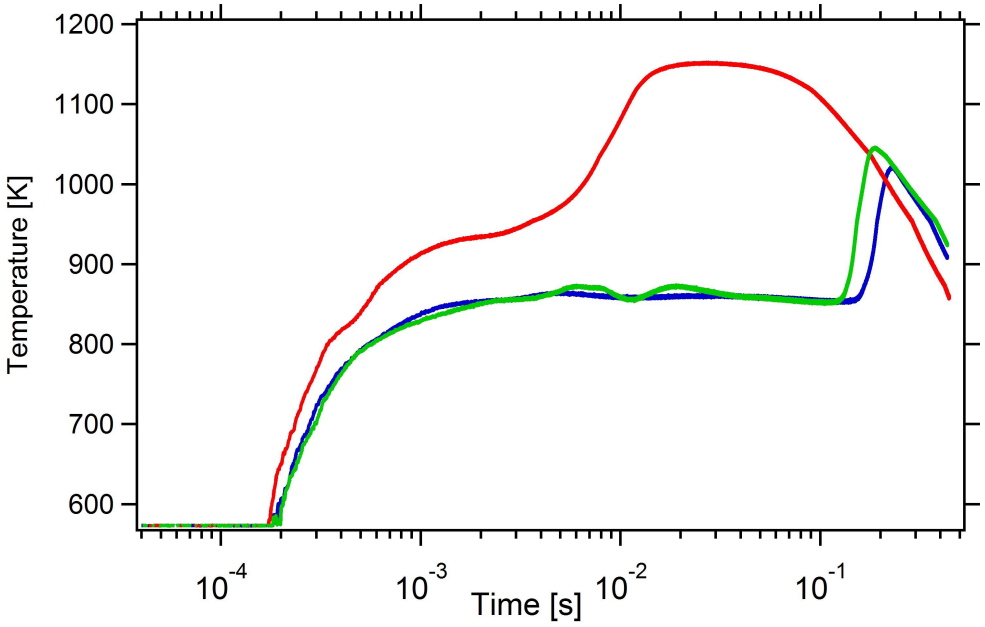

Figure 4.34: Temperature versus time curve during crystallization of $Zr_{65}Cu_{27.5}Al_{7.5}$ sample in Argon

after the second increase without rising a third time. The maximum temperature reached after the second increase is 1150 K which is significantly lower than 1350 K as observed in the measurements in air shown in Fig. 4.33a. Therefore, we conclude that the third increase in the temperature versus time curve is caused by oxidation.

4.12 Analysis of crystallized volume fraction

For ribbon A with the composition of $Zr_{65}Cu_{27.5}Al_{7.5}$ we analyzed the crystallization behavior further. For the calculation of the crystallized volume fraction we are restricted to the q-range from 1 to 6 $Å^{-1}$, because, to our knowledge, there was no literature data of the Bragg peak positions for primary crystalline phase Zr_2(Cu,Al) available for higher values. In order to determine the crystallized volume fraction, it is most crucial to seperate the crystalline from the amorphous contribution in the diffraction profiles [60]. For this purpose we fitted the total

diffraction intensity with a single function. In this function we attribute a multiple Gaussian fit to the Bragg peaks of the crystalline phase, a Pseudo-Voigt function [60] in order to describe the amorphous maxima and the background was fitted with polynom of second order. Before we analyzed a diffraction pattern during the crystallization process we fitted the first three maxima of a purely amorphous spectrum with a multiple Pseudo-Voigt function (see Fig. 4.35).

$$I_{am}(q) = \sum_{i=1}^{3} A_{am,i} \left[\eta_i \cdot \exp\left(-\ln(2) \cdot 4 \left(\frac{q - q_{am,max,i}}{\beta_{am,i}} \right)^2 \right) + (1 - \eta_i) \frac{1}{1 + 4\left(\frac{q - q_{am,max,i}}{\beta_i} \right)^2} \right] \tag{4.5}$$

The result of this fit, particularly the full widths at half maximum (FWsHM) $\beta_{am,1} = 0.37776$, $\beta_{am,2} = 0.7$ and $\beta_{am,3} = 0.7$, the absolute heights of the maxima $A_{am,1} = 60.23$,$A_{am,2} = 9.0481$ and$A_{am,3} = 3.5676$ and the Gaussian content $\eta_1 = 0.16354$,$\eta_2 = 0$ and $\eta_3 = 1$ is kept constant and is used for the next fit of the partially crystallized diffraction profiles. The positions of the amorphous maxima $q_{am,max,i}$ still remain variable in order to allow shifts during thermal expansion. It is visible that the second amorphous maximum can be modeled only with a Lorentzian contribution and the third amorphous maximum requires only a Gaussian part to describe the curve. The FWHM of the second and the third peak were partly varied manually because the fitting program tends to overemphasize one of the peaks.

For the fit of the entire, partially crystallized diffraction pattern we used the following function,

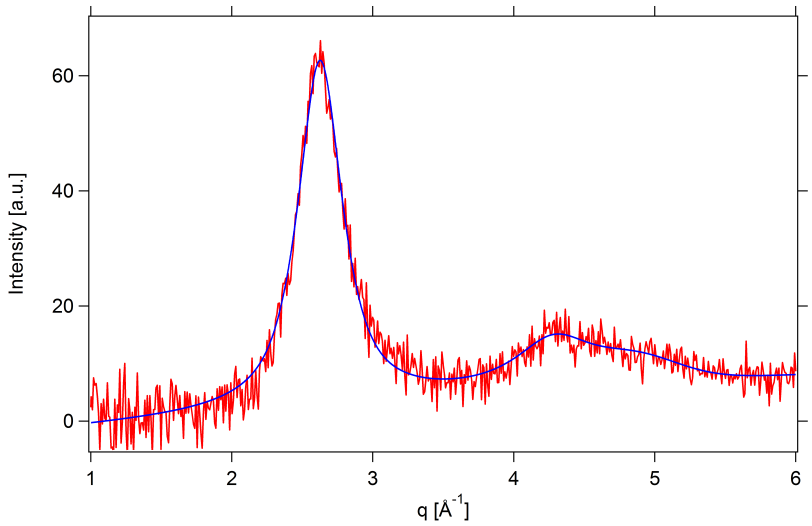

Figure 4.35: Multiple Pseudo-Voigt Fit of the purely amorphous diffraction patterns before the heating starts.

where the Bragg peaks are described by a Multiple Gaussian function [60]:

$$I_{total}(q) = \sum_{j=1}^{10} a_{cr,j} \exp\left(-ln(2) \cdot 4\left(\frac{q - q_{cr,max,j}}{\beta_{cr,j}}\right)^2\right) \tag{4.6}$$

$$+A_{am,rel} \cdot 60.23 \cdot 0.16354 \cdot \exp\left(-\ln(2) \cdot 4\left(\frac{q - q_{am,max,1}}{0.37776}\right)^2\right) \tag{4.7}$$

$$+A_{am,rel} \cdot 60.23 \cdot (1 - 0.16354) \frac{1}{1 + 4\left(\frac{q - q_{am,max,1}}{0.37776}\right)^2} \tag{4.8}$$

$$+A_{am,rel} \cdot 9.0481 \cdot \frac{1}{1 + 4\left(\frac{q - q_{am,max,2}}{0.7}\right)^2} \tag{4.9}$$

$$+A_{am,rel} \cdot 3.5676 \cdot \exp\left(-\ln(2) \cdot 4\left(\frac{q - q_{am,max,3}}{0.7}\right)^2\right) \tag{4.10}$$

$$+b_0 + b_1 \cdot q + b_2 \cdot x^2 \tag{4.11}$$

The line 4.6 corresponds to the Gaussian fits of the Bragg peaks with the height of the j-th Bragg peak $a_{cr,j}$, its position $q_{cr,max,j}$ and its FWHM $\beta_{cr,j}$. We allowed a maximum number of 10 crystalline peaks which form during crystallization because we found 10 crystalline peaks which belong to the dominant Zr_2(Cu,Al) phase found in section 4.9 in the lines 4.7-4.10 are the fits of the amorphous maxima which include the results for the FWHM, the heights of the peaks and the Gaussian content from the previous fit of the purely amorphous profile. The parameter $A_{am,rel}$ is the peak height of the amorphous contribution in the partially crystallized profile relative to the peak height of the purely amorphous profile and therefore it varies between 0 and 1. The quantities b_i of the polynomial contribution model the remaining background which was not entirely removed by the procedure described in section 3.14. The fit of the partially crystallized profile is shown in Fig. 4.36 (blue curve). The difference between the data points and the fit verifies a good agreement (see Fig. 4.36 bottom panel).

With the information from the fits it is possible to separate the crystalline from the amorphous contribution in the partially crystallized diffraction pattern and therefore we can make a statement about the crystallized volume fraction according to equation 2.10. As expected, the crystallized volume fraction X_{cryst} versus the scattering vector q of the measurement shown in Fig. 4.36 increases at the positions of the Bragg peaks and decreases in between (Fig. 4.37). For the value of the crystallized volume fraction of the entire diffraction pattern we used the last analyzed value $X_{cryst}(q = 6.0)$.

We analyzed the crystallized volume fraction of the samples of ribbon A which crystallize into the Zr_2(Cu,Al) phase and connected the value $X_{cryst}(q = 6.0)$ of each frame to the time where

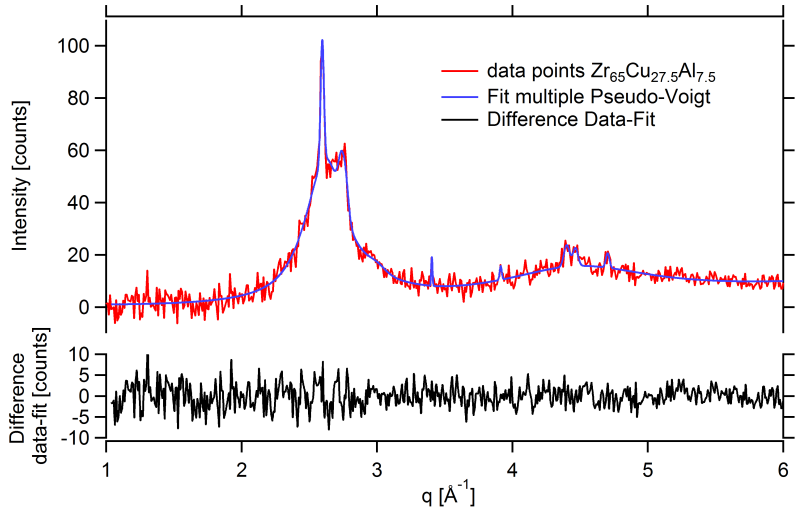

Figure 4.36: The top panel shows an exemplary, partially crystallized diffraction profile of a sample made of $Zr_{65}Cu_{27.5}Al_{7.5}$ (red curve) and a multiple Gaussian fit (blue curve). The bottom panel shows the difference between the data points of the diffraction profile and the fit.

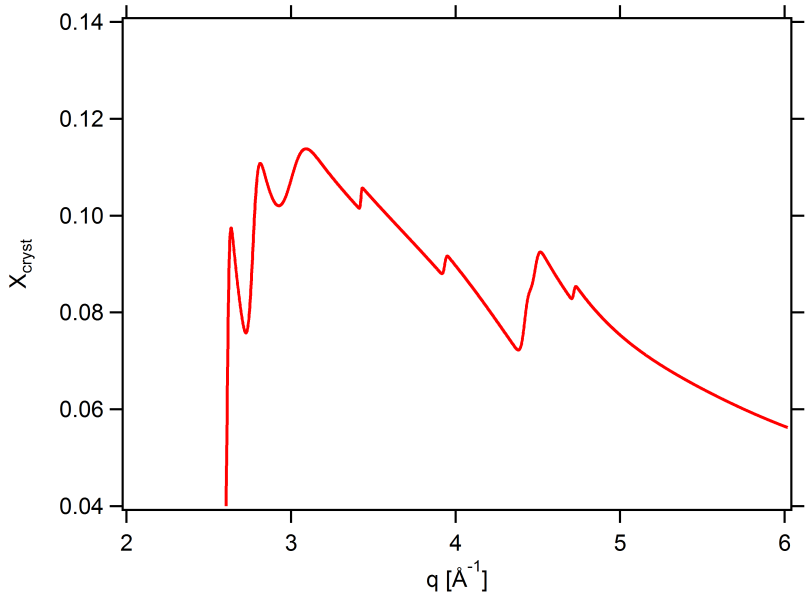

Figure 4.37: Exemplary crystallized volume fraction as a function of scattering vector in the q-range of 1 to 6 Å^{-1}.

the illumination of the frame ends (Fig. 4.38). In all the curves the increase in the crystallized volume fraction ends suddenly at a certain value between 30 and 50 %. It is also noticeable that the slope of the X_{cryst}-increase rises from sample A1 (black curve) to sample A4 which exhibits the highest slope. This is not correlated to the crystallization temperature which is the highest for the sample A9 (dark green curve). The increase of the crystallized volume fraction can be well approximated by the Johnson-Mehl-Avrami (JMA) equation 2.9. The fitting parameter k

represents the aforementioned change in slope of X_{cryst} with the temperature where the sample crystallizes (Fig. 4.39).

Despite the fact that the JMA model fits the data well, the interpretation of the resulting

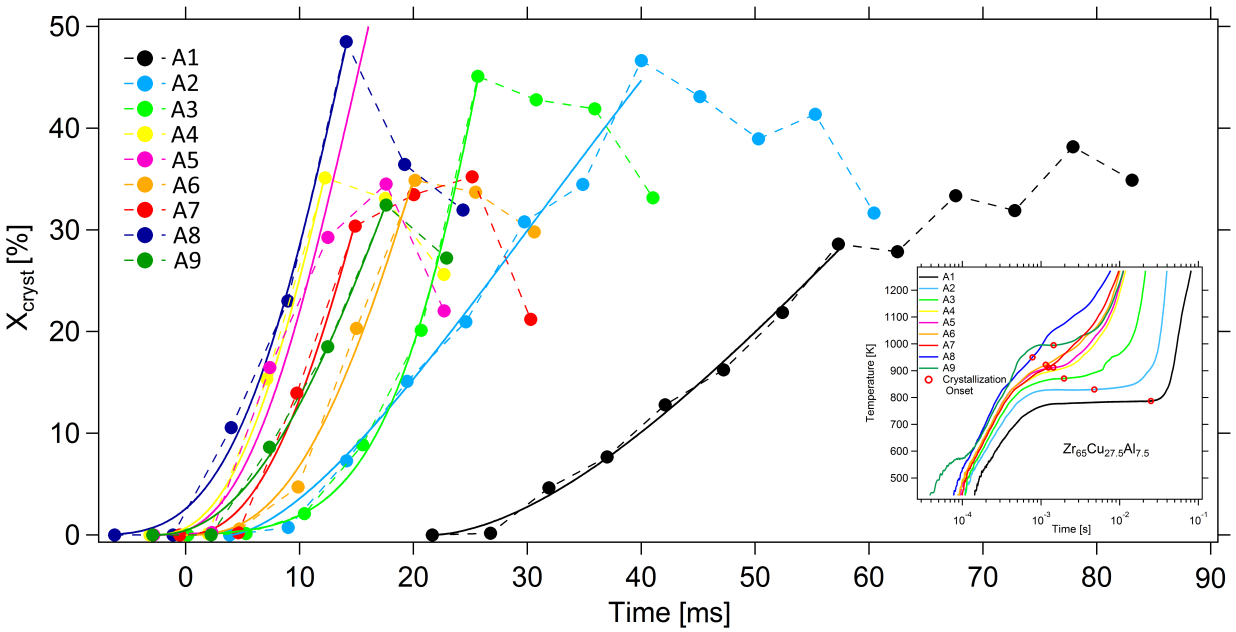

Figure 4.38: Crystallized volume fraction for the samples of ribbon A which crystallize into the Zr_2(Cu,Al)-phase. The solid lines are JMA-fits. The inset shows the temperature versus time curves of the samples of ribbon A during rapid heating which is copied from Fig. 4.19.

parameters can be misleading when the application of the model is not verified. First, the JMA model was designed for isothermal crystallization behavior and for non-isothermal experiments it can only applied in a very limited number of cases [57]. Particularly, for non-isothermal conditions it needs to be verified that the nucleation process is already finished when the crystal growth process starts [57] so that the number of nuclei does not change any more during the crystallization process. A common test of the applicability of the JMA model is to test the linearity of the plot $\ln(-\ln(1-\alpha))$ versus the inverse temperature. However, even if the resulting is curve is linear the application of the model is not valid and only a SEM study of the crystallization behavior can bring a conclusive result [1].

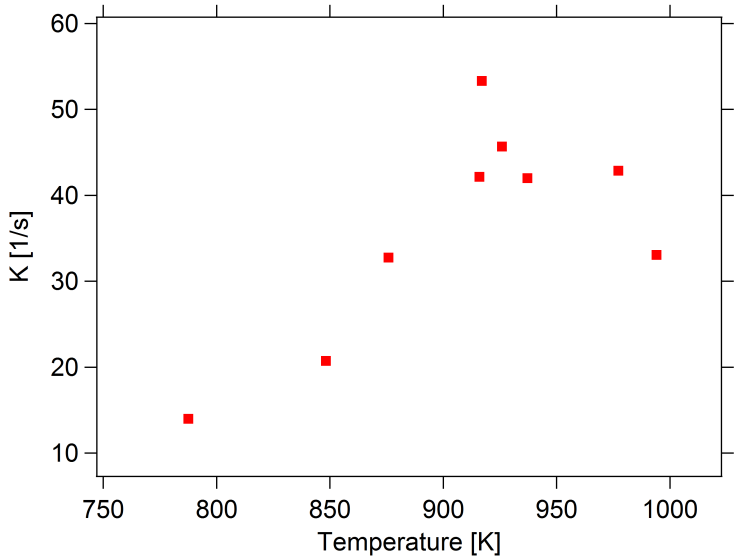

Figure 4.39: Graph of the fitting parameter k of the VFT fit as a function of the temperature where the sample crystallizes.

4.13 Very fast heating measurements that bypass the crystallization nose in $Zr_{65}Cu_{27.5}Al_{7.5}$

As mentioned above, the temperature curve during the in-situ X-ray measurements at the synchrotron of the sample B10 was not recorded properly (Fig. 4.22). This measurement is particularly interesting because it was heated with the highest rate within this set of measurements and it is the only measurement where the intermittent crystalline Zr_2(Cu,Al) phase was not detected anymore. Instead the sample directly devitrifies in the ZrO_2 phase. In order to check whether this change in the crystallization behavior is accompanied with a signature in the temperature versus time curve, we heated up three samples of the composition $Zr_{65}Cu_{27.5}Al_{7.5}$ with the attempt to reproduce the heating rate of sample B10 (Fig. 4.40a).

Here, the temperatures of the samples Air 1, Air 2, Air 3 do not decrease around 1038 K, instead the temperatures continue to rise until 1260 K, 1201 K and 1231 K, respectively, where all three curves exhibit a maxima. The subsequent minima are followed by another increase. At the time between $5.5 \cdot 10^{-4}$ s and $6.9 \cdot 10^{-4}$ s where the temperature graphs start to decrease, the capacitor is not fully discharged which can be seen in the inset of Fig. 4.40a. The temperature increase after the minimum may be caused by the heating due to the remaining charge of the capacitor. In the case of sample Air 1 the current signal suddenly drops at $3.99 \cdot 10^{-4}$ s which is most likely related to the failure of the sample.

The specific heat capacity of the samples Air 1, Air 2 and Air 3 exhibit a pronounced maximum at the glass transition temperature which occurs at 797 K, 766 K, and 770 K, respectively. The

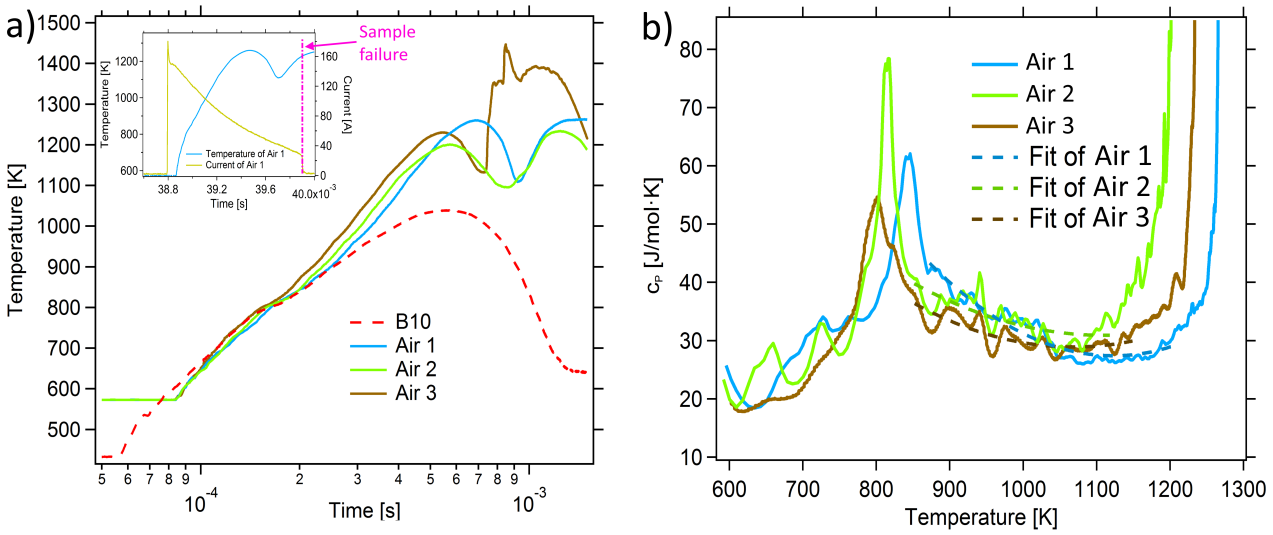

Figure 4.40: a) Temperature versus time curve of three rapid heating measurements which have a similar heating rate as sample B10. The inset shows the current and temperature versus time of sample Air 1. b) Specific heat capacity of the measurements shown in panel a). The dashed lines represent second order polynomial fits of the supercooled liquid region.

specific heat capacity in the supercooled liquid region decreases before it strongly increases. This increase is related to the maximum in the temperature versus time curve of each curve. The differences between the specific heat capacity in the glassy state and the one in the supercooled liquid state measured at the glass transition temperature are 20.44 J/mol·K, 15.25 J/mol·K and 8.62 J/mol·K.

Busch et al. predicted a T^2-dependence of the specific heat capacity in the supercooled liquid. We tried to verify this behavior. Therefore, we fitted the specific heat capacity in the supercooled liquid region with a second order polynomial: $f(T) = a_0 + a_1 \cdot T + a_2 \cdot T^2$.

We calculated the correlation coefficient from a graph where we plotted the specific heat

	a_0 $[J/(mol \cdot K)]$	a_1 $[J/(mol \cdot K^2)]$	a_2 $[J/(mol \cdot K^3)]$	$Kor(f(T), c_P)$
Air 1	348.29 ± 13.6	$-5.7164 \cdot 10^{-1} \pm 2.62 \cdot 10^{-2}$	$2.5459 \cdot 10^{-4} \pm 1.25 \cdot 10^{-5}$	0.958
Air 2	194.15 ± 38.8	$-2.9391 \cdot 10^{-1} \pm 7.88 \cdot 10^{-2}$	$1.3229 \cdot 10^{-4} \pm 3.98 \cdot 10^{-5}$	0.789
Air 3	211.28 ± 9.8	$-3.4144 \cdot 10^{-1} \pm 1.96 \cdot 10^{-2}$	$1.5981 \cdot 10^{-4} \pm 9.73 \cdot 10^{-6}$	0.819

Table 4.5: Fitting parameters of the second order polynomial fit of the supercooled liquid region.

capacity values $c_{P,i}$ versus the values of the fitting function $f(T)$ (Fig. 4.41)

$$Kor(f(T), c_P) = \frac{\sum_{i=1}^{n}(f_i(T) - \overline{f(T)})(c_{P,i} - \overline{c_P})}{\sqrt{\sum_{i=1}^{n}(f_i(T) - \overline{f(T)})^2 \cdot \sum_{i=1}^{n}(c_{P,i} - \overline{c_P})^2}} \tag{4.12}$$

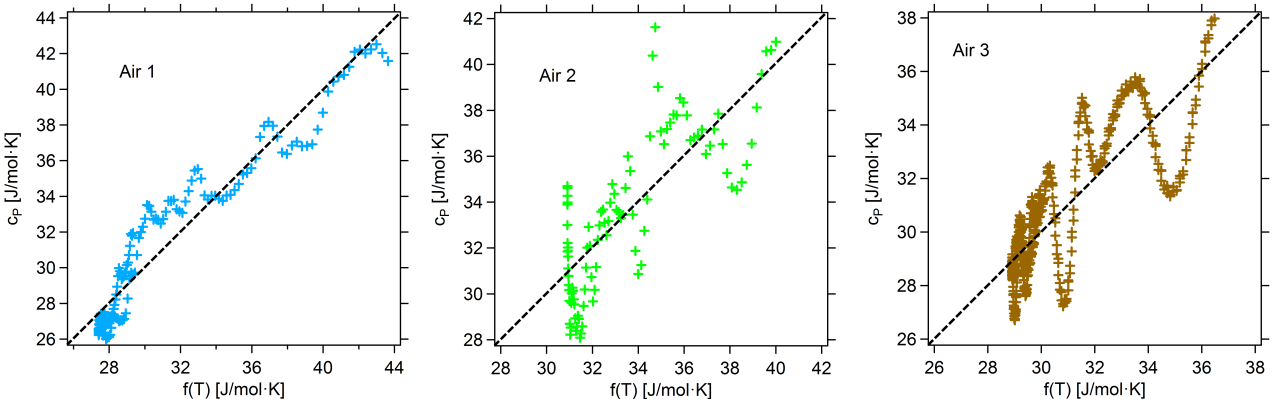

Figure 4.41: Specific heat capacity versus the second order polynomial fitting function for the samples a) Air 1, b) Air 2 and c) Air 3. The dashed lines represent the ideal case where the correlation coefficient is equal to 1.

Here, $\overline{c_P} = \frac{1}{n}\sum_{i=1}^{n} c_{P,i}$ is the mean value of the specific heat capacity values $c_{P,i}$ and $\overline{f(T)} = \frac{1}{n}\sum_{i=1}^{n} f_i(T)$ is the mean value of the fitting function values $f_i(T)$, where n is the number of data points. In the ideal the correlation coefficient is equal to 1. This means that there is a perfect correlation between two quantities x and y and the graph in a y versus x plot is a line with a slope equal to 1. All deviation of the curve from the ideal curve with a slope equal to 1 lowers the correlation coefficient.

The results show that the correlation coefficient of the samples Air 1 and Air 3 show a correlation coefficient above 0.8 which indicates a very strong correlation. The correlation coefficient of sample Air 2 is slightly below 0.8 at a value of 0.789 which means that there is a strong correlation.

In order to obtain more quantitative information about the maximum in the temperature versus time curve, we calculated the enthalpy of this process. For this purpose, we assumed a constant specific heat capacity c_P and extrapolated the temperature versus time curve with the heat transformed into the sample by the capacitor discharge. Therefore, the temperature at a certain time is given by

$$T(t_1) \;=\; T(t_0) + \frac{\int_{t_0}^{t_1} I(t)\cdot U(t)\mathrm{d}t}{c_P m}. \tag{4.13}$$

In this equation we evaluate the energy $\int_{t_0}^{t_1} I(t)\cdot U(t)\mathrm{d}t$ due to the capacitor discharge in the time interval between t_0 and t_1 and the consequent temperature increase from the starting temperature $T(t_0)$ up to the temperature $T(t_1)$. Now, the enthalpy is calculated by the equation $\Delta H = c_P \cdot \Delta T$ where ΔT denotes the maximum temperature difference between the measured and the extrapolated temperature versus time curve. For clarification, the procedure is shown

in Fig. 4.42.

For further analysis and as a confirmation that the samples do not crystallize during heating, we

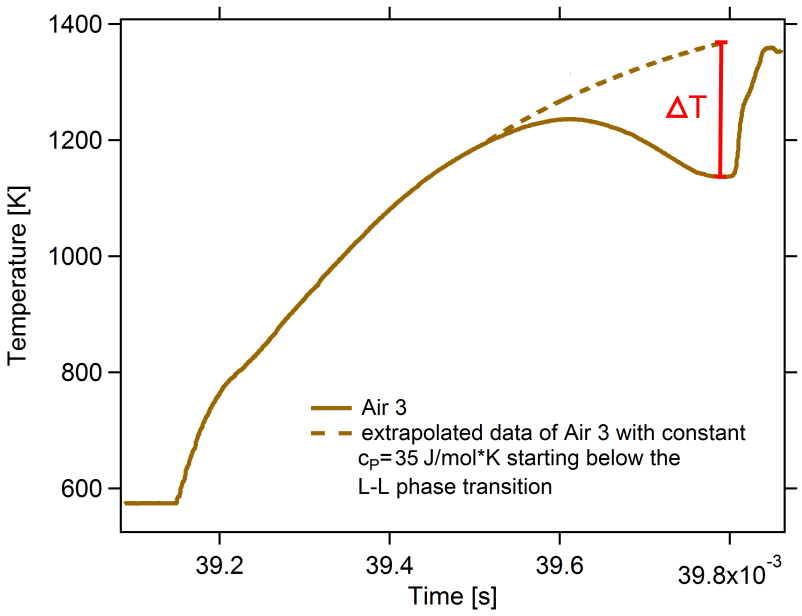

Figure 4.42: Temperature versus time curve of sample Air 3 with a extrapolated curve assuming a constant specific heat value and starting before the transition sets in.

determined the electrical resistance of these measurements by Ohm's law during the discharge process. During the measurement, the resistance of the sample as a function of time decreases at first until 820 K (Fig. 4.43). Above 900 K, the resistance increases with a slope of $6.7 \cdot 10^{-5} \Omega/K$ [61]. Additionally, we heated up several samples with an even higher rate. The corresponding

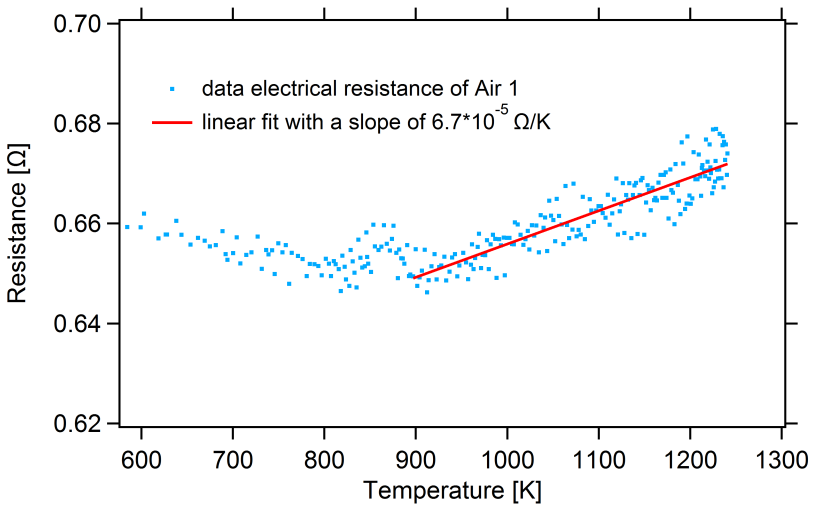

Figure 4.43: Electrical resistance of sample Air 1 as a function of temperature.

temperature versus time curves show a similar behavior as the previous measurements (Fig. 4.44). Here, it is noticeable that the temperature increases significantly further with increasing heating rate. The samples Air 4, Air 5 and Air 6 exhibit a maximum at 1464 K (after $3.56 \cdot 10^{-4}$ s), 1548 K (after $2.34 \cdot 10^{-4}$ s) and at 1336 K (after $3.77 \cdot 10^{-4}$ s), respectively. Sample Air 5 shows a slightly different behavior because it strongly increases after a weak maximum with a much higher slope than the slope due to the capacitor discharge. This behavior will be discussed below.

In order to exclude any influence of oxidation on the temperature curve, we also performed

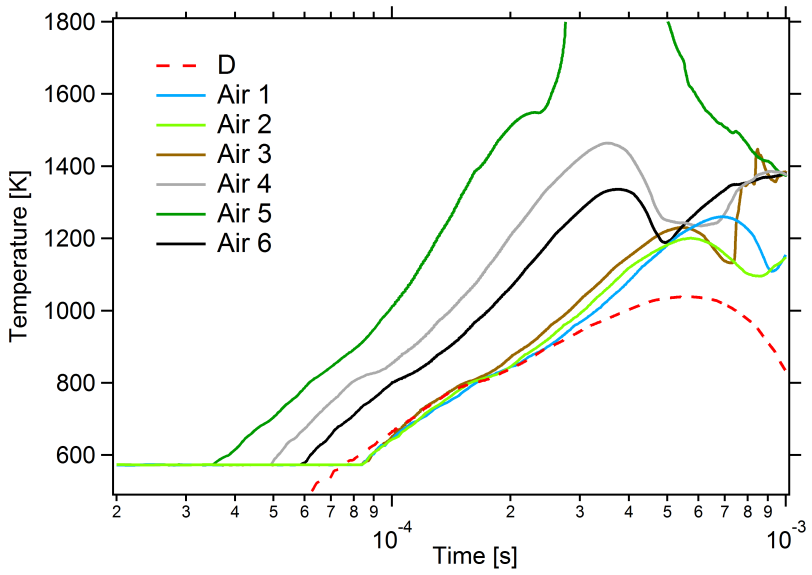

Figure 4.44: Temperature versus time curve of several samples that bypass the crystallization nose. These measurements were performed in air.

a number of measurements in a protective Argon atmosphere with purity of 6.0. The sample Argon 1 exhibits a clear maximum at a lower temperature of 1180 K after $1.87 \cdot 10^{-4}$ s while the samples Argon 2 and Argon 3 exhibit only a plateau before they increase strongly as also observed in the case of Air 5.

As a summary of all the measurements presented in this section, we show all curves in the same plot and indicated the maximum (Fig. 4.46).

4.14 Very fast heating measurements that bypass the crystallization nose in $Pd_{77.5}Cu_6Si_{16.5}$

In order to analyze how universal the phenomenon of the maximum in the temperature versus time curve at high temperatures in the supercooled liquid is, we analyzed a metallic glass ribbon

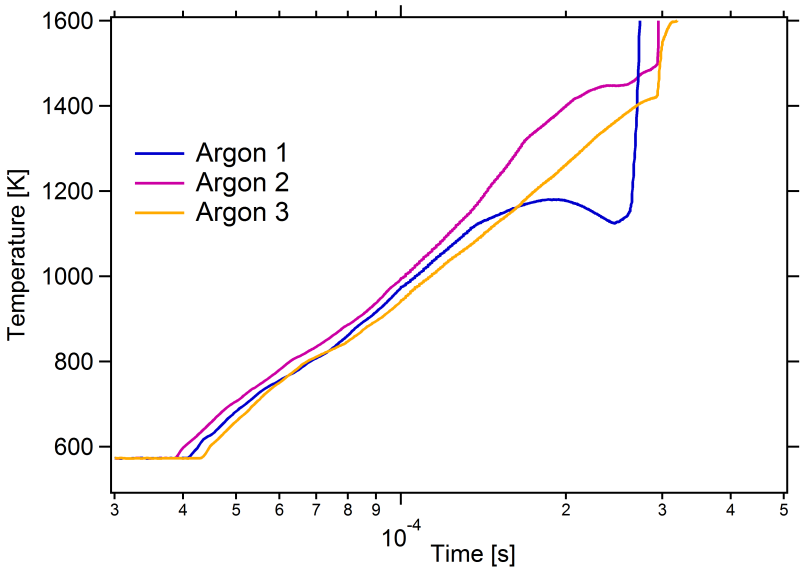

Figure 4.45: Three temperature versus time curves of rapid heating measurements that bypass the crystallization nose performed in a protective argon 6.0 atmosphere.

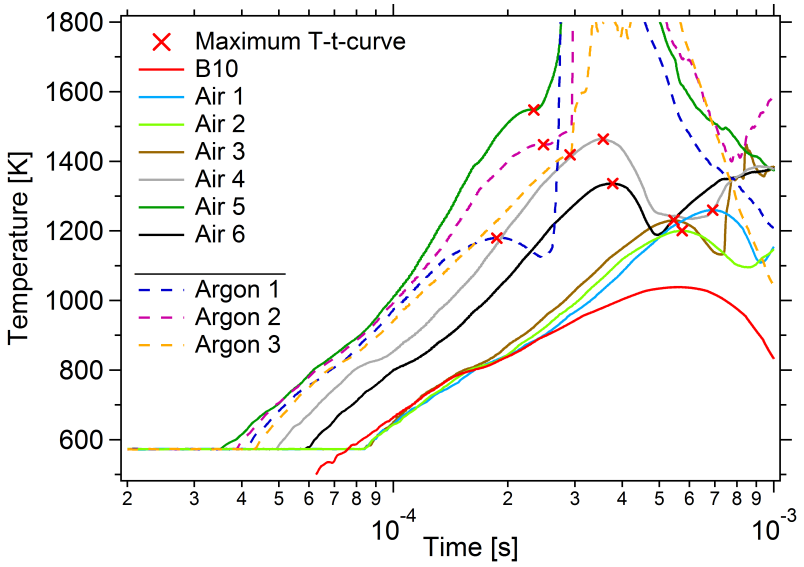

Figure 4.46: Overview of all very fast heating measurements that bypass the crystallization nose. The crosses indicate the maximum or plateau which occur during heating.

made of $Pd_{77.5}Cu_6Si_{16.5}$. In comparison to the Zr-based samples analyzed above, which are rather strong glass formers, this Pd-based alloy has a significantly higher fragility. Therefore, the dynamics and the change in the dynamics with temperature in the supercooled liquid region are different.

Here, we were only able to conduct a small number of three measurements successfully. Mostly after the measurement we could not find the sample in its original shape anymore. Instead, we

found little metallic spheres which were probably formed after the viscosity strongly dropped in the supercooled liquid. Despite this experimental difficulty of the rapidly decreasing viscosity above the glass transition, we tried to fix the sample in its position between the copper holder with a fixture made of pyrogel. Pyrogel is based on silica aerogel and has thermal conductivity around 20 mW/Km at room temperature and 90 mW/Km at 873 K, which is similar or even below the thermal conductivity of air [84].
In these measurements we found an increase which is interrupted by a little kink at the glass transition temperature and which finally ends with a maximum or a plateau in the temperature versus time curve (Fig. 4.47). In these cases the maximums occur at 960 K after $2.6 \cdot 10^{-4}$,

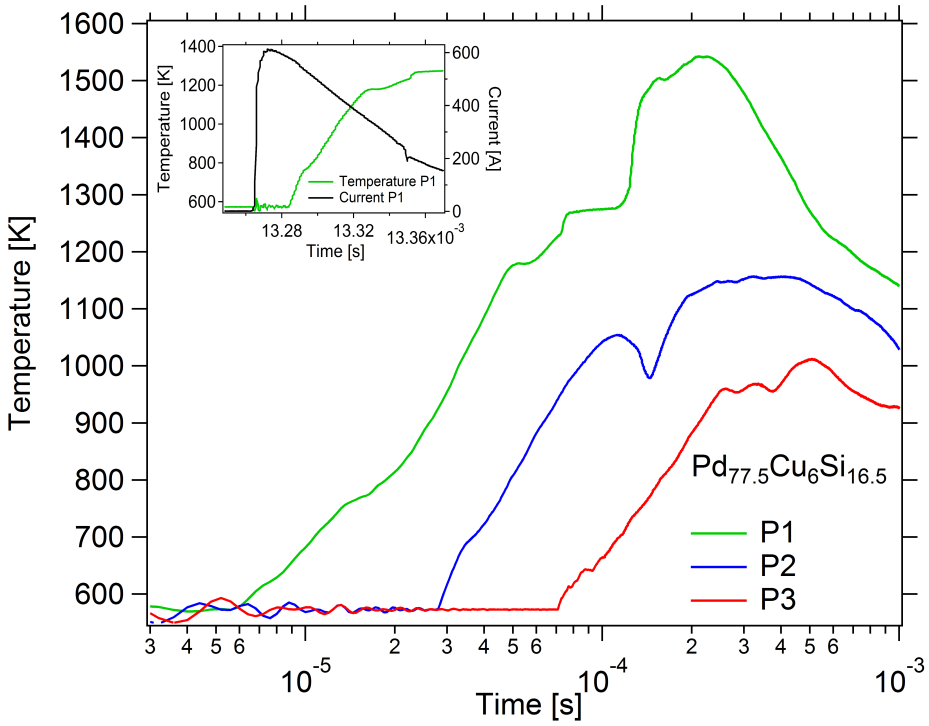

Figure 4.47: Temperature versus time curve during very fast heating experiments of three $Pd_{77.5}Cu_6Si_{16.5}$ samples that bypasses the crystallization nose.

at 1054 K after $1.1 \cdot 10^{-4}$ and at 1180 K after $5.2 \cdot 10^{-5}$. The inset of Fig. 4.47 shows the current and the temperature versus time of sample P1 and it verifies that the plateau in the temperature versus time curve at 1180 K is not related to the breaking of the sample since there is still current flowing.

Chapter 5

Discussion

5.1 Verification of the homogeneously dispersed amorphous structure

The broad diffraction maxima in the intensity of the X-ray diffraction measurements verifies the amorphous structure. We confirmed that every sample which we used during rapid heating measurements at the synchrotron beamline originally exhibited an amorphous structure prior to the measurements as it is shown in the exemplary graph in Fig. 4.1. For all ribbons which we used for measurements in the laboratory in Goettingen we tested a significant amount of samples in X-ray measurements with Siemens D8 difractometer and confirmed their amorphous nature. The verification of the amorphous structure is fundamental for our analysis. Please note that the expression "amorphous structure" in this work does not mean an entirely random structure where any structural order is completely absent. Greer et al. [1] emphasize that with common preparation techniques for metallic glasses nucleation cannot entirely inhibited during quenching and an amount of about 10^6 quenched-in nuclei usually remains in the amorphous solid. Such a small fraction in comparison to the total amount of atoms, for instance in our samples used for rapid heating experiments of 10^{23}, is not detectable during X-ray measurements. In section 5.6, we discuss whether or not such an estimated amount of quenched-in nuclei has an influence on the crystallization behavior.
Furthermore, different groups [20, 17] found various sorts polyhedron clusters as for instance quasicrystalline icosahedral clusters in CuZr. Lad et al. [20] claim that the third broad amorphous maximum in the X-ray diffraction pattern which occurs as a shoulder of the second maximum is an indication for such icosahedral clusters in the CuZr system. We also observe the third amorphous maximum partly merged with the second one. Despite this feature and the quenched-in nuclei, we identify the structure to be amorphous as long as there are no crystalline

peaks visible and there are clearly broad diffraction maxima visible which decay in intensity with increasing q-values and therefore the vast majority of the system does not exhibit a long range order but only average nearest neighbor distances.

5.2 Differential Scanning calorimetry measurements

In the calorimetry measurements performed in the DSC 7 from room temperature until 823 K we observed a polymorphous crystallization process of $Zr_{65}Cu_{27.5}Al_{7.5}$ in two clearly seperated steps at a heating rate of 10 K/min. Both crystallization events shift with increasing heating rate to higher temperatures. Apparently, the first crystallization process shifts faster with heating rate and thus the two crystallization processes merge at a heating rate of 200 K/min. Murty et al. [71] observed that $Zr_{65}Cu_{27.5}Al_{7.5}$ primarily devitrifies in an icosahedral quasicrystalline phase which causes the first exothermic peak in the DSC scan. At higher temperatures this metastable phase transforms into a stable Zr_2(Cu,Al) phase accommodated by the second exothermic peak. The system only crystallizes in the quasicrystalline phase when there is a sufficient amount of oxygen ($\geq$ 0.43 at%) dispersed in the system. Otherwise the system directly crystallizes in the stable Zr_2(Cu,Al) phase. Therefore, we expect to have a certain amount oxygen in our samples which is larger than 0.43 at%. We cannot exactly determine this amount because energy dispersive X-ray diffraction is not very sensitive to oxygen and the amount of oxygen is not proportional to, for instance, the enthalpy associated with the crystallization into the quasicrystalline phase. The first exothermic peak in our measurements is more pronounced in comparison to the first peak in the work of Murty [71] which is not directly related to a higher oxygen content. In our work the two exothermic crystallization peaks merge at a heating rate of 200 K/min while in literature it is observed to merge already at a rate of 40 K/min. This difference is probably related to a different oxygen content. The reason for oxygen in the system is most likely the high casting temperature which the alloy reached before it was quenched. Ribbons with the same composition which were not heated to such high temperatures during the preparation procedure exhibit only a one-step crystallization event, which is related to a low oxygen content (see Appendix C). This is similar to the behavior of an alloy with 0.14 at% in the work of Murty et al. [71].
We analyzed the shift of the glass transition temperature as a function of heating rate for five different compositions in the DSC (see Fig. 4.3). The trend can be well described using the Vogel-Fulcher-Tamman (VFT) equation. We will not discuss the obtained fitting parameters any further because the trend of some of the curves, particularly $Pd_{77.5}Cu_6Si_{16.5}$ and $Zr_{65}Cu_{27.5}Al_{7.5}$, may also be described with an exponential fit and therefore, the fitting pa-

rameters of the VFT fit are not very accurate. This coincidence that some curves can also be described with a linear fit might be attributed to two reasons. The first reason could be due to the small range of heating rates we analyzed in DSC measurements that the actual curvature is smaller than the fluctuations of the curve. The second reason could be that the curvature which can be described with the VFT law is naturally very small far away from the critical heating rate ϕ_c. However, Brüning et al. [33] could show that the VFT law indeed describes the trend of the data better than a linear dependence. This implies a lower limit for the glass transition temperature and a divergence of the glass transition temperature at a critical heating rate. The lower limit of the glass transition temperature is related to the prediction of the VFT fit that the α-relaxation time also goes to infinity at finite temperatures below the glass transition temperature [29].

5.3 Specific heat capacity measurements during ultrafast heating

In this part of the work, we determined the specific heat capacity in several different ways. Particularly, we calculated the specific heat capacity during ultrafast heating for the first time by additional capacitor discharges and continuously during the primary capacitor discharge. Therefore, it is necessary to compare our calculated data for the specific heat capacity with the the established method of the differential scanning calorimeter (DSC). In the exemplary case of $Pd_{77.5}Cu_6Si_{16.5}$, the absolute values of the specific heat determined during the primary capacitor discharge and the specific heat calculated by additional discharges match well in the solid glass state and in the supercooled liquid state (Fig. 5.1). For a comparison of the two data sets with the DSC curve, the specific heat curve obtained by DSC measurements with a heating rate of 2.5 K/s has been shifted. It shifted in the way that the specific heat values below the glass transition correspond approximately to the values from the specific heat determined by the continuous method. The reason for this is that the absolute values of the specific heat from the Perkin Elmer DSC 7 are subject to errors because they are sensitive to parameters which are difficult to control, like for instance the thermal coupling of the sample to the heater or fluctuations in the pressure between two measurements (i.e. the baseline measurement and the actual specific heat measurement). However, the specific heat differences within one measurement are not very affected from the aforementioned influences. Therefore, we can compare the specific heat jump at the glass transition temperature between the three techniques.

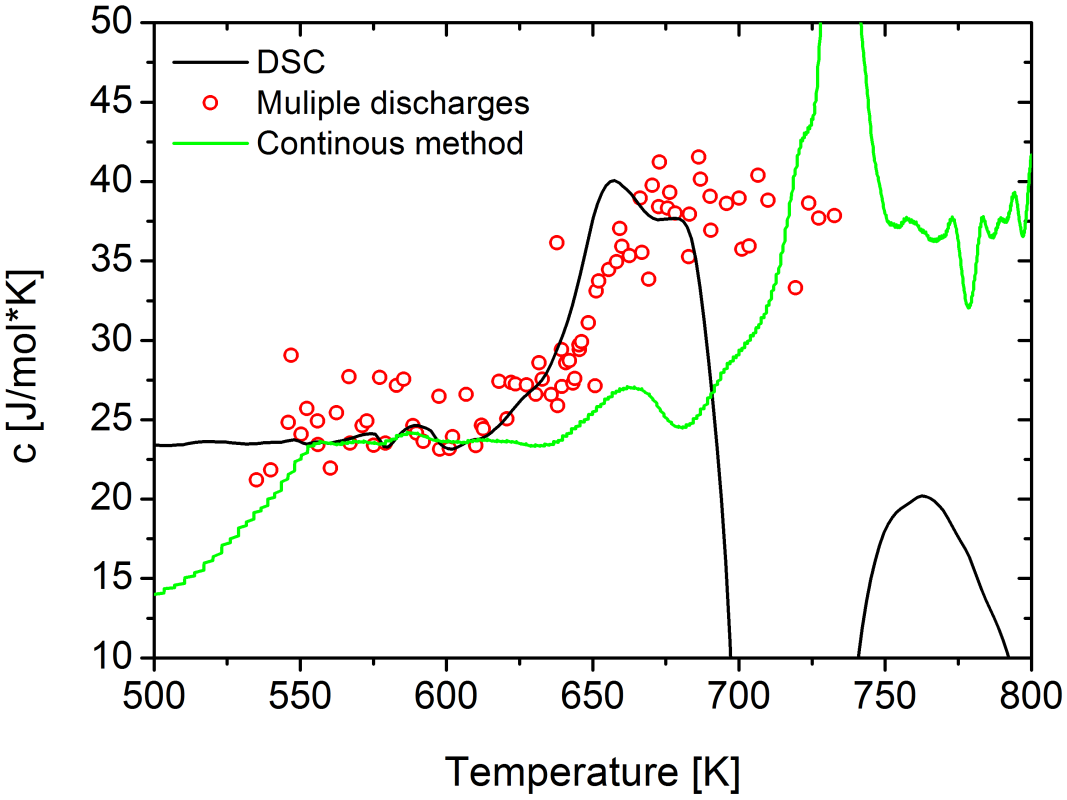

Figure 5.1: Comparison between the specific heat capacity data measured with the DSC (black curve), the one determined by additional discharges (red circles) and the specific heat calculated during the primary capacitor discharge (green curve).

The difference between the specific heat in the glassy state and the specific heat in the supercooled liquid state is 12.69 J/mol·K, 14.61 J/mol·K and 13.31 J/mol·K for the method with the multiple discharges, the continuous method and the DSC method with a heating rate of 2.5 K/s, respectively. The mean value of the differences in the specific heat at the glass transition temperature of all evaluated heating rates in the DSC measurements (0.167 K/s, 0.333 K/s, 0.667 K/s, 1.333 K/s, 2.5 K/s, 3.333 K/s) for the composition $Pd_{77.5}Cu_6Si_{16.5}$ is $\overline{\Delta c_P} = 18.72 \pm 1.65$ J/mol·K. The values obtained with the continuous method and with the multiple discharges are not within the error range of the average. However, as mentioned in section 2.2.2, in general considerations among several compositions there is an average increase in the specific capacity at the glass transition of 13.69±2.05 J/mol·K [36]. The specific heat difference obtained by multiple discharges with only one sample (12.69 J/mol·K), the specific heat difference from the continuous method of $Pd_{77.5}Cu_6Si_{16.5}$ (14.61 J/mol·K) as well as the mean value of $Zr_{65}Cu_{27.5}Al_{7.5}$ (13.93 J/mol·K) are in the range of the expected value. In

the measurement of the multiple discharges where we used several samples we obtained a specific heat difference of 15.84 J/mol·K which is slightly above the error range of the average value from literature. Also the value of the specific heat capacity difference from the "first approach" $\Delta c_P = 19.36$ J/mol · K where we just evaluated the temperature increase after the first capacitor discharge an the heat required for the increase is too high. In this measurement, one factor which affects the Δc_P-value is the difference between the heating and cooling rate. The low cooling rate in comparison to the heating rate leads to a decrease in enthalpy. In the subsequent capacitor discharge, the high heating rate causes an enthalpy recovery. This effect can also be observed in capacitor discharge measurements where the specific heat capacity was determined with the continuous method (green curve in Fig. 5.1). The specific heat capacity exhibits a pronounced overshoot over the supercooled liquid level at the glass transition temperature. In the same manner, aged glasses exhibit an enthalpy recovery which is also visible in a pronounced overshoot ([85, 3]). In this method of determining the specific heat capacity, one cannot definitely distinguish between the different factors which contribute to the Δc_P-value. Therefore, it is becomes evident that the "first approach" is a rather rough approach to the specific heat capacity.
As a consequence from the discussion in this section, we can conclude that both, the method using multiple discharges and the continuous method during the primary capacitor discharge, are suitable for the determination of specific heat values.

5.4 The change in glass transition temperature with heating rate

In this section, we discuss the glass transition temperature as a function of heating rate using three different techniques, namely, differential scanning calorimetry, intermediate heating using a power supply and ultrafast heating with a capacitor discharge. All together, they cover eight orders of magnitude in heating rates. In comparison, the absolute values of the glass transition temperature determined by the DSC and the intermediate heating technique match quite well in the range where both methods overlap (Fig. 5.2).

At low heating rates (< 2.5 K/s), our measurements confirm the results from Brüning et al. [33] that the increasing trend of the glass transition temperature with heating rate can be well described with the Vogel-Fulcher-Tammann (VFT) equation. When considering only the change in the glass transition with heating rate of the intermediate heating method between $10^1 - 10^5$ K/s, one can observe an almost linear increase on the semi logarithmic scale. However, in comparison with the other methods which all together cover a wider heating rate range, it

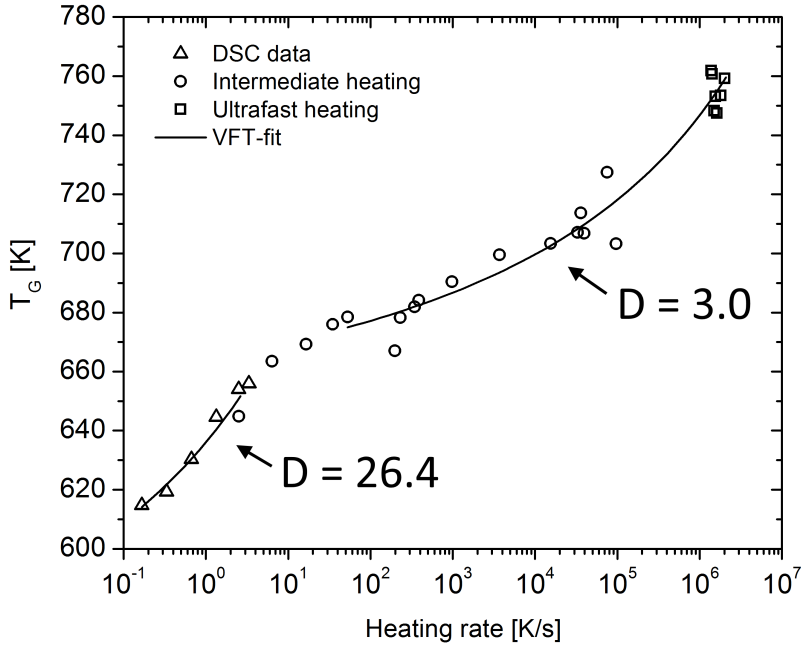

Figure 5.2: Glass transition temperature determined by DSC, intermediate heating and capacitor discharge technique versus the heating rate.

becomes evident that there is a certain curvature in the trend of the curve, too. This means that the shift in the glass transition temperature is not proportional to the logarithm of the heating rate in the high heating range either. In fact, the VFT equation is capable of describing the trend of the graph within a certain heating rate regime. We found that the increasing VFT trend from low heating rates cannot be extrapolated over the entire evaluated range and there is no single fit which can describe the shift of the glass transition temperature over the whole heating rate range. This includes the expected result, that the glass transition temperature does not diverge which was predicted from the VFT fit of the low heating rate regime ($10^{-1} - 10^{1}$ K/s). It seems that there are two regimes which both follow an independent VFT law and which are connected by a small transition regime. Particularly, the abrupt change in the trend at the end of the low heating rate VFT fit, which is found in the DSC measurements and confirmed with the intermediate heating technique, suggests that the process changes. It seems like we track two different glasses. One at low heating rates and a different one at high heating rates.
The fitting parameter of both VFT fits in Fig. 5.2 using equation 2.3 are shown in table 5.1.

When the VFT fit is applied to the alpha relaxation or the viscosity, the strength parameter D is closely related to the fragility m of the system by $D = 590/(m - 16)$ [28]. Rather strong

Parameter	Low heating rate regime	High heating rate regime
T_0 [K]	302 ± 612	589.31 ± 8.90
D	26.35 ± 151	2.96 ± 0.47
τ_0 [s/K]	$4.99 \cdot 10^{-11} \pm 2.22 \cdot 10^{-9}$	$1.57 \cdot 10^{-11} \pm 1.53 \cdot 10^{-11}$

Table 5.1: Fit parameter for the VFT Fit of $Zr_{65}Cu_{27.5}Al_{7.5}$ for the low and the high heating rate regime.

glass formers exhibit a high D-value (D≥10) while fragile systems show a small one (D<10) [28]. Since the VFT fit for the glass transition was derived from the Deborah number with the alpha relaxation time and the external frequency, it basically implies the parameters for the alpha relaxation time. Therefore, we can also relate the D-value obtained in this work to the fragility. It was previously observed that the system $Zr_{65}Cu_{27.5}Al_{7.5}$ has a fragility index of $m = 38.4$ [73]. According to the aforementioned equation, the fragility index results into a strength parameter of $D = 26.34$. This matches very nicely within the experimental error in the low heating rate. At high heating rates, the errors of the fitting parameters are much smaller. The strength parameter of $D = 2.96$ is significantly smaller than the low heating rate value. It corresponds to a fragility value of $m = 215$ which is even higher than the most fragile glass former poly vinyl chloride with a fragility at the glass transition of $m = 191$ [28].
The transition from the VFT behavior in the low heating rate range into the VFT behavior of high heating rates takes place at the transition from the DSC measurements to the intermediate heating measurements. In order to prove that the change in the trend of the glass transition increase is not an artifact of the change between the two techniques, we analyzed the crystallization behavior in the DSC measurements and the intermediate heating technique. It is visible, that the onset of crystallization increases logarithmically with heating rate in both techniques (Fig. 5.3). There is no change in the logarithmic increase at the transition between the two techniques. Consequently, we exclude any technical artifact which occurs when switching between the two techniques.

Because of this dramatic change in the fragility, we conclude that we observe a strong to fragile transition in $Zr_{65}Cu_{27.5}Al_{7.5}$ which takes place between the temperatures of 660 K and 680 K and between the heating rates of 2.5 K/s and 50 K/s.
In the supercooled liquid, the inverse proportionality between the translational and the rotational diffusion coefficients and the viscosity breaks down (Stokes-Einstein breakdown). This breakdown is expected to take place at a temperature around $1.2 \cdot T_G$ [16]. In our case it is unclear which glass transition temperature to use for the estimation. But even with the lowest glass transition temperature of $T_G = 615$ K for $Zr_{65}Cu_{27.5}Al_{7.5}$ found in this work at a heating rate of 0.167 K/s, we would expect the breakdown of the Stokes-Einstein relation to take place

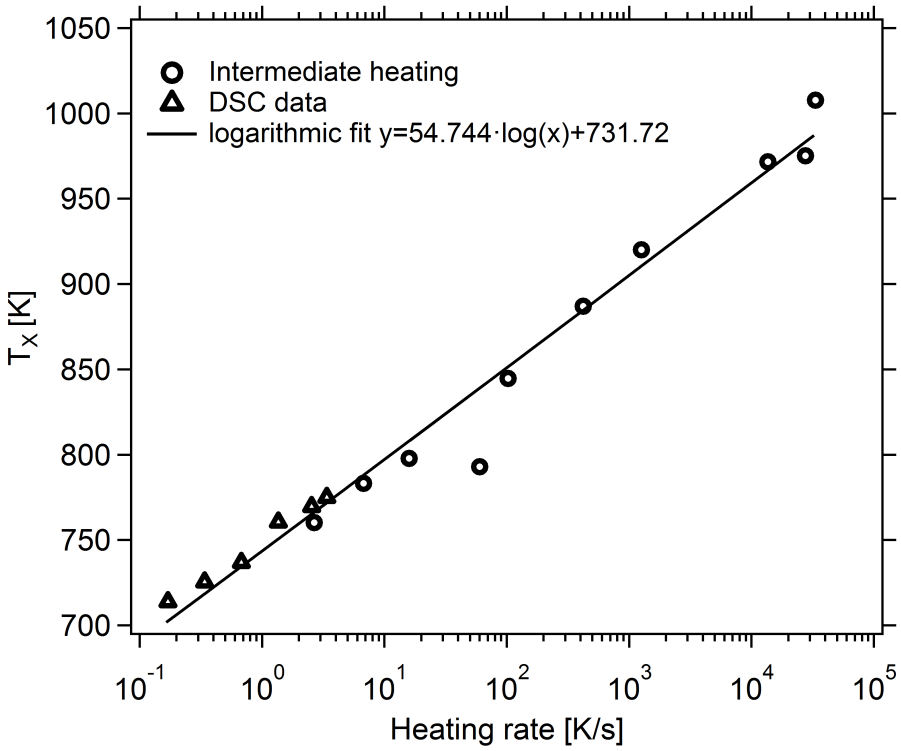

Figure 5.3: Onset of crystallization as a function of heating rate measured with DSC and intermediate heating technique.

at $T_{SE} = 738$ K. This value is higher than our transition between the two VFT trends around 670 K.

Additionally, in the supercooled liquid upon cooling a bifurcation between the α- and the β-process takes place. Rault estimated the α-, β-bifurcation to take place at around $1.3 \cdot T_G$ [43]. Hence, this process takes place at even higher temperatures than the breakdown of the Stokes-Einstein relation. In our measurements for $Zr_{65}Cu_{27.5}Al_{7.5}$, the α-, β-bifurcation is expected to take place around 800 K which is also significantly higher than the transition between the two VFT trends. In previous experiments, Hachenberg and coworkers estimated the α-, β-merging temperature, which is the same process as the α-, β-bifurcation. In this case, measured upon heating, the $Zr_{65}Cu_{27.5}Al_{7.5}$ system exhibits a merging at 870 ± 290 K [48]. This value is higher than the previous prediction of 800 K and beyond the maximum shift of the glass transition with heating rate obtained in this work.

In general, the VFT fit of the glass transition temperature predicts a lower limit T_0 of a possible shift of the glass transition temperature. This lower limit was previously identified with the Kauzmann temperature [33]. At the Kauzmann temperature, the configurational entropy of a supercooled liquid is equal to the one of the stable crystal. The phenomenon is controversially discussed in literature because a very slowly cooled crystal structure would reach a zero entropy

at $T = 0$ and a supercooled liquid with the same entropy as the stable crystal would reach a negative entropy upon further cooling [16]. This phenomenon is called "Kauzmann paradox" or "Entropy crisis". It is expected that the glass transition takes place at the Kauzmann temperature when a glass forming liquid is cooled down starting from the liquid state with extremely low cooling rates.
In our case, we obtain a lower limit of $T_0 = 302$ K which is very close to room temperature. This means that the metallic glass $Zr_{65}Cu_{27.5}Al_{7.5}$ is able to exhibit viscous flow on very long time scales close to room temperature. Unfortunately, the error of the VFT fit of the low heating rate regime is rather large and we did not test lower heating rates than 10^{-1} K/s as in the work of Brüning et al. [33]. Therefore, this work is not very suitable to give an accurate estimation of the lower limit of T_G.
Again, there are two regimes in the glass transition versus heating rate graph in Fig. 5.2 which both can be fitted using the VFT equation. So there is a second T_0 for $Zr_{65}Cu_{27.5}Al_{7.5}$ which is at $T_0 = 589$ K. Apparently, if the system would be able to maintain the state which it shows at higher heating rates also at lower heating rates, this T_0 might be the so called Kauzmann temperature. Since the system changes the heating rate dependence of the glass transition temperature at low heating rate to a "fragile" dependence, we expect that this temperature T_0 can be reached. An extrapolation of the low heating rate VFT behavior towards even lower temperatures yields that a heating rate of $1.9 \cdot 10^{-2}$ K/s would cause the glass transition temperature to be equal to the aforementioned T_0 of the high heating rate regime, i.e. $T_G = 589$ K.

Additionally, it is interesting to discuss whether or not there is an upper limit for the change in the glass transition temperature. Commonly used functions, like VFT, Arrhenius or Cohen-Crest to describe the temperature dependence of the alpha relaxation time, do not predict an upper limit for the glass transition temperature as a function of heating rate. However, it is shown here that there is not a single function which can describe the entire change of glass transition temperature with heating rate. Thus, it is likely that an extrapolated curve from low to high heating rates has only very limited validity. One possible reason that the glass transition temperature saturates and becomes independent on heating rate at very high heating rates is the occurrence of an equilibrium liquid-liquid phase transition at high temperatures in the supercooled as it was observed previously in a variety of systems [50, 86, 87, 52]. The transition at high temperatures in the supercooled liquid region observed in this work (see Fig. 4.46) exhibits a stronger heating rate dependence than the glass transition at the same heating rate, as discussed in the next chapter. Therefore, the transition described in the next chapter does not seem to merge with the glass transition temperature at very high heating rates.

5.5 Interpretation of T_0

In previous experiments, Yu et al. could show that it is possible to form ultrastable metallic glasses when a glass forming composition, in their case it is also $Zr_{65}Cu_{27.5}Al_{7.5}$, is sputtered on a substrate which is heated to a temperature close to T_G [88]. In general, ultrastable glasses were found in molecular glass formers and polymers and they were discovered to have remarkable thermodynamic and kinetic properties [89, 90]. Particularly, the glass transition of ultrastable glasses is shifted to significantly higher temperatures which cannot be obtained by long time annealing process. For the preparation it is important that the substrate is heated to temperatures which range from 0.7-0.8·T_G for metallic glasses, 0.75-0.85·T_G for molecular glasses and 0.8-0.9·T_G for polymers. The elevated substrate temperatures are very close to the expected Kauzmann temperature of the deposited glass forming system. This fact could also be confirmed by computer simulations [91].
In comparison to our measurements, the aforementioned substrate temperature intervals are also close to the Kauzmann temperature (previously called T_0) which we obtain from the VFT-fit of the high heating rate regime of 589 K. As discussed above, at the transition from the low heating rate regime to the high heating rate regime in our measurements, it seems as if we test different glass former in both regimes. In our case we found that the system exhibits a higher fragility at high heating rates. In DSC measurements from ultrastable glasses it could be observed that jump in the specific heat capacity at the glass transition is significantly larger in comparison to conventionally prepared glasses [90]. A large jump in the specific heat capacity at the glass transition is also a particular feature of fragile systems.
Additionally, we observe that the kinetic stability towards crystallization, measured by the temperature interval $\Delta T = T_X - T_G$ between the crystallization temperature T_X and the glass transition temperature T_G, is enhanced in the high heating rate regime in comparison to low heating rates (see Fig. 5.4). A general increase in ΔT with increasing heating rate is expected [22] (indicated by the dashed line in Fig. 5.4). But in the results here, it is visible that the glass transition temperature exhibits a milder increase with heating rate in the high heating rate regime in comparison to low heating rates while the increase in the crystallization temperature with heating rate remains unchanged. Consequently, ΔT increases stronger with heating rate above a rate of 7 K/s.
Contrary to the observation of ultrastable glasses, the measurements reported in this work indicate that the increase in the specific heat capacity at the glass transition is not larger for the capacitor discharge technique in comparison the measurement in the DSC (see section 5.3).
In order to test whether or not it is possible to create an ultrastable glass by "rapid annealing" we heated up a sample just above the glass transition temperature with a rate that corresponds

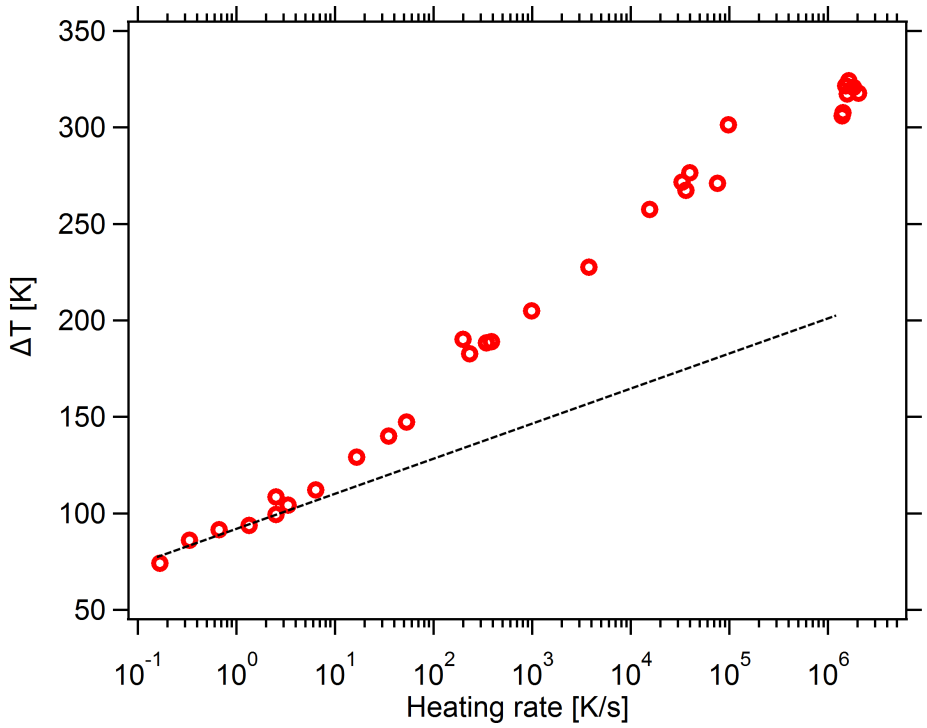

Figure 5.4: $\Delta T = T_X - T_G$ as a function of heating rate. The T_X-values result from the fit in Fig. 5.3. The dashed line is a logarithmic extrapolation from the low heating rate regime.

to the high heating rate regime (see Fig. 5.5a). Here, the sample was heated with an average rate of $2.36 \cdot 10^4$ K/s up to temperature of 748 K which is above the glass transition temperature of about 705 K. The amorphicity of the sample was again confirmed by X-ray diffraction measurements (graph not shown). Afterwards, the rapidly annealed sample was reheated in a DSC scan at 0.667 K/s. In comparison, with an as-cast ribbon there is no difference in the onset of the glass transition temperature (Fig. 5.5b). This means that the rapid annealing does let the sample relax to a significantly lower energy level and at least with this experiment it is not possible to capture the high heating rate state of the system.

5.6 Transition at high temperatures

In Fig. 4.46, we found a maximum in the specific heat capacity in those measurements where the sample has been heated up with such a high heating rate that it bypasses the crystallization nose. This maximum is a clear indication for an endothermal process within the liquid phase which is not correlated to any oxidation or crystallization process. In fact, a disordering of the amorphous structure is possible here as it takes place in a first order liquid-liquid phase transition.

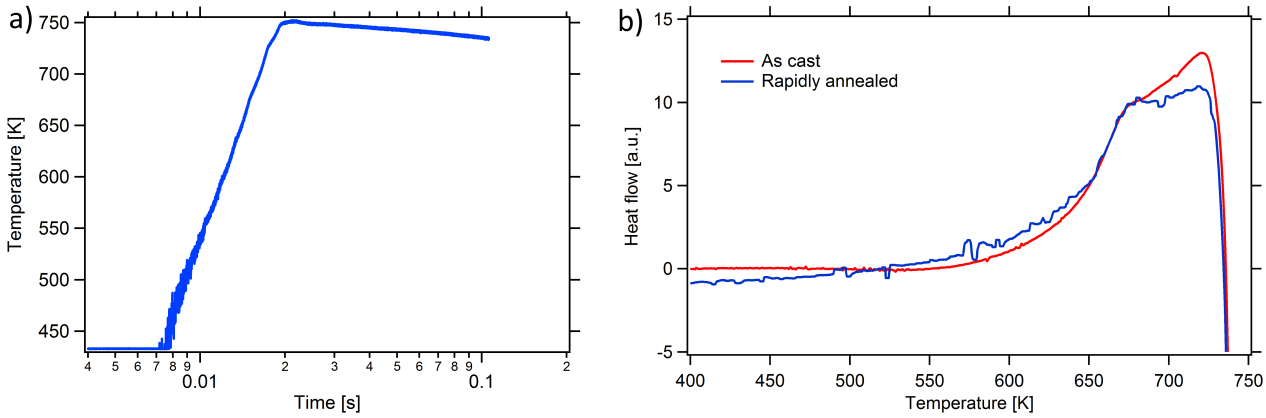

Figure 5.5: Comparison between a rapidly annealed sample and an as cast sample. a) Temperature versus time curve of the rapid annealing experiment. b) Two DSC scans with the same heating rate of an as-cast sample and an rapidly annealed sample.

The verification of a first order phase transition agrees with previous observations in MD-simulations by Lad et al. [20] In these simulations, a binary metallic glass of the composition $Cu_{55}Zr_{45}$ was quenched from the equilibrium liquid below its glass transition temperature. During quenching, the system exhibits a weak first order phase transition around 1130 K. This transition overlaps with a fragile to strong transition and is very close to the breakdown of the Stokes-Einstein-relation and the mode coupling temperature T_C. Despite the fact, that the composition is different to the one of our system, the value is fairly close to the value of the increase in the specific heat found in this work.

As observed in MD-simulations, the L-L-phase transition occurs at a temperature close to the mode coupling temperature T_C. In our case, if we assume the approximate relation $T_C = 1.4 \cdot T_G$ and a glass transition temperature of $T_G = 655$ K at a heating rate of 10 K/min, we obtain a value of $T_C = 917$ K for our system which is not in the close vicinity of our observed values at 1200 K for the lowest heating rate of $2.1 \cdot 10^6$ K/s at which the liquid-liquid phase transition occurs.

Most recently, Wei et al. showed an indication for a first order phase transition in the Zr-based glass former Vitreloy 1 due to hysteresis in volume and entropy [52]. This transition occurs above the melting temperature at 1100 K with an enthalpy around 1 kJ/mol·K. Despite the fact that it occurs in the liquid, this first order phase transition is closer to our reported heat capacity maximum at 1200 K.

The liquid-liquid phase transition found in this work exhibits a high value of the heat of fusion of about 8.0 kJ/mol which exceeds the enthalpy of crystallization for the stable Zr_2(Cu,Al)-phase of 2.5 kJ/mol [71] but is lower than the heat of fusion of the crystal structure of 12.8 kJ/mol [71]. Regarding the possibility that the process is related to the melting of quenched-in nuclei,

its enthalpy is about 60 % of the heat of fusion of the crystal. If such a crystalline fraction of the sample exists already at the beginning of the measurement, it would be visible in the X-ray diffraction patterns. For a verification that the scenario of crystallization during heating and subsequent melting of these crystals is unlikely, we calculated the crystallization rate by evaluating the crystallized volume fraction from the X-ray patterns (see section 4.38). Assuming the highest determined crystallization rate, there would be 3 % of the sample crystallized after 0.6 ms (time where the maximum in the temperature curves occurs). A melting of this crystallized volume fraction would not require more energy than it was stored in the sample by the capacitor discharge which still continues after about 1 ms. In fact, the temperature would still increase in the time interval between the maximum and the minimum in the temperature curve by 84 K. This means that it would not cause a temperature decrease but just a milder increase.

Another possible explanation for an endothermal maximum in the specific heat is the formation and subsequent melting of nanocrystals. Nanocrystals would not necessarily be visible in the X-ray patterns and might not have a distinct contribution to the temperature curve. Therefore, we calculated the electrical resistivity during heating from the current and the voltage measurement. The temperature coefficient of electrical resistance remains at a constant value of $6.7 \cdot 10^{-5}\Omega/\mathrm{K}$ between 900 K and 1250 K in case of sample Air 1 (see Fig. 4.43). During a crystallization process, the electrical resistance rather decreases since it is commonly higher in the amorphous than in the crystalline state. Additionally, if a large amount of nanocrystals would exist, nucleation would be inhibited and the crystallization process would be almost exclusively driven by the crystal growth of the nanocrystals. In comparison to the crystallization of amorphous metals, pure growth of nanocrystals exhibits only a decay in the enthalpy release rate, while amorphous metals show a distinct maximum during crystallization (see Fig. 2.10) [58]. The shape of the temperature curve during crystallization shows that the crystal starts from an amorphous alloy rather than from a nanocrystalline one. Consequently, the maximum in the temperature-versus-time curve of the samples which have been heated so fast that they bypass the crystallization nose (see Fig. 4.46 and Fig. 4.47) is not related to the melting of any crystalline structure.

Please note, that the samples Air 1, Air 2 and Air 3 reach a temperature of 1200 K within 0.6 ms, as shown in Fig. 4.40a. The composition $Zr_{65}Cu_{27.5}Al_{7.5}$ shows indeed a high tendency to oxidize [92]. In order to discard any influence of oxidation on the temperature curve of the measurements which bypass the crystallization nose, we heated up the samples termed Argon 1, Argon 2 and Argon 3 in a 970 mbar argon atmosphere. The chamber was previously evacuated to a pressure of $5.4 \cdot 10^{-5}$ mbar. These samples show the same behavior with pronounced maxima around 1200 K, 1450 K and 1400 K, respectively (see Fig. 4.45). Therefore, we are

sure that oxidation does not affect the trend of the temperature curves on this short timescale. As a consequence of all the arguments, we conclude that the decrease in the temperature curve is caused by a liquid-liquid phase transition of the amorphous structure to a liquid structure. Our measurements show that upon rapid heating the difference between the supercooled liquid and the high temperature liquid becomes evident and that this change between the two states is manifested in a first-order phase transition. For an overview of all transitions which

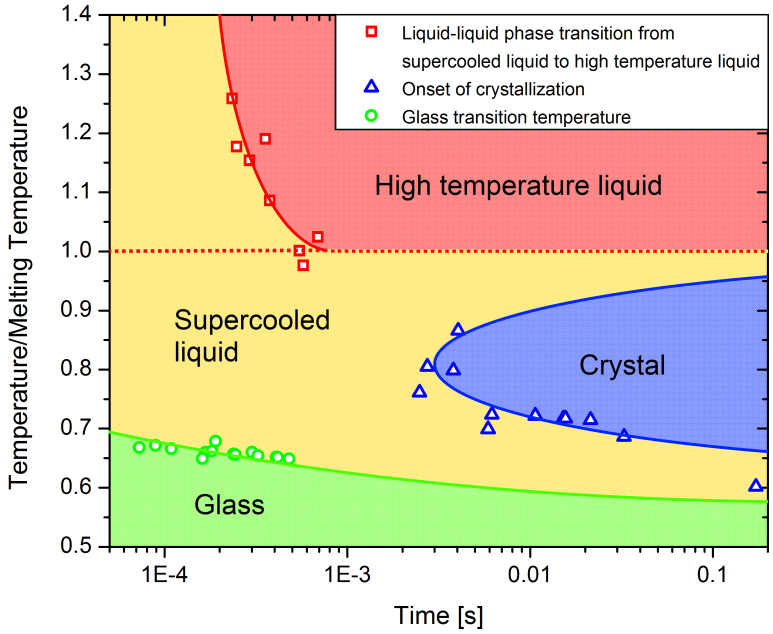

Figure 5.6: Compilation of all transitions observed in the $Zr_{65}Cu_{27.5}Al_{7.5}$ system with the exception of the crystal melting and oxidation. The y-axis is normalized by the melting temperature of the crystalline Zr_2(Cu,Al)-phase of 1230 K and the solid lines represent trendlines. Since there is no data for the liquid-liquid phase transition from the supercooled liquid to the high temperature liquid for times higher than the 10^{-3} s available, the trendline of our data points of the liquid-liquid transition ends in the melting temperature of the crystalline Zr_2(Cu,Al)-phase (red dotted line)

occur in our measurements and which are characteristic transitions of the metallic glass former $Zr_{65}Cu_{27.5}Al_{7.5}$, we plotted in Fig. 5.6 the points in the temperature-versus-time-curve where the liquid-liquid phase transitions occur (Fig. 4.46), the points where the second temperature increase due to crystallization sets in (Fig. 4.33) and the glass transition temperature for all the measurements in Fig. 4.33.

The data of the liquid-liquid phase transition obtained in this work may be connected with the melting temperature of the crystalline Zr_2(Cu,Al)-phase. In Fig. 5.6 it becomes evident, that

the liquid-liquid phase transition from the supercooled liquid in the high temperature liquid is strongly heating rate dependent. Please note that the transition from the supercooled liquid (marked in yellow in Fig. 5.6) to the crystal (marked in blue) is an exothermal process and the transition from the supercooled liquid to the high temperature liquid (marked in red) is an endothermal process.

Fig. 5.7 shows the same data as in Fig. 5.6 and, additionally, we plotted the crystallization

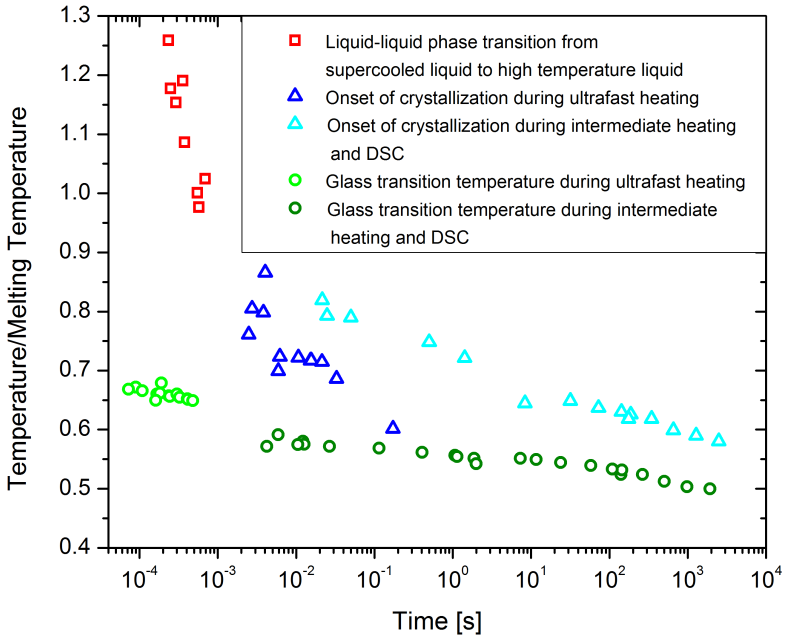

Figure 5.7: TTT diagram of $Zr_{65}Cu_{27.5}Al_{7.5}$ which includes the transition shown in Fig. 5.6 as well as the glass transition and crystallization onset during intermediate heating and the DSC measurements.

data from the intermediate heating measurements and the DSC measurements which is shown in Fig. 5.3. The temperature treatment is different in the intermediate heating measurements and in the DSC measurements in comparison to the ultrafast heating measurements during the capacitor discharge. The samples in the intermediate heating measurements were heated up with a constant rate while the samples which crystallize during the rapid heating measurements using the capacitor discharge technique have been heated rapidly to a certain temperature where the temperature remains constant until the sample crystallizes. As a consequence, the curves of the crystallization onsets in the temperature versus time curve of the intermediate heating technique and the ultrafast heating method do not connect. There is a systematic temperature difference between the two crystallization curves which, for instance, result in a temperature

difference of 128 K at $2.14 \cdot 10^{-2}$ K in the temperature versus time graph.
Fig. 5.7 shows the Fig. 5.8 shows the glass transition and the liquid-liquid transition in an

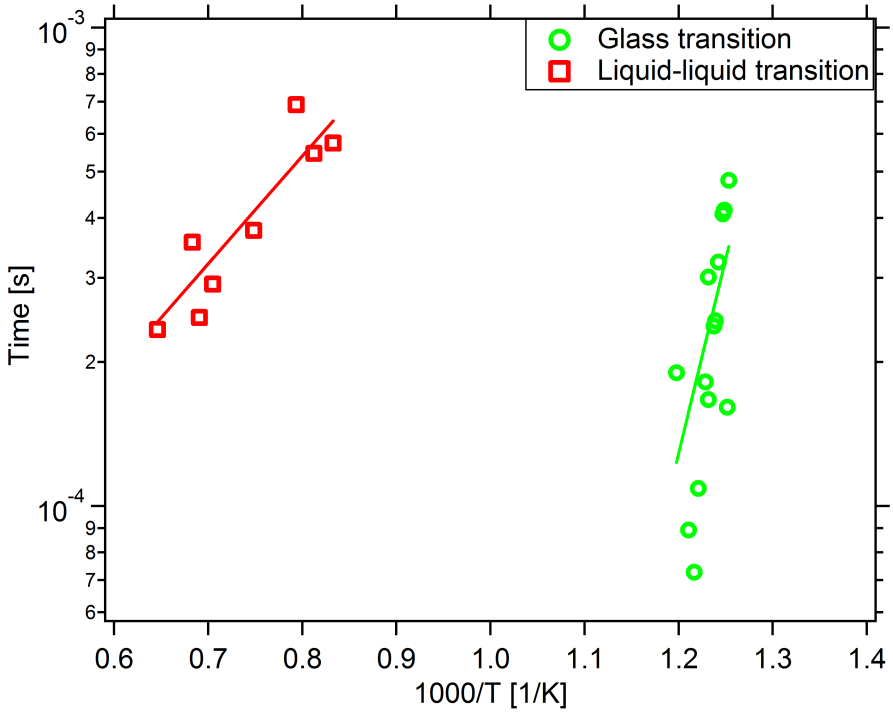

Figure 5.8: Arrhenius plot of the glass transition and the liquid-liquid transition.

Arrhenius plot. The time and the temperature data, both were taken from the data points in Fig. 5.6. Assuming the case that the crystallization could be somehow suppressed, it is interesting to ask whether or not the heating rate dependence of the liquid-liquid transition would continue to shift towards lower temperatures with decreasing heating rates. Therefore, the data points were fitted with an Arrhenius fit as shown in section 2.1. An extrapolation of both fits towards lower temperatures yields an intersection point at $T = 685$ K after $t = 1.64$ s (which corresponds to heating rate of $4.17 \cdot 10^4$ K/s). This point of the temperature and the heating rate is located on the curve of the high heating rate VFT fit in Fig. 5.2. It does not seem to correspond to a distinguished point the glass transition versus heating rate plot in Fig. 5.2. Additionally, in comparison to other decoupling phenomena which have been observed in the supercooled liquid this temperature is not close to any kinetic process observed in the supercooled liquid of $Zr_{65}Cu_{27.5}Al_{7.5}$.
In comparison, the trend of the liquid-liquid transition in Fig. 5.8 and also the position relative to the glass transition is very similar to the Debye-type relaxation process which was observed in the dielectric loss at higher temperatures in comparison to the glass transition in several alcohols [93]. The Debye process is expected to be related to the hydrogen bonds in alcohols and

it can be clearly distinguished from the α-process [93]. This was not observed in systems with van-der-Waals bonds [93]. Additionally, it takes place above the melting temperature, more precisely, at a fixed frequency it takes place at higher temperatures than the α-process and at a fixed temperature it is located at lower frequencies. There are two possibilities to prove, whether or not the liquid-liquid transition has a Debye-shape in, for example, the mechanical loss modulus. In the first way, the system could be excited using a sinusoidal mechanical excitation while increasing the temperature above the melting temperature of 1230 K, similar as is was performed in [74, 94] but to much higher temperatures. Or in the second way, the system could be hold at an elevated temperature close to the glass transition while it is excited with a much lower frequency than the frequency where the α-process occurs. In both ways, there are a range of technical circumstances which need to be solved first, like, for instance, a dynamic mechanical testing device which capable of testing at high temperatures in the first way and the technical resolution, crystallization and oxidation in the second way.
For comparison, we also heated up the more fragile glass former $Pd_{77.5}Cu_6Si_{16.5}$ with very high heating rates in order to bypass the crystallization nose (see Fig. 4.47). Unfortunately, there are only three measurements which were successfully heated to temperatures around the melting temperature of 1118 K. Similar to the measurements of the Zr-based alloy, the temperature versus time curves of the three alloys exhibit a maximum. In two of the three measurements, the maximum or plateau is below the crystalline melting temperature while the temperature of the plateau of the sample heated with the highest heating rate exceeds the melting temperature. There is also a considerable heating rate dependence: After heating with the highest average heating rate of $1.71 \cdot 10^7$ K/s the plateau occurs at 1180 K which is 220 K higher than in the measurement where the sample was heated with a rate of $2.58 \cdot 10^6$ K/s. The observation of the maximum in the temperature versus time curve in this Pd-based glass former suggests that this is a rather general process which is not an effect of a single composition or only in strong glass formers. However in the case for $Pd_{77.5}Cu_6Si_{16.5}$ there are certainly more measurements required in order to make an exact statement.

5.7 Crystallization of $Zr_{65}Cu_{27.5}Al_{7.5}$

At low temperatures, the $Zr_{65}Cu_{27.5}Al_{7.5}$ metallic glass crystallizes first in the Zr_2(Cu,Al)-phase. The duration of this intermittent phase decreases with increasing crystallization temperature and eventually vanishes at high temperatures (Fig. 4.23, Fig. 4.20 and Fig. 4.33a). The duration of this temperature increase matches well with the duration of the Zr_2(Cu,Al)-phase formation (Fig. 4.33b).
At high temperatures, $Zr_{65}Cu_{27.5}Al_{7.5}$ exhibits then a transition from the Zr_2(Cu,Al)-phase to

the ZrO_2-phase. In order to prove that this transition is responsible for the third increase of the temperature-versus-time curve in Fig. 4.33a which occurs above 1300 K, we heated up metallic glass samples of the same composition in an argon atmosphere. In these measurements, the third increase of the temperature-vs-time curve, as observed in Fig. 4.33a, does not occur anymore. Hence, we conclude that the transition from the Zr_2(Cu,Al)-phase to the ZrO_2-phase is an artifact of the air atmosphere during the measurements at the synchrotron.
The analysis of the crystallization process shows that the crystallized volume fraction first increases and follows the expected JMA trend. At a certain point in each curve the increase suddenly stops and the crystallized volume fraction deviates from the JMA fit. At high crystallization temperatures, it is visible that the crystallized volume fraction decreases rapidly when it deviates from the fit. Consequently, the areas underneath the crystalline peaks which we use for the analysis do not increase anymore and instead decrease. This is clear indication that the crystallization process has stopped and a new process sets in. Taking the change of X-ray diffraction patterns with time, it is noticeable that the decrease in the crystalline peaks of the Zr_2(Cu,Al)-phase is not directly linked to the increase of the peaks which correspond to the ZrO_2-phase because first a diffuse region occurs. The diffuse region sets in at the end of the increase in the temperature curve which is around 1300 K. This temperature is above the melting temperature of Zr_2(Cu,Al) of 1189 K. Additionally, it seems that the temperature increases to higher values during the crystallization in air in comparison to the measurements in Argon which reach only around 1140 K. The temperature increase in Argon during crystallization shows the expected behavior that it almost reaches the eutectic melting point. However at this point it is not clear whether this temperature difference between the measurements in air and the measurements in argon is caused by an additional heat due to the oxidation process or it is just an artifact due to change in emissivity of the oxidized surface.

Chapter 6

Summary and outlook

6.1 Summary

In this work we set up a capacitor discharge technique which is capable to heat up metallic glass ribbons with heating rates in the order of $10^6 - 10^7$ K/s. The capacitor discharge technique was partially combined with a series of four additional capacitor discharges which can be discharged at high temperature after the primary capacitor discharge. The additional capacitor discharges lead to small temperature increases in order to determine the specific heat capacity at high temperatures, for instance, in the supercooled liquid region. Additionally to the determination of the specific heat capacity by multiple discharges, the specific capacity was obtained in a continuous method during the primary capacitor discharge. Apart from the analysis of the absolute values of the specific heat capacity in the glass state and in the supercooled liquid we evaluated the specific heat capacity increase at the glass transition temperature. This increase at the glass transition is determined by the multiple discharge technique and during the primary discharge match well with expectations from literature data.
In total, we measured 9 compositions with the focus on the strong glass former $Zr_{65}Cu_{27.5}Al_{7.5}$. In the specific heat capacity of $Zr_{65}Cu_{27.5}Al_{7.5}$ at high temperatures, we found a significant increase with increasing temperature. This increase is not related to the melting of crystalline structures or oxidation and consequently we assign it to a pronounced liquid-liquid phase transition from the supercooled liquid into the high temperature liquid. The rather fragile glass former $Pd_{77.5}Cu_6Si_{16.5}$ exhibits the same behavior as aforementioned Zr-based one.
At the synchrotron beamline P07 at DESY we performed in-situ high temporal resolution X-ray studies. For this purpose, we designed a chopper system which was able to enhance the temporal resolution of the flat panel detector at the beamline P07 from 66 ms by a factor of 13 up to 5 ms. In principle, this chopper system is able to increase the temporal resolution of any 2D flat panel detector. Additionally, we derived a general formalism in order to construct

a chopper system which could enhance the temporal resolution of any 2D X-ray detector by an even higher factor than 13. Using the chopper system, we could show that the increase in the specific heat capacity is related to structural change of system. Instead of crystallizing into the Zr_2(Cu,Al) phase when crossing the crystallization nose, the X-ray diffraction patterns of the glass former $Zr_{65}Cu_{27.5}Al_{7.5}$ exhibit a diffuse region in combination with the ZrO_2 phase. While the oxide phase is an artefact of the measurements in air, we assign the diffuse region to the high temperature liquid phase.

Additionally, we studied the change in the glass transition temperature of $Zr_{65}Cu_{27.5}Al_{7.5}$ as a function of heating rate. For this purpose we used differential scanning calorimetry, capacitor discharge measurements and an intermediate heating rate technique using a power supply which all together cover 8 orders of magnitude in heating rate. We found that the change of glass transition temperature exhibits two distinct regimes. In both regimes the trend can be described by an individual Vogel-Fulcher-Tammann law. We assign the change in the parameters between the two fits to a fragile to strong transition and the systems heated with the high heating rates exhibit some similarities with the recently discovered ultrastable glasses.

6.2 Outlook

The results of this work contributed to the understanding of the thermodynamics and kinetics of metallic glasses and supercooled liquids. In general, advances always rise new question. And some of the questions resulting from the progress of this work are formulated in this section.
We could show that the glass transition temperature of a Zr-based metallic glass as a function of heating rate does not follow a single VFT law but instead exhibits a strong to fragile transition. It would be interesting to verify and further characterize this transition for instance by viscosity measurements. Previous viscosity measurements of $Zr_{65}Cu_{27.5}Al_{7.5}$ were restricted to temperatures just above the glass transition temperature because of the incipient crystallization process. Therefore the fragile to strong transition was not observed earlier. Johnson et al. showed that the capacitor discharge technique combined with a deformation experiment is capable of determining the viscosity during ultrafast heating and therefore the viscosity can be studied in the entire supercooled liquid region.
In this context, it would be also interesting to extent the investigated heating rate regime in this work to higher and to lower heating rates in order to test whether or not strong glasses exhibit only a single fragile to strong transition or multiple.
Furthermore, a possible link between a glass heated in the high heating rate regime and ultrastable glasses is particularly interesting for applications. The quality of ultrastable glasses is very sensitive to the substrate temperature [88]. It is likely that there is a similar sensitivity on the temperature which is reached by fast heating during rapid annealing. Such a dependence would need to be investigated first. Yu et al. could also show that the shift of the glass transition temperature of an ultrastable glass is proportional to the fragility. Therefore, one would expect that the observed strong to fragile transition changes between different systems depending on the fragility.
Additionally, we showed that a Zr-based metallic glass exhibits a liquid-liquid phase transition during ultrafast heating when transforming from the supercooled liquid into the high temperature liquid. Apparently, the liquid-liquid transition has a universal character since we could also observe it in a Pd-based glass former. However, to make clear a statement regarding universality, studies of more compositions are required. Johnson et al. could successfully performed enthalpy studies during ultrafast heating. This is a promising way in order to obtain more information about this transition.
For the crystallization measurements it would be interesting to further quantify the difference in the TTT curves during cooling and heating. In this context, one could test whether or not the crystallization behavior or the change in the TTT nose between cooling and heating is linked to the liquid-liquid transition or to the strong to fragile transition.

It would be also helpful to have an extension to the ultrafast heating technique where the sample could also be quenched in order to freeze in different high temperature states. This would simplify the analysis because the different states could be investigated at room temperature.

Chapter 7

Acknowledgement

The entire work for this thesis took several years starting from the construction of the setup, over the design and performance of the experiments until the evaluation and the interpretation of the results. The completion of this work would not have been possible without the valuable contributions of the following people. I thank you very much for your help.

First and foremost I thank **Prof. Dr. Konrad Samwer** for the possibility to write my PhD thesis in his glass group in such an interesting and edge cutting project. Including the period of the diploma thesis, I enjoyed to work since 6 years under his kind and inspiring supervision. In all these years I learned to improve my ways of approaching a physical problem and the general work as a scientist.

I thank **Prof. Dr. Hans-Ulrich Krebs** that he was willing and interested to be the second advisor of my thesis and his friendly recommendations towards the end of my PhD period.

I thank **all members of my examination committee** for agreeing to evaluate my thesis.

I thank the **1st Physical Institute** and the **DFG** within the **SFB602** and the **CRC1073** for financial support.

I am very grateful to **Carsten Mahn**. Carsten substantially helped me in all technical questions. He made major contributions to the setups, the Labview programs and supported me with the design of the chopper. During our collective work, I did not only benefit and learned from his experience but it was also always a pleasure to work with him.

I also thank very much **Uta Filippich** and **Antje Krüger**. Particularly Uta invested a lot of time in the trial to improve the sample preparation parameters. In total, we prepared 47 glassy ribbons which did not make it all in this thesis.

I thank **Dennis Kohl** for the performance of the EDX measurements.

I thank the **central workshop** of the Physics Department for their great efforts regarding the construction of the chopper system. Due to the approaching beamtime, the staff of the workshop and, particularly, Christof Schmidt invested a lot of time even during vacations to successfully finish the chopper system on time.

I thank the **workshop of the 1st Physical Institute** for all the little and big things which they constructed quickly for my setups on short notice.

I thank **Katrin Gehrke** for her helpful assistance with DSC measurements and handling of gas bottles.

I thank the former and the current members of the glass group of the 1st Physical Institute **Dr. Dennis Bedorf**, **Dr. Moritz Schwabe**, **Dr. Hannes Wagner**, **Matthias Büchsenschütz-Göbler**, **Dr. Jon-Olaf Krisponeit**, **Dr. Yuansu Luo**, **Steffi Finkhäuser**, **Birte Riechers**, **Dr. Hai-Bin Yu**, **Prof. Dr. Bo Zhang**, **Sebastian Pitikaris**, **Prof. Dr. Walter Arnold**, **Dr. Robert Maass**, **Carlos Herrero-Gomez**, **Dr. Alexandra Lagogianni** for the active and fruitful discussions as well as for the nice time during and after work.

I am grateful to the summer students from the University of Cambridge **Goodwin Gibbins**, **Eleanor Brug** and **Joe Corkerton**. Goodwin, the first exchange student I supervised, was very excited about glasses and helped me with her intense studies, her efficient support during our synchrotron beamtime in September 2012 and with ordering and labeling all the samples before and after the beamtime. Eleanor had a lot of patience and endurance in trying a number of ways to perform the ultrafast heating measurements with Pd-based samples. And, finally, Joe helped me by performing many intermediate heating experiments which gave a good overview over different glass formers.

I thank **Jonas Rübsam** for sharing my excitement and interest in this project during his

Bachelor thesis.

I thank **Dr. Norbert Mattern** for his kind and helpful collaboration within the beamtime at the synchrotron and the discussion of the results.

I am grateful to the **staff at synchrotron beamline P07** at PETRA III at DESY in Hamburg and particularly our local advisor **Dr. Jozef Bednarcik**, the beamline engineer **Olof Gutowski** and **Dr. Uta Ruett** for their kind and very efficient assistance during the beamtime in April 2011 and September 2012.

I thank **Prof. Dr. Joe Turner** and **Prof. Dr. Ranko Richert** for their interest and discussion during their stay in Göttingen.

I thank **Prof. Dr. Austen Angell** for his interest in my work and his motivating words.

I thank all current and former **members of the 1st Physical Institute** for the friendly and helpful atmosphere during the working time and the nice spare time activities like, for instance, excursions, barbecue and watching football.

I am also very grateful to my parents **Rudi** and **Christa Küchemann** for all their understanding, support and, particularly, for giving Alan a great time when I could not do it myself.

I thank my son **Alan Küchemann** for making my spare time so multifarious and exciting with all his lively and loving ways of doing things.

I thank my wife **Karina Avila** for all the discussions and patience with me during my PhD. It is invaluable to be supported by a loving and understanding family during times where I was mainly not available. I genuinely thank you for your support.

Appendix A

Capacitor discharge circuits

Fig. A.1 shows the detailed discharge circuit with the main capacitor discharge. The letters A and B mark the relays. When relay A is switched on (upwards) and, at the same time, relay B is switched down, the capacitor is charging. For the discharge relay A switches downwards and therefore the power supply is disconnected to the discharge circuit. After a certain waiting time (in our case 30 s) which is sufficient to discharge the capacitor entirely, relay B shwitches upwards and is connected to two electrical resistances which assure that the capacitor is discharged. This is important in case the sample broke during the discharge and there is a remaining charge on the capacitor. Afterwards, it is save to exchange the sample.

The multiple discharge circuit in Fig. A.2 has four times the same circuit and the main capacitor discharge. The four additional capacitor are charged by the same power supply.

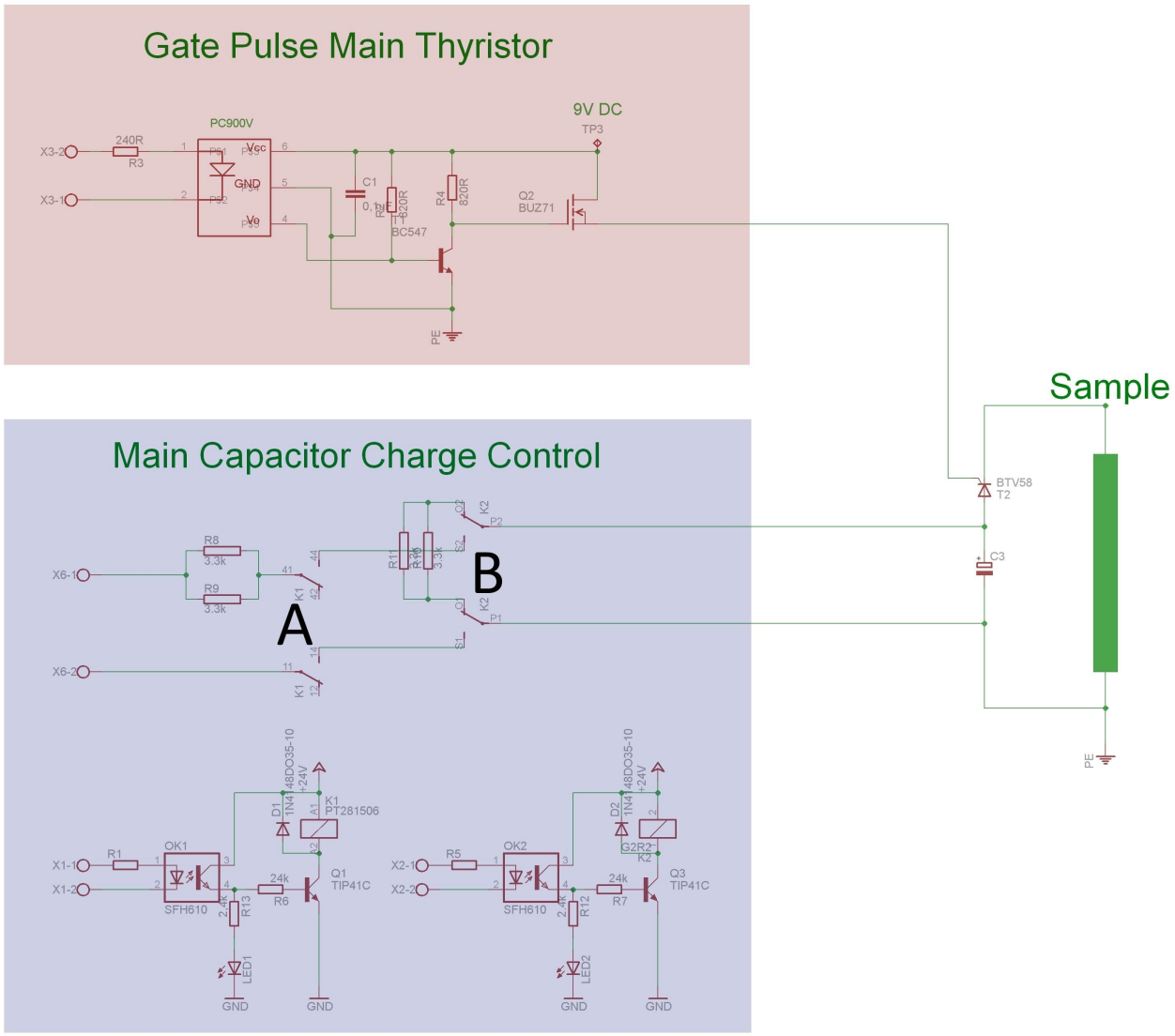

Figure A.1: Detailed capacitor discharge circuit of the main capacitor discharge

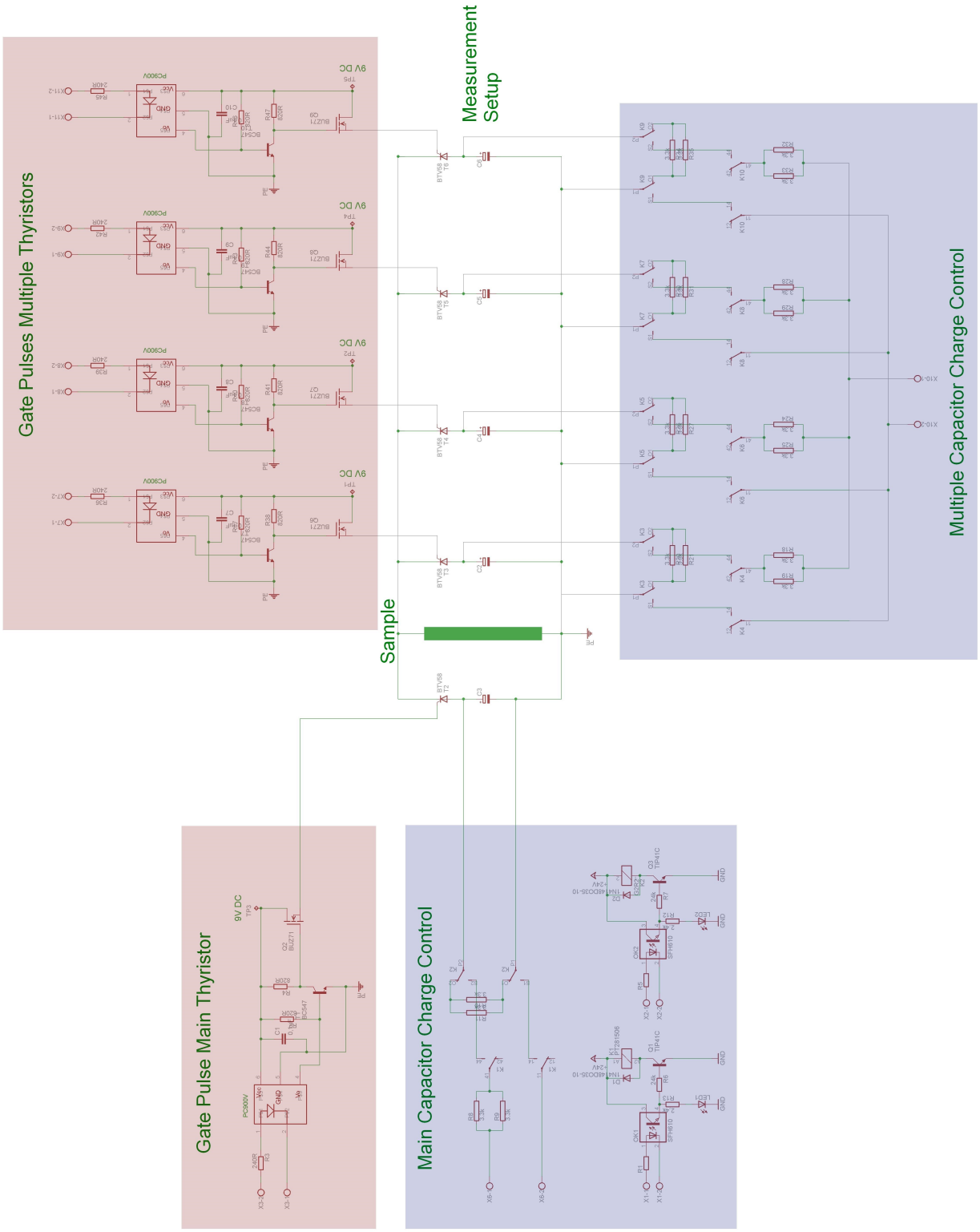

Figure A.2: Detailed capacitor discharge circuit of the main capacitor discharge and the four additional capacitor discharges.

Appendix B

Detailed analysis of composition

This chapter contains all the results from the EDX analysis. The average of each composition and brief description of the results is shown in section 4.2.

Element	nominal	1st	2nd	3rd	4th	5th	6th	∅
Zr [at%]	65.0	62.9	63.2	62.5	63.5	63.5	63.0	63.1 ± 0.1
Cu [at%]	27.5	29.4	28.9	30.1	28.2	28.8	29.0	29.1 ± 0.2
Al [at%]	7.5	7.7	7.9	7.4	8.3	7.7	8.0	7.8 ± 0.1

Table B.1: Composition of sample A

Element	nominal	1st	2nd	3rd	4th	5th	∅
Zr [at%]	65.0	64.5	64.1	64.5	63.8	62.9	64.0 ± 0.3
Cu [at%]	27.5	27.3	28.0	27.5	28.6	29.9	28.3 ± 0.4
Al [at%]	7.5	8.2	7.9	8.0	7.6	7.3	7.8 ± 0.1

Table B.2: Composition of sample B

Element	nominal	1st	2nd	3rd	4th	5th	6th	∅
Zr [at%]	45.0	43.9	43.5	43.7	43.2	42.1	43.9	43.4 ± 0.3
Cu [at%]	45.0	45.5	46.4	45.4	46.8	48.5	45.9	46.4 ± 0.5
Al [at%]	10.0	10.6	10.2	10.8	10.0	9.3	10.2	10.2 ± 0.2

Table B.3: Composition of sample C

Element	nominal	1st	2nd	3rd	4th	5th	6th	∅
Zr [at%]	66.5	65.1	64.3	65.4	65.5	66.4	66.1	65.5 ± 0.3
Cu [at%]	33.5	34.9	35.7	34.6	34.5	33.6	33.9	34.5 ± 0.3

Table B.4: Composition of sample D

Element	nominal	1st	2nd	3rd	4th	5th	6th	∅
Zr [at%]	66.5	63.7	63.6	63.2	63.1	62.1	63.4	63.2 ± 0.2
Cu [at%]	33.5	36.3	36.4	36.8	36.9	37.9	36.6	36.8 ± 0.2

Table B.5: Composition of sample E

Element	nominal	1st	2nd	3rd	4th	5th	6th	∅
Zr [at%]	65.0	64.7	63.9	63.8	63.6	63.5	63.5	63.8 ± 0.1
Cu [at%]	27.5	27.4	28.0	28.5	28.3	28.4	28.7	28.2 ± 0.2
Al [at%]	7.5	7.9	8.1	7.7	8.1	8.1	7.8	8.0 ± 0.1

Table B.6: Composition of sample F

Element	nominal	1st	2nd	3rd	4th	5th	6th	∅
Zr [at%]	45.0	44.1	43.5	43.7	44.8	43.7	44.2	44.0 ± 0.2
Cu [at%]	45.0	45.7	46.5	46.2	44.9	46.4	45.7	45.9 ± 0.2
Al [at%]	10.0	10.2	10.0	10.1	10.3	9.9	10.1	10.1 ± 0.1

Table B.7: Composition of sample G

Element	nominal	1st	2nd	3rd	4th	5th	6th	∅
Zr [at%]	66.5	64.7	65.5	65.1	66.3	67.1	66.8	65.9 ± 0.4
Cu [at%]	33.5	35.3	34.5	34.9	33.7	32.9	33.2	34.1 ± 0.4

Table B.8: Composition of sample H

Element	nominal	1st	2nd	3rd	4th	5th	6th	∅
Pd [at%]	77.5	78.6	78.6	79.5	78.4	79.3	79.6	79.0 ± 0.2
Cu [at%]	6.0	6.4	5.5	6.0	6.4	5.4	6.1	6.0 ± 0.2
Si [at%]	16.5	14.9	16.0	14.5	15.3	15.3	14.3	15.1 ± 0.3

Table B.9: Composition of sample I

Appendix C

Influence of the casting temperature on the crystallization behavior

Apparently, the temperature in the high temperature liquid from which the sample is quenched during the sample preparation has an influence on the crystallization behavior of the sample. This influence is briefly shown in this chapter with the four ribbons A (casting temperature[1]: T_{cast}=2173 K), B (T_{cast}=1423 K), F (T_{cast}=1473 K) and Z (T_{cast}=2173 K) of the nominal composition $Zr_{65}Cu_{27.5}Al_{7.5}$.

In the TTT diagram, the onsets of crystallization of the ribbon A and ribbon Z, here labeled with "group 1", are quite similar and the same is true for ribbon B and ribbon F, here labeled with "group 2"(see Fig. C.1). But there is a significant difference between the crystallization onsets of group 1 and group 2. At all temperatures, the crystallization onsets of group 2 occur at a later point in time. For instance, at 982 K the crystallization of group 2 starts about $2.8 \cdot 10^{-3}$ s after the start of the crystallization in group 1. At about $4.5 \cdot 10^{-3}$ s, there is a temperature difference of about 140 K between group 1 and group 2.

Fig. C.2 shows DSC measurements of ribbon A and ribbon F for six different rates. The aforementioned two step crystallization behavior presented in section 4.3 is shown in panel a). In contrast to this observation, ribbon F exhibits only a single crystallization event which is visible in Fig. C.2b. Consequently, there is also a significant difference in the crystallization at low heating rates additional to the previously described difference in crystallization behavior during ultrafast heating.

The other preparation parameters do not show a systematic influence on the crystallization behavior. Only the casting temperature seems to have a significant influence on the crystallization behavior. Another possible reason for such a change could be a deviation in the actual

[1]The casting temperature is the maximum temperature which is reached during the melt spinning procedure just before the alloy is quenched by squeezing it on the copper wheel.

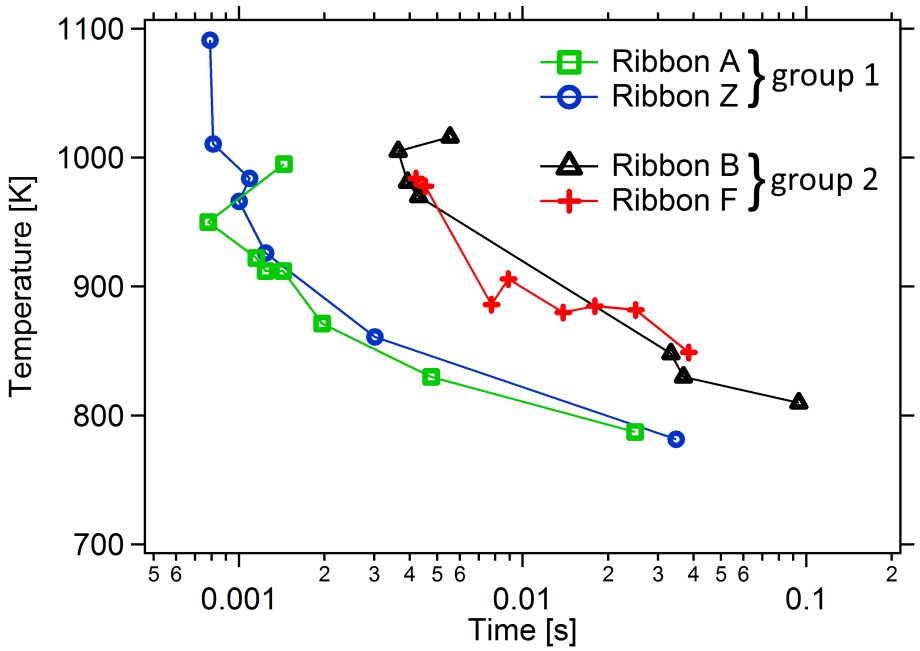

Figure C.1: TTT diagram of the crystallization onsets of ribbon A, B, F and Z.

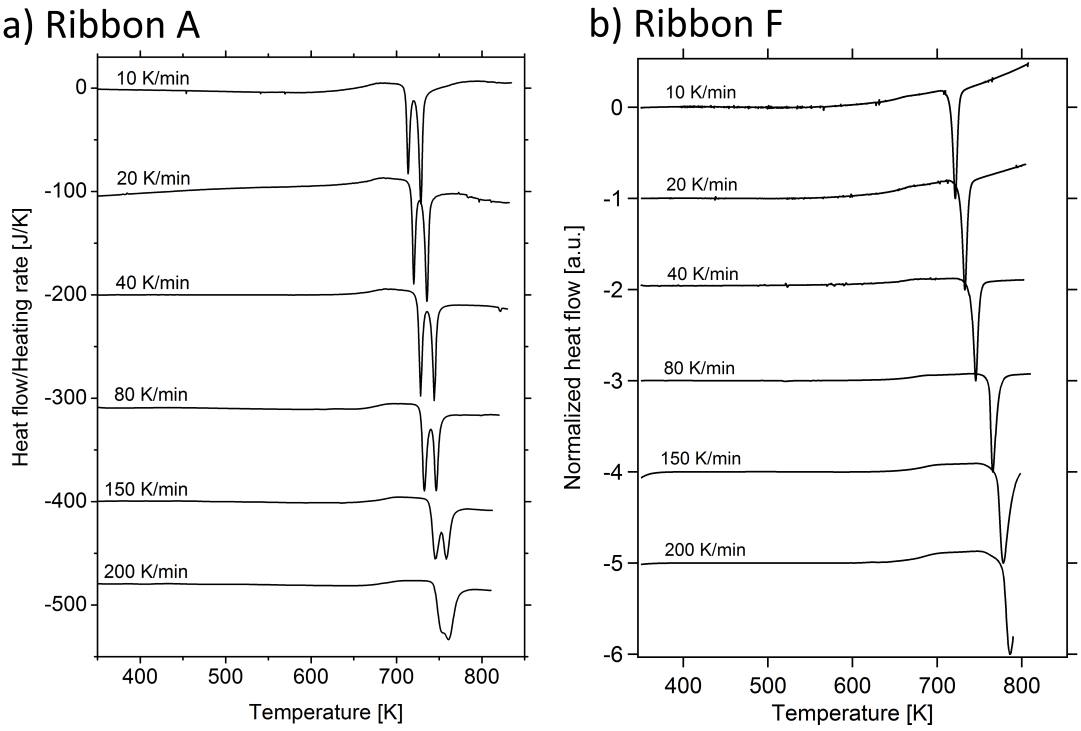

Figure C.2: DSC scans at six different heating rates 10 K/min, 20 K/min, 40 K/min, 80 K/min, 150 K/min and 200 K/min, shifted vertically for clarity. Panel a) shows measurements of ribbon A (copied from Fig. 4.2) and panel b) shows measurements of ribbon F.

composition among the ribbons. In fact, while the compositions of ribbon B and ribbon F deviate only by 0.2 at% at most, the Zr-content of ribbon A is 0.7 at% lower than the one of ribbon F. Additionally, the Cu-content of ribbon A is 0.8 at% higher than the one of ribbon B but the Al-content is the same of all three ribbons (see section 4.2 and Appendix B). However, since the crystallization behavior between ribbon B and ribbon F does not change despite 0.2 at% difference in Zr-content, we do not expect such a change in crystallization behavior when the Zr-content changes by 0.7 at%. Nevertheless, at this point, we cannot rule out completely that the little difference of the Zr- or Cu-content is responsible for the different crystallization behaviors. But it is more likely that the big difference in the casting temperature causes the change in the crystallization behavior.

Bibliography

[1] Ken Kelton and Alan Lindsay Greer. *Nucleation in condensed matter: applications in materials and biology*, volume 15. Elsevier, 2010.

[2] David Turnbull. Kinetics of Solidification of Supercooled Liquid Mercury Droplets. *The Journal of Chemical Physics*, 20(3):411, 1952.

[3] Jerzy Zarzycki. *Glasses and the vitreous state*. Number 9. Cambridge University Press, 1991.

[4] KL Ngai. *Relaxation and diffusion in complex systems*. Springer, 2011.

[5] W Buckel and R Hilsch. Einfluß der kondensation bei tiefen temperaturen auf den elektrischen widerstand und die supraleitung für verschiedene metalle. *Zeitschrift fuer Physik*, 138(2):109–120, 1954.

[6] Werner Buckel. Elektronenbeugungs-aufnahmen von dünnen metallschichten bei tiefen temperaturen. *Zeitschrift für Physik*, 138(2):136–150, 1954.

[7] W Klement, RH Willens, and POL Duwez. Non-crystalline structure in solidified gold–silicon alloys. *Nature*, (187):867–870, 1960.

[8] Gerold Adam and Julian H Gibbs. On the temperature dependence of cooperative relaxation properties in glass-forming liquids. *The journal of chemical physics*, 43(1):139–146, 1965.

[9] Morrel H Cohen and David Turnbull. Molecular transport in liquids and glasses. *The Journal of Chemical Physics*, 31(5):1164–1169, 1959.

[10] David Turnbull and Morrel H Cohen. Free-volume model of the amorphous phase: glass transition. *The Journal of Chemical Physics*, 34(1):120–125, 1961.

[11] Wolfgang Götze. Recent tests of the mode-coupling theory for glassy dynamics. *Journal of Physics: condensed matter*, 11(10A):A1, 1999.

[12] KL Ngai. Relation between some secondary relaxations and the α relaxations in glass-forming materials according to the coupling model. *The Journal of chemical physics*, 109(16):6982–6994, 1998.

[13] C Austen Angell. Formation of glasses from liquids and biopolymers. *Science*, 267(5206):1924–1935, 1995.

[14] E Rössler. Indications for a change of diffusion mechanism in supercooled liquids. *Physical review letters*, 65(13):1595–1598, September 1990.

[15] Marcus T. Cicerone, F. R. Blackburn, and M. D. Ediger. How do molecules move near Tg? Molecular rotation of six probes in o-terphenyl across 14 decades in time. *The Journal of Chemical Physics*, 102(1):471, 1995.

[16] P G Debenedetti and F H Stillinger. Supercooled liquids and the glass transition. *Nature*, 410(6825):259–67, March 2001.

[17] YQ Cheng, HW Sheng, and E Ma. Relationship between structure, dynamics, and mechanical properties in metallic glass-forming alloys. *Physical Review B*, 78(1):014207, 2008.

[18] Ch E Lekka, A Ibenskas, AR Yavari, and GA Evangelakis. Tensile deformation accommodation in microscopic metallic glasses via subnanocluster reconstructions. *Applied Physics Letters*, 91(21):214103, 2007.

[19] AE Lagogianni, G Almyras, Ch E Lekka, DG Papageorgiou, and GA Evangelakis. Structural characteristics of cu x zr 100- x metallic glasses by molecular dynamics simulations. *Journal of Alloys and Compounds*, 483(1):658–661, 2009.

[20] K N Lad, N Jakse, and a Pasturel. Signatures of fragile-to-strong transition in a binary metallic glass-forming liquid. *The Journal of chemical physics*, 136(10):104509, March 2012.

[21] J Orava, a L Greer, B Gholipour, D W Hewak, and C E Smith. Characterization of supercooled liquid Ge2Sb2Te5 and its crystallization by ultrafast-heating calorimetry. *Nature materials*, 11(4):279–83, April 2012.

[22] William L Johnson, Georg Kaltenboeck, Marios D Demetriou, Joseph P Schramm, Xiao Liu, Konrad Samwer, C Paul Kim, and Douglas C Hofmann. Beating crystallization in glass-forming metals by millisecond heating and processing. *Science (New York, N.Y.)*, 332(6031):828–33, May 2011.

[23] T. Egami. Atomic level stresses. *Progress in Materials Science*, 56(6):637–653, August 2011.

[24] JOHN D Eshelby. The determination of the elastic field of an ellipsoidal inclusion, and related problems. *Proceedings of the Royal Society of London. Series A. Mathematical and Physical Sciences*, 241(1226):376–396, 1957.

[25] M. Reiner. The Deborah Number. *Physics Today*, 17(1):62, 1964.

[26] Morrel H Cohen and G_ S Grest. Liquid-glass transition, a free-volume approach. *Physical Review B*, 20(3):1077, 1979.

[27] Wei-Hua Wang, Chuang Dong, and CH Shek. Bulk metallic glasses. *Materials Science and Engineering: R: Reports*, 44(2):45–89, 2004.

[28] Roland Böhmer, KL Ngai, CA Angell, and DJ Plazek. Nonexponential relaxations in strong and fragile glass formers. *The Journal of chemical physics*, 99(5):4201–4209, 1993.

[29] Pablo G Debenedetti. *Metastable liquids: concepts and principles*. Princeton University Press, 1996.

[30] Wolfgang Götze. *Complex Dynamics of Glass-Forming Liquids: A Mode-Coupling Theory: A Mode-Coupling Theory*, volume 143. Oxford University Press, 2008.

[31] S. R. Elliott. *Physics of amorphous materials*, volume 20. Longman Group Ltd., 1984.

[32] Cornelius T Moynihan, Allan J Easteal, James Wilder, and Joseph Tucker. Dependence of the glass transition temperature on heating and cooling rate. *The Journal of Physical Chemistry*, 78(26):2673–2677, 1974.

[33] R Brüning and K Samwer. Glass transition on long time scales. *Physical Review B*, 46(18):11318, 1992.

[34] Katharina Vollmayr, Walter Kob, and Kurt Binder. How do the properties of a glass depend on the cooling rate? a computer simulation study of a lennard-jones system. *The Journal of chemical physics*, 105(11):4714–4728, 1996.

[35] Paul K Dixon. Specific-heat spectroscopy and dielectric susceptibility measurements of salol at the glass transition. *Physical Review B*, 42(13):8179, 1990.

[36] HB Ke, P Wen, DQ Zhao, and WH Wang. Correlation between dynamic flow and thermodynamic glass transition in metallic glasses. *Applied Physics Letters*, 96(25):251902–251902, 2010.

[37] T Egami. Formation and deformation of metallic glasses: atomistic theory. *Intermetallics*, 14(8):882–887, 2006.

[38] Klaus Stierstadt, Wilhelm T Hering, and Thomas Dorfmüller. Mechanik, relativität, wärme, band 1 der reihe bergmann-schaefer: Lehrbuch der experimentalphysik. *Walther de Gruyter, Berlin-New York*, 1998.

[39] Walter Kob, Claudio Donati, Steven J Plimpton, Peter H Poole, and Sharon C Glotzer. Dynamical heterogeneities in a supercooled lennard-jones liquid. *Physical review letters*, 79(15):2827, 1997.

[40] Mi D Ediger. Spatially heterogeneous dynamics in supercooled liquids. *Annual review of physical chemistry*, 51(1):99–128, 2000.

[41] SA Reinsberg, XH Qiu, M Wilhelm, HW Spiess, and MD Ediger. Length scale of dynamic heterogeneity in supercooled glycerol near tg. *The Journal of Chemical Physics*, 114(17):7299–7302, 2001.

[42] Claudio Donati, Sharon C Glotzer, Peter H Poole, Walter Kob, and Steven J Plimpton. Spatial correlations of mobility and immobility in a glass-forming lennard-jones liquid. *Physical Review E*, 60(3):3107, 1999.

[43] Jacques Rault. Origin of the vogel–fulcher–tammann law in glass-forming materials: the α–β bifurcation. *Journal of non-crystalline solids*, 271(3):177–217, 2000.

[44] Gyan P Johari and Martin Goldstein. Viscous liquids and the glass transition. ii. secondary relaxations in glasses of rigid molecules. *The Journal of Chemical Physics*, 53(6):2372–2388, 1970.

[45] HR Schober. Soft phonons in glasses. *Physica A: Statistical Mechanics and its Applications*, 201(1):14–24, 1993.

[46] Daniel B Miracle, Takeshi Egami, Katharine M Flores, and Kenneth F Kelton. Structural aspects of metallic glasses. *MRS bulletin*, 32(08):629–634, 2007.

[47] I Chang, F Fujara, B Geil, G Heuberger, T Mangel, and H Sillescu. Translational and rotational molecular motion in supercooled liquids studied by nmr and forced rayleigh scattering. *Journal of non-crystalline solids*, 172:248–255, 1994.

[48] Jorg Hachenberg, Dennis Bedorf, Konrad Samwer, Ranko Richert, Annelen Kahl, Marios D Demetriou, and William L Johnson. Merging of the α and β relaxations and aging via

the johari–goldstein modes in rapidly quenched metallic glasses. *Applied Physics Letters*, 92(13):131911–131911, 2008.

[49] M Paluch, CM Roland, S Pawlus, J Zioło, and KL Ngai. Does the arrhenius temperature dependence of the johari-goldstein relaxation persist above t g? *Physical review letters*, 91(11):115701, 2003.

[50] Kaori Ito, Cornelius T Moynihan, and C Austen Angell. Thermodynamic determination of fragility in liquids and a fragile-to-strong liquid transition in water. *Nature*, 398(6727):492–495, 1999.

[51] John JZ Li, WK Rhim, CP Kim, K Samwer, and WL Johnson. Evidence for a liquid–liquid phase transition in metallic fluids observed by electrostatic levitation. *Acta Materialia*, 59(5):2166–2171, 2011.

[52] Shuai Wei, Fan Yang, Jozef Bednarcik, Ivan Kaban, Olga Shuleshova, Andreas Meyer, and Ralf Busch. Liquid–liquid transition in a strong bulk metallic glass-forming liquid. *Nature communications*, 4, 2013.

[53] YJ Kim, R Busch, WL Johnson, AJ Rulison, and WK Rhim. Experimental determination of a time–temperature-transformation diagram of the undercooled zr41. 2ti13. 8cu12. 5ni10. 0be22. 5 alloy using the containerless electrostatic levitation processing technique. *Applied physics letters*, 68(8):1057–1059, 1996.

[54] S Pogatscher, PJ Uggowitzer, and JF Löffler. In-situ probing of metallic glass formation and crystallization upon heating and cooling via fast differential scanning calorimetry. *Applied Physics Letters*, 104(25):251908, 2014.

[55] Urs Gasser, Eric R Weeks, Andrew Schofield, PN Pusey, and DA Weitz. Real-space imaging of nucleation and growth in colloidal crystallization. *Science*, 292(5515):258–262, 2001.

[56] MD Ediger, Peter Harrowell, and Lian Yu. Crystal growth kinetics exhibit a fragility-dependent decoupling from viscosity. *The Journal of chemical physics*, 128(3):034709, 2008.

[57] Jiří Málek. The applicability of johnson-mehl-avrami model in the thermal analysis of the crystallization kinetics of glasses. *Thermochimica Acta*, 267:61–73, 1995.

[58] LC Chen and F Spaepen. Calorimetric evidence for the micro-quasicrystalline structure of 'amorphous' al/transition metal alloys. *Nature*, 336(6197):366–368, 1988.

[59] P Riello, P Canton, and G Fagherazzi. Quantitative phase analysis in semicrystalline materials using the rietveld method. *Journal of applied crystallography*, 31(1):78–82, 1998.

[60] Jozef Bednarcik, Stefan Michalik, Vladimir Kolesar, Uta Rütt, and Hermann Franz. In situ xrd studies of nanocrystallization of fe-based metallic glass: a comparative study by reciprocal and direct space methods. *Physical Chemistry Chemical Physics*, 15(22):8470–8479, 2013.

[61] Stefan Küchemann and Konrad Samwer. Ultrafast heating of metallic glasses reveals disordering of the amorphous structure. in review, 2014.

[62] B Zhang, DQ Zhao, MX Pan, RJ Wang, and WH Wang. Formation of cerium-based bulk metallic glasses. *Acta materialia*, 54(11):3025–3032, 2006.

[63] SM Chathoth, B Damaschke, JP Embs, and K Samwer. Giant changes in atomic dynamics on microalloying metallic melt. *Applied Physics Letters*, 95(19):191907, 2009.

[64] Glenn R Garrett, Marios D Demetriou, Jason Chen, and William L Johnson. Effect of microalloying on the toughness of metallic glasses. *Applied Physics Letters*, 101(24):241913, 2012.

[65] Yossi Cohen, Smarajit Karmakar, Itamar Procaccia, and Konrad Samwer. The nature of the β-peak in the loss modulus of amorphous solids. *EPL (Europhysics Letters)*, 100(3):36003, 2012.

[66] Ratul Dasgupta, Pankaj Mishra, Itamar Procaccia, and Konrad Samwer. Micro-alloying and the toughness of glasses: Modeling with pinned particles. *Applied Physics Letters*, 102(19):191904, 2013.

[67] Qi An, Konrad Samwer, William A Goddard III, William L Johnson, Andres Jaramillo-Botero, Glenn Garret, and Marios D Demetriou. Predicted optimum composition for the glass-forming ability of bulk amorphous alloys: Application to cu–zr–al. *The Journal of Physical Chemistry Letters*, 3(21):3143–3148, 2012.

[68] Hannes Wagner, Dennis Bedorf, Stefan Küchemann, Moritz Schwabe, Bo Zhang, Walter Arnold, and Konrad Samwer. Local elastic properties of a metallic glass. *Nature materials*, 10(6):439–442, 2011.

[69] PJ Cote and LV Meisel. Electrical transport in glassy metals. In *Glassy Metals I*, pages 141–166. Springer, 1981.

[70] AH Cai, X Xiong, Y Liu, H Chen, WK An, XS Li, Y Zhou, and Y Luo. Estimation of kauzmann temperature and isenthalpic temperature of metallic glasses. *The European Physical Journal B-Condensed Matter and Complex Systems*, 64(2):147–151, 2008.

[71] BS Murty, DH Ping, K Hono, and A Inoue. Influence of oxygen on the crystallization behavior of $zr_{65}cu_{27.5}al_{7.5}$ and $zr_{66.7}cu_{33.3}$ metallic glasses. *Acta materialia*, 48(15):3985, 2000.

[72] Stefan Küchemann, Hannes Wagner, Moritz Schwabe, Dennis Bedorf, Walter Arnold, and Konrad Samwer. Stored mechanical work in inhomogeneous deformation processes of a pd-based bulk metallic glass. *Metallurgical and Materials Transactions A*, 45(5):2389–2392, 2014.

[73] Manfred Weiß. *Mechanische Eigenschaften und thermische Stabilität tief unterkühlter Metallschmelzen im Bereich der Glastemperatur*. Verlag Neue Wiss., 2000.

[74] Jörg Hachenberg. *Sekundäre Relaxationen in amorphen Festkörpern*. PhD thesis, Niedersächsische Staats-und Universitätsbibliothek Göttingen, 2006.

[75] Thaddeus B Massalski, Hiroaki Okamoto, PR Subramanian, Linda Kacprzak, et al. *Binary alloy phase diagrams*. ASM international, 1990.

[76] Delta Elektronika BV. High speed programming options for sm800, sm1500, sm3000 and sm6000. *Operation Manual*, 2010.

[77] Xiao Liu, Marios D Demetriou, Georg Kaltenboeck, Joseph P Schramm, Glenn R Garrett, and William L Johnson. Description of millisecond ohmic heating and forming of metallic glasses. *Acta Materialia*, 61(8):3060–3067, 2013.

[78] Perkin Elmer. Xrd 1621 n es series: 16-inch digital x-ray detectors. *Datasheet*, 2008.

[79] Clifford Bueno, Richard L. Rairden, and Robert A. Betz. Hybrid scintillators for x-ray imaging. *SPIE International Symposium Medical Imaging*, 1996.

[80] Paxscan and Varian medical systems. Flat panel x-ray imaging. *report from www.varian.com*, 2004.

[81] Stefan Küchemann, Carsten Mahn, and Konrad Samwer. Note: Significant increase to the temporal resolution of 2d x-ray detectors using a novel beam chopper system. *Review of Scientific Instruments*, 85(1):016105, 2014.

[82] Lin He, Zhen-Hua Han, Feng Jiang, and Jun Sun. Crystallization kinetic characteristics of oxygen-induced i-phase and zr_2cu phase in $zr_{65}cu_{27.5}al_{7.5}$ glassy alloy. *Transactions of Nonferrous Metals Society of China*, 18(3):610–616, 2008.

[83] Hideo Toraya, Masahiro Yoshimura, and Shigeyuki Somiya. Calibration curve for quantitative analysis of the monoclinic-tetragonal zro2 system by x-ray diffraction. *Journal of the American ceramic society*, 67(6):C–119, 1984.

[84] Aspen Aerogels. Pyrogel xtf: Flexible industrial insulation for high-temperature applications. *Datasheet*, 2010.

[85] Ping Wen, ZuoFeng Zhao, and WeiHua Wang. Physical aging in zr46. 75ti8. 25cu7. 5ni10be27. 5 typical bulk metallic glass manifested as enthalpy relaxation. *Science in China Series G: Physics, Mechanics and Astronomy*, 51(4):356–364, 2008.

[86] Yoshinori Katayama, Takeshi Mizutani, Wataru Utsumi, Osamu Shimomura, Masaaki Yamakata, and Ken-ichi Funakoshi. A first-order liquid–liquid phase transition in phosphorus. *Nature*, 403(6766):170–173, 2000.

[87] Srikanth Sastry and C Austen Angell. Liquid–liquid phase transition in supercooled silicon. *Nature Materials*, 2(11):739–743, 2003.

[88] Hai-Bin Yu, Yuansu Luo, and Konrad Samwer. Ultrastable metallic glass. *Advanced Materials*, 25(41):5904–5908, 2013.

[89] Stephen F Swallen, Kenneth L Kearns, Marie K Mapes, Yong Seol Kim, Robert J McMahon, Mark D Ediger, Tian Wu, Lian Yu, and Sushil Satija. Organic glasses with exceptional thermodynamic and kinetic stability. *Science*, 315(5810):353–356, 2007.

[90] Yunlong Guo, Anatoli Morozov, Dirk Schneider, Jae Woo Chung, Chuan Zhang, Maike Waldmann, Nan Yao, George Fytas, Craig B Arnold, and Rodney D Priestley. Ultrastable nanostructured polymer glasses. *Nature materials*, 11(4):337–343, 2012.

[91] Sadanand Singh, MD Ediger, and Juan J de Pablo. Ultrastable glasses from in silico vapour deposition. *Nature materials*, 12(2):139–144, 2013.

[92] Diana Toma, Monika Meuris, U Köster, et al. Oxidation of zr-based metallic glasses in air. *Journal of Non-crystalline solids*, 250:719–723, 1999.

[93] Li-Min Wang and Ranko Richert. Dynamics of glass-forming liquids. ix. structural versus dielectric relaxation in monohydroxy alcohols. *The Journal of chemical physics*, 121(22):11170–11176, 2004.

[94] Peter Rösner. Mechanische relaxation in komplexen fluiden. *Doktorarbeit Göttingen*, 2004.